UTS UNIVERSITY OF TECHNOLOGY SYDNEY

CHARACTERISATION AND MODELLING FOR ELASTOMERIC AND GEL-LIKE MAGNETORHEOLOGICAL MATERIALS

by Shaoqi Li

Thesis submitted in fulfilment of the requirements for the degree of

Doctor of Philosophy

under the supervision of Yancheng Li

University of Technology Sydney
Faculty of Engineering and IT

February 2021

CERTIFICATE OF ORIGINAL AUTHORSHIP

I, Shaoqi Li declare that this thesis, is submitted in fulfilment of the requirements for the award of Doctor of Philosophy, in the School of Civil and Environmental Engineering at the University of Technology Sydney.

This thesis is wholly my own work unless otherwise referenced or acknowledged. In addition, I certify that all information sources and literature used are indicated in the thesis.

This document has not been submitted for qualifications at any other academic institution.

This research is supported by the Australian Government Research Training Program.

Production Note:
Signature: Signature removed prior to publication.

Date: 17 February 2021

CHARACTERISATION AND MODELLING FOR

ELASTOMERIC AND GEL-LIKE

MAGNETORHEOLOGICAL MATERIALS

by

Shaoqi Li

Submitted to the School of Civil and Environmental Engineering

on 22 February 2021, in partial fulfilment of the

requirements for the degree of

Doctor of Philosophy

Abstract

Magnetorheological (MR) material is an aspiring branch of smart material. It can change its mechanical properties rapidly and reversibly subjected to an externally applied magnetic field, so-called MR effect. Due to the sensitivity to magnetic field and the versatility in physical states, i.e., liquid (MR fluid), gel-like (MR gel), elastomeric (MR elastomer), MR materials have tremendous application potential in engineering industries, especially in civil engineering, involving vibration reduction and isolation for infrastructures. However, some MR materials have inherent limitations: sedimentation and instability of MR fluid, and low MR effect and large energy consumption of MR elastomer. MR gels were fabricated to gain the merits of both MR fluid and MR elastomer, i.e., high MR effect and excellent sedimentation resistance.

This work focuses on the two types of MR materials: MR elastomer and MR gel. They both significantly improve the sedimentation problem of MR fluid, yet the current knowledge and design techniques are inadequate to deliver efficient and effective

applications. For MR elastomer, this work implements the hybrid magnets (permanent magnet and electromagnet) configuration in both characterisation and engineering applications to resolve the large energy consumption issue. Moreover, an improved magnetic circuit model is proposed to serve as an effective and efficient approach for designing and analysing MR elastomer devices with complicated structures, i.e., hybrid magnets and laminated structure. In a pioneering manner, the field-dependent dynamic stress-strain hysteresis of MR gel is characterised and shows a unique stress overshoot phenomenon. A simple hysteresis model with support vector machine generalisation technique is formulated and validated the experimental results. Finally, thixotropy of MR gel is characterised by a proposed test protocol considering the variables of shear rate, magnetic field, shearing time and resting time. A thixotropy model for MR gel is proposed and agrees well with the experimental date under all test conditions considered.

Thesis Supervisor: Yancheng Li

Title: Senior Lecturer, School of Civil and Environmental

Engineering, University of Technology Sydney

Acknowledgement

This doctoral thesis is the result of three and a half years of dedicated work with my supervisor, Yancheng Li, to whom I am incredibly grateful for his unwavering patience and guidance. I sincerely appreciate my co-supervisor, Jianchun Li, for his advices and contributions that greatly improved this work. I particularly thank Hong Guan and Xiaobo Qu who encouraged me to embark on this PhD journey. I also would like to acknowledge Yang Yu, Peter Watterson, Peter Brown, and Scott Graham who generously offered their expertise and support. Lastly, my family, thank you for always being there.

List of Publications during the candidature

1. **Li, S.**, Watterson, P., Li, Y., Wen, Q., & Li, J. (2020). Improved magnetic circuit analysis of a laminated magnetorheological elastomer devices featuring both permanent magnets and electromagnets. *Smart Materials and Structures, 29*(8), 085054.
2. **Li, S.**, Liang, Y., Li, Y., Li, J., & Zhou, Y. (2020). Investigation of dynamic properties of isotropic and anisotropic magnetorheological elastomers with a hybrid magnet shear test rig. *Smart Materials and Structures*, *29*(11), 114001.
3. **Li, S.**, Tian, T., Wang, H., Li, Y., Li, J., Zhou, Y., & Wu, J. (2020). Development of a four-parameter phenomenological model for the nonlinear viscoelastic behaviour of magnetorheological gels. *Materials & Design*, *194*, 108935.
4. Yu, Y., Li, J., Li, Y., **Li, S.**, Li, H., & Wang, W. (2019). Comparative investigation of phenomenological modeling for hysteresis responses of magnetorheological elastomer devices. *International journal of molecular sciences*, *20*(13), 3216.
5. Wang, H., Chang, T., Li, Y., **Li, S.**, Zhang, G., Wang, J., & Li, J. (2020). Characterization of nonlinear viscoelasticity of magnetorheological grease under large oscillatory shear by using Fourier transform-Chebyshev analysis. *Journal of Intelligent Material Systems and Structures*, 1045389X20959466.
6. Yu, Y., Royel, S., Li, Y., Li, J., Yousefi, A. M., Gu, X., **Li, S.**, & Li, H. (2020). Dynamic modelling and control of shear-mode rotational MR damper for mitigating hazard vibration of building structures. *Smart Materials and Structures*, *29*(11), 114006.

Contents

Chapter 1

Introduction

1.1 Background

Magnetorheological (MR) material is a branch of smart materials and normally comprises of micro sized ferro-magnetic particles and carrying matrix. By using different types of carrying matrix, various MR materials were developed, i.e., MR fluid [1, 2], MR elastomer [3, 4], and MR gel [5, 6]. When a magnetic field is applied on MR materials, their rheological or mechanical properties can be rapidly and reversibly changed, due to the occurrence of magnetic attraction between the polarized ferroparticles, so called MR effect. In the past three decades, this effect has been adopted to controllable devices such as MR dampers [7, 8], clutches [9, 10], and base isolators [11, 12]. The tuneable mechanical performances of such devices have made adaptive vibration control, torque transmission and earthquake protection possible and tremendously benefited the fields of civil and mechanical engineering.

The first explored is the MR fluid reported by Rabinow in 1948 [13]. It has ferroparticles dispersed in carrying oil. In MR fluids, the di-pole interactions induced by externally applied magnetic field forms arrange the free-flowing ferroparticles into chain and

columnar structures that parallel to magnetic flux. As the field strength increases, the yield strength of the ferroparticle structures and the damping property of the MR fluid become higher. After the field is removed, the particles return to the free-flowing state.

Although MR fluids are the most widely adopted, its development and application have reached a bottleneck due to its significant drawbacks: aggregation and sedimentation, led by the low viscosity of the oil matrix [14]. On one hand, if the magnetic field is applied for a long time, the particles form large aggregates that cannot return to the uniformly dispersed state in the matrix. On the other hand, the long-time magnetic field-off state can result sedimentation which causes the reduce of yield stress and fail to start the MR fluid devices.

To resolve the limitations of MR fluids and implement MR effect in a wider range of engineering applications, MR elastomers and MR gels were developed. MR elastomers use elastomeric materials as matrix, in which the ferroparticles are trapped [15]. In this way, MR elastomers do not have the particle sedimentation problem. Depending on the particle distribution in cured matrix, MR elastomers can be classified as isotropic and anisotropic MR elastomers [16]. In isotropic and anisotropic MR elastomers, the ferroparticles are uniformly dispersed and pre-aligned in chain patterns, respectively. The chain structures in anisotropic samples are formed by applying magnetic field to the sample during the curing of the matrix. The externally applied magnetic field polarizes ferroparticles; and the intensifying of field strength leads to stronger interparticle attractions and higher stiffness and damping properties of the MR elastomer. The elastomeric matrix also exhibits the bearing capacity against vertical loadings that made applications such as MR elastomer isolators [17] and vibration absorber [18] possible.

However, the limited mobility of ferroparticles results in a lower MR effect of MR elastomer compared with MR fluids. In terms of energy efficiency, majority of reported MR elastomer devices requires relatively higher power than MR fluid devices [15]. This is

due to that the elastomers have limited tensile strength. To reach a designated shear deformation, thick or multiple layers of MR elastomers were introduced to the devices [11, 18]. This results in the long magnetic flux path that may require up to hundreds of watts to fully energise the device [19]. Thus, the electromagnetic performance of a MR elastomer device should be specifically designed and analysed through magnetic circuit or finite element methods to deliver an effective and efficient adaptive performance. Compared with finite element, magnetic circuit models provide equational representation to intuitively describe the relations between magnetic field density and device specifications [20-22]. This method is well adopted for optimizing the performance of MR fluid devices, yet it has not reported in MR devices with complicated structures.

To develop a system that has outstanding sedimentation performance, high MR effect and high yield stiffness, MR gel were developed [23]. It can be treated as the intermediate between MR fluid and MR elastomer. MR gels are generally comprised of ferroparticles and crosslinked polymeric gels and additives. They appear as viscous gels [24-26] or solid-like [27, 28] depending on the fabrication process and composition. Differing from MR fluid and MR elastomer, the off-state viscosity of MR gel can be easily tailored by controlling the polymeric crosslink profile and component of the carrier matrix which gives abundant flexibility of preparing MR gels [29]. Most importantly, the high viscosity and crosslinked structures of the polymer structure greatly reduce the chance of sedimentation of MR gel during resting. However, the highly crosslinked gel matrix with high concentration of particle filler could raise thixotropy which is a time-dependent recoverable rheological effect [30]. The typical behaviour of a thixotropic material is the gradually decreasing viscosity under flow [31]. After the material has been sheared and then rested, the viscosity can recover for a certain level. This effect may affect and cause unstable force output during starting-up or changing shear rates of the devices. To date,

the investigations on the characterization, modelling and application on MR gels are of a limited amount, and the thixotropy of MR gel is not reported.

Despite that MR effect could play a crucial role in engineering industries, towards the effective and efficient design and application, it is fundamental to carry out characterisation and modelling for this complicated behaviour and improve the current design and analysis techniques. This project attempts to mitigate the current knowledge gap between material and practical application in the field of MR materials by focusing on both elastomeric and gel-like MR materials. This is done by conducting: energy-efficiency design for MR elastomer characterisation and engineering applications, improved magnetic circuit modelling for complicated MR elastomer device, characterisation and modelling of dynamic behaviour of MR gel and, experimental and numerical investigations of thixotropy for MR gel.

1.2 Objectives

The overall aim of this research is focused on the investigations of two types of MR materials: MR elastomer and MR gel, in terms of the characterisation and modelling of the mechanical and rheological properties. From the engineering application perspective, MR device design techniques and time-dependent rheological properties of MR materials are also investigated. The specific objectives are listed as follows:

1. Propose an energy-efficient hybrid magnets test rig to characterise the dynamic properties isotropic and anisotropic MR elastomer with considering the influences of different ferroparticle weight fractions, excitation amplitude and frequency, and magnetic fields. Phenomenological modelling of the characterised stress-strain hysteresis of isotropic and anisotropic MR elastomer samples.

2. Propose an easy and accurate magnetic circuit model to facilitate the design and electromagnetic analysis of a prototype laminated MR elastomer base isolator featuring both electromagnet and permanent magnet.
3. Characterise the dynamic stress-strain hysteresis behaviour of MR gel with considering the influences of strain amplitude, excitation frequency and magnetic field. Propose a phenomenological model for MR gel.
4. Propose a characterisation method for the time dependent behaviours of MR gels with considering the resting time, shearing time, shear rate, and magnetic field. Formulate a time-dependent model to predict the characterised time dependent properties of MR gel.

It should be mentioned that the COVID-19 pandemic has significantly affected the scope and progress of this research – being the non-operation of the essential shake table facility and unavailability of technical repairing support since February 2020 to date. The characterisation of the proposed base isolator is thus unable to be carried out and planned in the future work. To deliver integral and comprehensive research outcomes, this research has switched the focus to the investigation of MR materials which include the characterization and modelling of the dynamic properties and thixotropy of MR gel.

1.3 Outline

Starting with an introduction, this thesis firstly presents the background and motivation, objective, and outline of this work.

Chapter 2 provides a literature review on the current development of MR materials, including their properties and drawbacks, characterisation and modelling methods, and engineering applications.

In Chapter 3, a hybrid magnets shear test rig is proposed to experimentally explore the influences of anisotropy and weight fraction of ferroparticle on the field-dependent dynamic mechanism of MR elastomer. A stiffness stiffening model is implemented to predict the characterised behaviours of different MR elastomer samples.

In Chapter 4, an energy-efficient hybrid magnets MR elastomer base isolator is designed and fabricated as an analysis prototype. An improved magnetic circuit analysis is proposed to provide an effective and efficient approach to design and analyse MR elastomer devices with complicated structures, i.e., hybrid magnets and laminated structure.

In Chapter 5, MR gel is characterised under large amplitude oscillatory shear and exhibits a unique field-dependent stress overshoot phenomenon. A simple hysteresis model with support vector machine generalisation technique is constructed for MR gels and generalised by support vector machine.

In Chapter 6, thixotropy of MR gel is characterised by a proposed testing protocol with considering the variance of shear rate, magnetic field, shearing time and resting time. A thixotropy model for MR gel is proposed and shows good agreement with the experimental result under all test conditions considered.

Chapter 7 conclude the findings of this research and discuss the future research work.

Chapter 2

Literature Review

2.1 Preface

Materials whose properties can be reversibly controlled upon the application of an external stimulus (like mechanical, thermal, magnetic, electrical, etc,) are identified as smart materials. To date, various branches of smart materials were developed, i.e., MR materials [4, 6], electrorheological fluids [32, 33], and shape memory alloys [34, 35]. Since a homogeneous material hardly retains multifunction, smart materials normally composite materials with the abilities of perception, actuation, and control to realise the multi-characteristics. MR materials are fabricated by dispersing ferromagnetic particles which can rapidly and reversibly response to magnetic field in carrier matrix which can be various types of viscoelastic materials. Thus, MR materials possess the adjustable viscoelastic properties in response to externally applied magnetic fields. According to the matrix and the physical state when no magnetic field applied, MR materials can be categorised into MR fluids [36, 37], MR elastomers [3, 4], MR gels [5, 6], etc.

However, despite being widely adopted in the construction, automotive and robotics industry, the implementation of MR material is still faced with challenges. Each type of

MR materials has their own unique rheological properties and limitations. The sensitivity to magnetic field added another layer of complication in the behaviours of the MR materials. More discussions on the challenges identified in the current research and application of MR materials will be detailed in the following sections.

In this chapter, a comprehensive review on the MR materials will be firstly presented, with the emphasis laid on the origin, compositions, properties, applications, and drawbacks. Next, the characterisation and modelling techniques for MR materials are elaborated and compared. Finally, the gaps and challenges of the current development and application of MR materials are identified and concluded.

2.2 MR materials

2.2.1 MR fluid

MR effect in MR fluids was firstly reported by Jacob Rabinow in 1948 [13], inspired by electrorheological effect [38]; but the serious instability of MR fluid has curbed the commercial success in the years following. In 1990's, MR effect stated to gain intensive attentions as it exhibits much stronger interparticle attractions than electrorheological effect. This advantage has made MR fluid a more preferrable option in developing controllable devices in the past three decades.

A typical MR fluid is composed of ferromagnetic particle filler, carrier fluid, and additives; and can be easily fabricated by mixing all components together until the uniform distribution of the filler is reached. The most common carriers are silicone oil and petroleum oil. For the ferroparticle filler, carbonyl iron particle (CIP) is the widely adopted due to its large saturation magnetization which can reach up to 2.1 T. The ferroparticle normally takes approx. 20% to 40% of the total volume of the fabricated MR fluids. To

prevent the particles from sedimentation and aggregation, additives like stabilizer and surfactant are necessary added.

In response to the external magnetic field, the randomly dispersed ferroparticles are aligned into chain-like microstructures instantaneously. Stronger field intensity contributes to longer and more ordered microstructures. The photos of chain-like microstructure are presented in Fig. 2.1 [39]. The rheological manifestation of this field-induced microstructure evolution is the increasing yield stress of MR fluid under shear flow. From the past rheological measurements, MR fluid expresses as a classic Bingham fluid with the maximum yield stress exceeding 100kPa and the up tune of apparent viscosity reaching four orders of magnitude, when magnetic field applied [25].

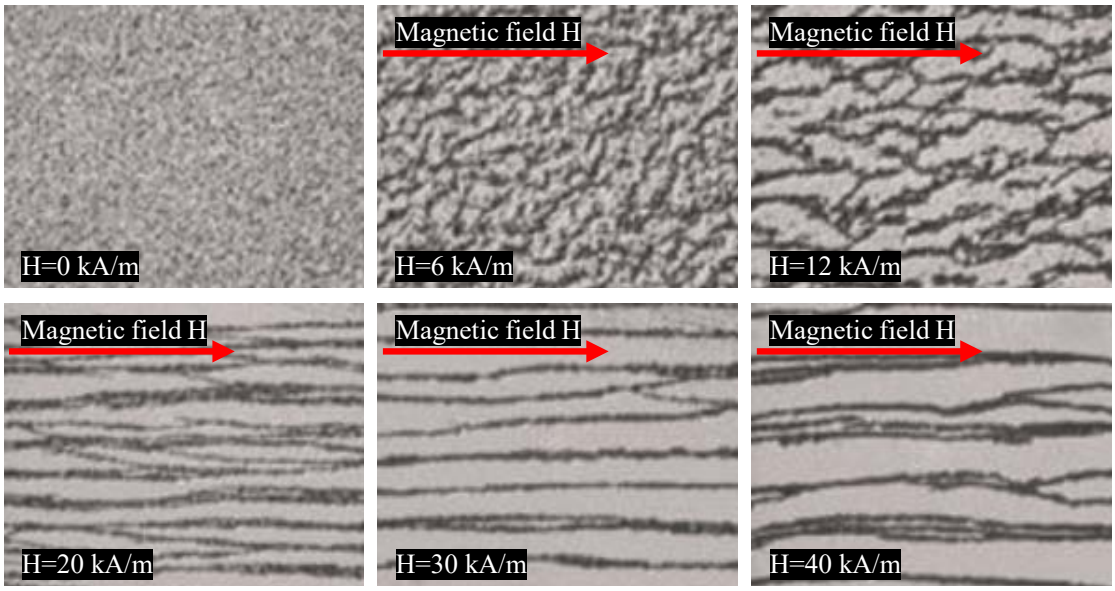

Fig. 2.1 Photo of chain structures under different magnetic fields [39]

The applications of MR fluids can be classified into three basic operating mode: flow mode, shear mode and squeeze mode. The diagrams of the three modes and schematics of their typical application are presented in Fig. 2.2 and Fig. 2.3, respectively. In flow mode, MR fluid is sandwiched and made to flow between two fixed plates. The magnetic field is applied perpendicular to the direction of the flow and controls the flow resistance of MR

fluid. Typical applications operation in this mode are damper, shock absorber and actuators. In shear mode, MR fluid is subject to the shear motion induced by the relative displacement to the two plates. The viscosity of MR fluid is adjusted by the magnetic field to exhibit controllable shear stress response under different shear rate of the top plate. Examples of application working in this mode are breaks, dampers and clutches. In squeeze mode, the changing displacement between the two plates causes the flow motion of MR fluid. Device operating in this mode are normally limited to a small displacement amplitude, usually several millimetres.

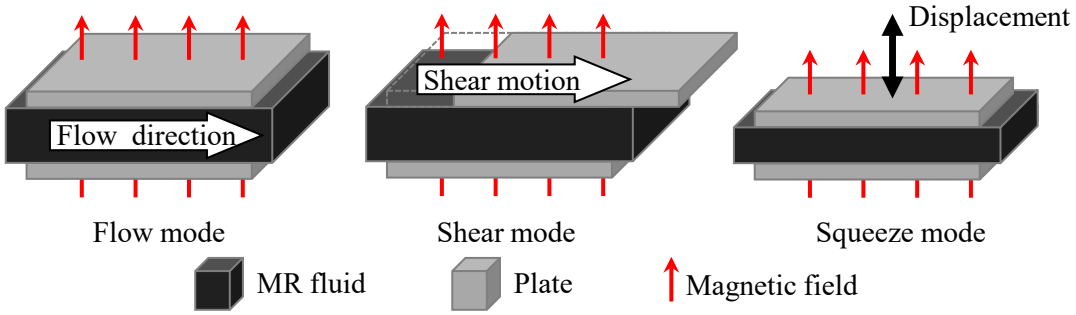

Fig. 2.2 Operating modes of MR fluid

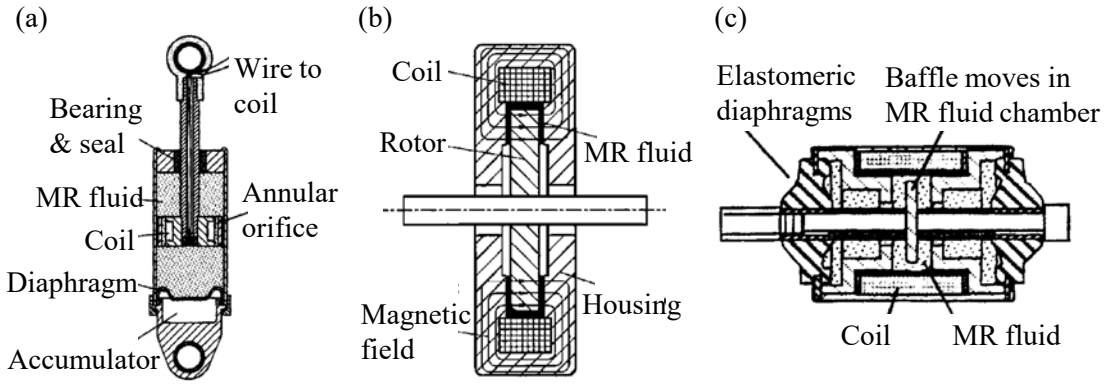

Fig. 2.3 Schematics of MR fluid applications (a) A flow mode MR fluid damper [40] (b) A shear mode MR fluid clutch [36] (c) A squeeze mode MR fluid vibration damper [40]

The mismatch between the densities of the ferroparticles and the carrying matrix leads to serious sedimentation problem which impends a wider application of MR fluids.

Addressing this drawback, several techniques were proposed with the focuses on augmenting the ferroparticle and introducing additives to the carrier fluid. The detailed measures to avoid sedimentation and aggregation in MR fluid are listed as follows:

1. Appling coting, i.e., amorphous silica [41], organic polymer [42], and polymethyl methacrylate [43], on the ferroparticles to reduce its density difference from the carrier.
2. Using spherical nanosized particles as solid additive which usually have lower densities and larger surface area to volume ratio than the micron-sized ferroparticles [44, 45]. Due to the seraphical area-volume ration increases when the radius decreases to the nanometre level [46].
3. Adding wire particles in together with nanoparticles to improve the consistency and broad size distribution of the particle phase and to enhance the yield stress of the chain-like microstructure[47-49].
4. Adding stabilizers and additives to the matrix to improve the structural stability and prevent sedimentation. Common additives are fumed silica [50], polyacrylic acid [51], submicron-sized organoclays [52], etc.
5. Using polymeric gels and lubricant as carrying matrix. This method actually evolves the MR fluid to a new branch of MR material: MR gel [5, 6].

However, using additives, coating, and nanoparticles brings some undesired effects to the MR fluids: reduced yield stress and poor particle shape consistency. Practices of using several additives altogether were carried out and proved to be effective. But this method introduced difficulty and reduced the flexibility of fabricating MR fluids. Nowadays, studies in the field have showed increasing interests in using polymeric gels as matrix to fabricate MR gel, as this method improves both the stability of particle dispersion and the yield stress while maintaining an easy and flexible fabrication process. A review on MR gels is prepared in Section 2.2.3.

2.2.2 MR elastomers

The sedimentation problem of MR fluids is can be improved by modifying the carrier and ferroparticle but only to limited extent. To completely resolve this issue, MR elastomer were firstly proposed by Shiga *et al.* in 1993 [53]. MR elastomers appear as solid state with and without the external magnetic field and are generally comprised of three components: ferroparticles, elastomer or rubber matrix and additives [15]. The fabrication of MR elastomers involves three essential steps: mixing, removing air bubble, and curing. Depending on the presence and absence of magnetic field during curing, the dispersion of ferroparticles can classified into two types: isotropic and anisotropic [16]. If no magnetic field was applied during curing, the particles are uniformly distributed and locked in the cured matrix. This type of MR elastomer is called isotropic MR elastomer. The other type is anisotropic MR elastomer. It has aligned particle-chain structures locked in the elastomeric matrix by the external magnetic field applied during curing. Fig. 2.4 presents the scanning electron microscope (SEM) of both isotropic and anisotropic MR elastomers [54].

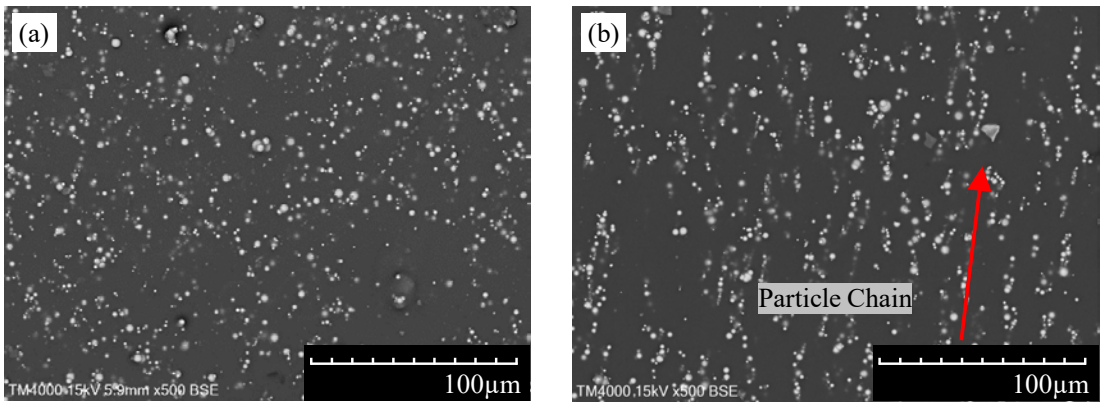

Fig. 2.4 SEM of MR elastomers (a) Isotropic sample [54] (b) Anisotropic sample [54]

MR elastomers generally operate within its pre-yield region and possess adjustable viscoelasticity [55]. Under magnetic fields, the ferroparticles are polarised and interparticle

attractions are generated. This effect increases both the stiffness and damping of a MR elastomer. The adjustability of a MR elastomer is normally judged by its storage modulus as the magnetic field induced damping parameter change are rather small [4, 56, 57]. The ration between the difference of the storage modulus of a MR elastomer under magnetic field and zero-field and the zero-field storage modulus is defined as MR effect of MR elastomer. Literatures showed that anisotropic MR elastomers have higher MR effect compared with the isotropic sample [16, 54].

The operation modes of MR elastomer devices differ from the MR fluid devices due to the solid physical state and the limited particle movement. Fig. 2.5 shows the basic modes of MR elastomers [58]. In shear mode and compression mode, the motion of the top plate deforms the MR elastomer. By adjusting the magnetic field, the resulted shear or compression force can be actively tunned. Examples of devices using shear mode are absorber and vibration isolator. Devices operating in compression mode are compression spring, MR elastomer mount and vibration absorber. The filed-active uses the magnetostrictive effect can be explained as the field-induced interparticle attraction brings the ferroparticles closer and deforms the carrier matrix. This effect was used for developing actuators. Typical of engineering application are presented in Fig. 2.6.

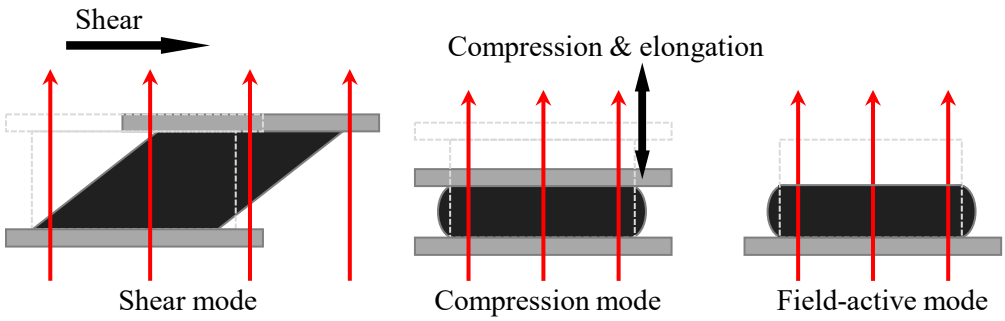

Fig. 2.5 Basic operating modes of MR elastomer (red arrows indicate the direction of magnetic field)

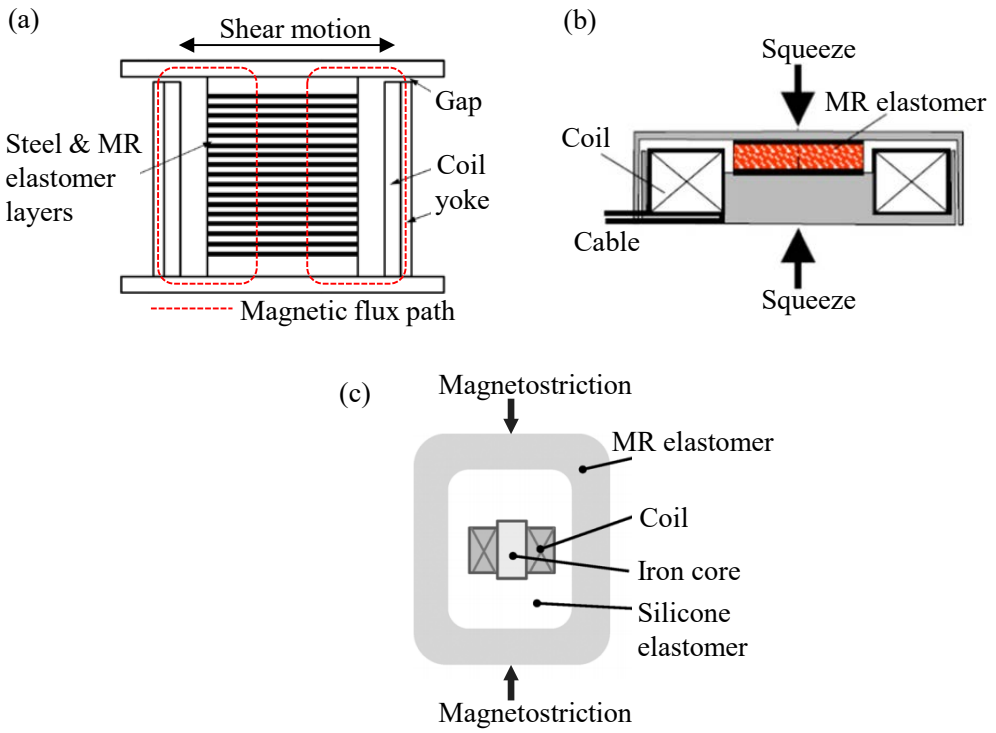

Fig. 2.6 Applications of MR elastomer: (a) A shear mode base isolator [59] (b) A compression mode MR elastomer spring element [60] (c) A MR elastomer soft actuator [61]

Although elastomeric matrix completely prevents the filling particle from settling in MR elastomer, the MR effect is contrarily reduced which makes the requirements of engineering application hard to be achieved. Moreover, MR elastomers are required to operate in its pre-yield regime to avoid irreversible damage to the material. In engineering applications, the effective thickness of the MR elastomer layers can reach up to 40 millimetres [11, 59]. To fully activate MR effect, magnetic flux needs to penetrate and saturate all the MR elastomer layers. The magnetic flux path in a MR elastomer device becomes longer and more complicated than that of a MR fluid device which normally have several millimetres fluid channel [21, 22, 62-64]. This leads the increasing design complexity of MR elastomer devices. Accurate magnetic circuit model and finite element model are mandatory to be constructed to ensure that adequate field strength can be

applied on the MR materials. However, as one of the most effective and accurate method for optimizing electromagnetic design, magnetic circuit models [21, 22] were rarely reported for MR elastomer devices in the past.

2.2.3 MR gel

MR gel is another class of magnetoactive smart material which uses viscoelastic polymeric matrix. The concept was firstly proposed by Shiga *et al.* in 1995 [23]. MR gels can be regarded as the intermediate between the MR elastomer and MR fluid. The fabrication of MR gels is kept in a process of mixing and resting. Depending to the physical state at zero-field, MR gels can be further distinguished into liquid-like [24-26] and solid-like MR gels [27, 28]. Liquid-like MR gels can be treated like a MR fluid with using polymeric gel solution as matrix. The network or crosslinked structure of the polymeric gel augmented the interfacial characteristics and interaction with the ferroparticle. These aspects helped to reduce the sedimentation and enhanced the strength of particle chain structures under magnetic fields [25, 65, 66]. For solid-like MR gels, the most fascinating feature is that the sedimentation problem is completely resolved as MR elastomer [67, 68]. But the physical state does not show the elasticity as rubber and elastomer, solid-like MR gels cannot be classified into MR elastomer.

In the past decade, both liquid-like and solid-like MR gels have experienced a reveal of interest due to their high MR effect and outstanding sedimentation resistance. Images of liquid-like and solid-like MR gels are presented in Fig. 2.7. Xu *et al.* investigated the rheological and sedimentation performance of liquid-like MR gels samples with different weight fractions of CIP [29]. The results indicated that when the CIP content is less than 25% of the total weight of the sample, the particle sedimentation can be effective avoided. An *et al.* investigated the field-dependent rheological behaviour of MR gel and suggested that the storage modulus of MR gel under 650 mT was increased for over 6000% compared

with the zero-field scenario [69]. Xu *et al.* fabricated a novel solid-like MR gel by mixing micron sized magnetic particles with plasticine-like polyurethane as shown in Fig. 2.7(b), (c), and (d) [68]. When no filed applied, this material can be easily shaped and preserve the shape like plasticine. When the magnetic field is applied, the solid-like MR gel deforms along the direction of the magnetic field. Moreover, the aligned particle microstructure can be maintained after the field is removed.

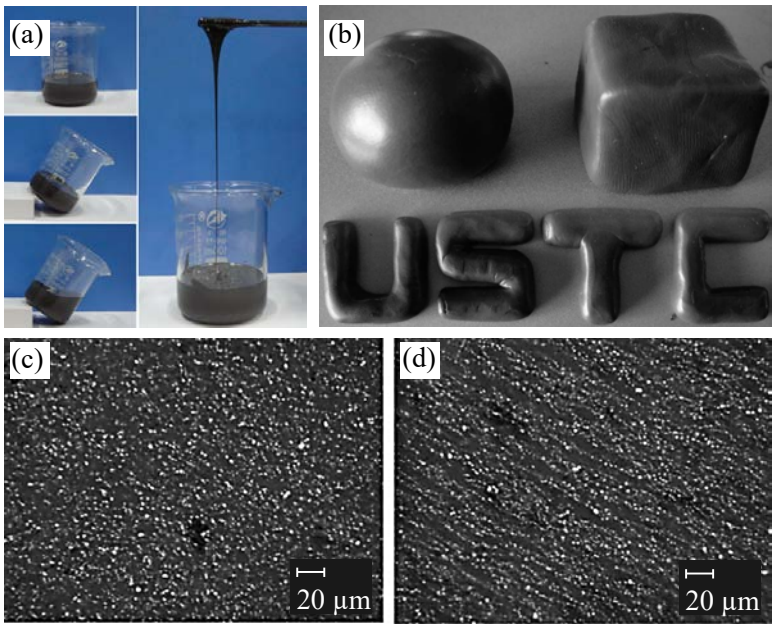

Fig. 2.7 Images of MR gels (a) liquid-like MR gel [70] (b) solid-like MR gel [68] (c) SEM of MR gel without magnetic field [68] (d) SEM of MR gel under magnetic field [68]

As conclusion, MR gels holds the merits of both MR fluid and MR elastomer which are movability of particle, improved sedimentation performance and the ability to retain the particle chain structures. The flexibility of the physical state, controllable zero-field property, and simple fabrication process provides possibility to enlarge the range of engineering application. However, due to the MR gel matrix provide weak restrains on the particles, the response of MR gel differs from that of MR elastomer and MR fluid. The mechanical behaviour of MR gel can show distinct differences for the zero-field and field applied scenarios. Moreover, compositions of the highly crosslinked polymeric structure

and particles normally express time dependent rheological behaviours: thixotropy [31]. Coupled with magnetic field, this uncharacterised behaviour of MR gel can escalate to another level of complexity.

At the current state, investigations of MR gels are limited in reporting the sedimentation performance and characterisation of basic rheologic parameters, i.e., modulus and viscosity, engineering applications are rarely reported. Thus, the current understanding of this material is far from enough to develop valid and effective engineering applications and significant effort should be laid on the characterisation and modelling of the dynamic hysteresis (stress-stain relationship) and time-dependent rheological behaviours before developing MR gel engineering applications.

2.3 Experimental characterisation of MR materials

Experimental characterisation of MR materials serves as a crucial role towards the understanding of the magneto-mechanical coupled effect and certifying the veracity of theoretical results, by providing the necessary rheological parameters. There are number of testing protocols like shear tests, compression and tension tests, fatigue test, etc., were reported for the magneto-mechanical properties for MR materials. The most widely adopted is using shear loadings as this mode is adopted for most of the engineering applications of MR material [71]. For MR elastomers, uniaxial and biaxial compression/tension tests were also reported [72-74]. Except from the essential factors like magnetic field and loading, the influence of temperature, shape, particle concentration, particle arrangement (isotropy and anisotropy) and PH value were also broadly studied. Common characterisation equipment are rheometer, dynamic mechanical analyser (DMA), and customized test rig. These equipment are normally equipped with electromagnetic modulus or permanent magnets to apply the external field on the test samples.

2.3.1 Steady shear test

Steady shear tests characterise the basic rheological parameters, i.e., shear stress and viscosity, for both solid-like and liquid-like MR materials. This characterisation is normally performed on rheometers (Fig. 2.8(a)) with a parallel plate setup which is shown in Fig. 2.8 (b). The setup forms a gap between the plate shaped measuring tool and the base plate. The MR material is accommodated in the gap. The rheometer motor applies shear motion in one direction to the sample through the measuring tool and measures the resulted torque. The measured torque can then be interpreted to the shear stress and viscosity data based on the measuring tool geometry and shear rate. Besides this geometry, twin-gap setup (Fig. 2.8(c)) was also reported for characterising MR materials [75, 76]. It provides a shielded container for the sample and prevents the sample from spilling out during high shear rates which can reach up to 10000 1/s. However, this configuration can only be used for testing liquid-like MR materials. Both plate-plate and twin gap geometries have the coil positioned beneath the bottom plate to apply magnetic field on MR materials.

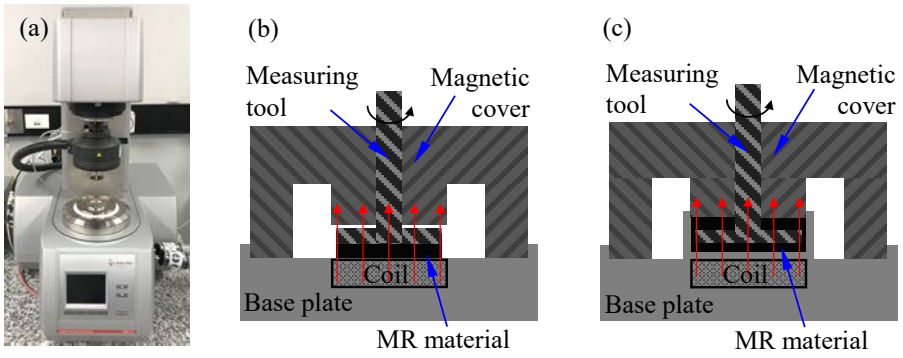

Fig. 2.8 Image of (a) Anton Paar MCR 302 rheometer (b) parallel plate geometry (c) twin gap geometry (red arrows indicate the direction of magnetic field)

The field-dependent rheological behaviours can be portrayed by Bingham model:

$$\begin{aligned} \tau &= \tau_y + \eta\dot{\gamma} \qquad |\tau| \geq \tau_y \\ \tau &= G_0\gamma \qquad |\tau| < \tau_y \end{aligned} \tag{2.1}$$

where τ, τ_y η, $\dot{\gamma}$, and G_0 represent the shear stress, magneto-dependent yield stress, plastic viscosity, shear rate and shear modulus in linear viscoelastic regime, respectively. Fig. 2.9(a) is a typical result steady flow test result for a MR fluid [77]. For MR liquid, the pre-yield regime is usually less than 0.1 strain and the shear stress value at 0 1/s is normally to represent τ_y. Fig. 2.9(a) indicated that the magnetic field considerably increases τ_y and shear rate has less influence on the resulted stress or the plastic viscosity of MR fluid under magnetic field. Thus, the field induced τ_y is normally regarded as a key characterisation parameter to judge the MR effect for liquid-like MR materials. Similar findings were also reported from the steady characterisation of a MR gel as shown in Fig 2.9(b), but with a more apparent increase in the plastic viscosity when shear rate increases [29].

For solid-like MR materials, the focus of this characterisation is laid in the pre-yield regime as majority of applications of solid-like MR materials avoid the occurrence of yielding during operating. Fig 2.9(c) shows the characterisation result a MR elastomer under steady shear tests [55]. The slope of the curve represents G_0. It can be observed that magnetic field contributes to the increase of shear modulus of MR elastomer and the shear stress grows linearly with the increase of shear strain within 10% strain which is the linear viscoelastic region. This finding completely differs with MR fluid and suggest that MR fluid operates within its yielding regime, whereas MR elastomer operates in the pre-yield region. When a strain over 10% is applied on the MR elastomer, the shear modulus no longer increases, and the resulted stress maintains at the same level. This could be resulted by sample sliding and friction.

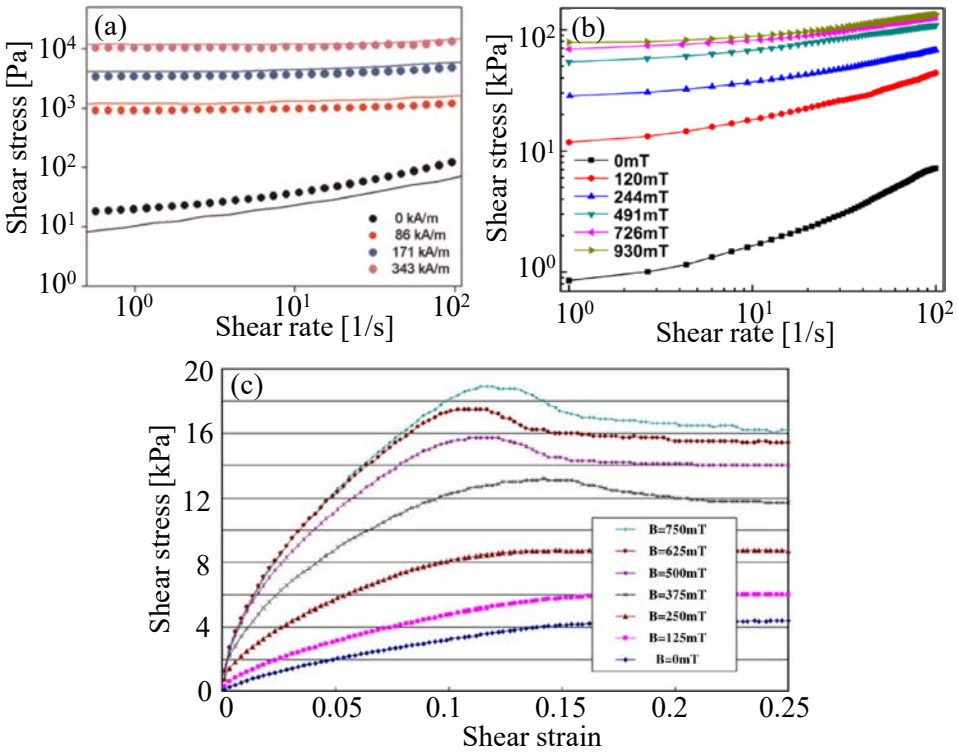

Fig. 2.9 steady shear results of MR materials (a) a MR fluid [77] (b) a MR gel [29] (c) a MR elastomer [55]

Steady shear can serve as a universal characterisation technique for MR materials to evaluate their MR effect with considering the influence of essential variables: strain, strain rate, and magnetic field. It should be noted that for solid-like MR materials the shear rate and stain should be carefully chosen as the friction caused by slippage is sometimes mistaken as yield stress. However, the understandings are limited in the rheological aspect, which is not enough for developing engineering application.

2.3.2 Dynamic shear test

Both solid and liquid MR materials are viscoelastic materials, and the dynamic mechanical properties are the most important aspect to be considered during design an adaptive device. Oscillatory shear test is one of the fundamental techniques [78-80]. It applies sinusoidal

strain to the sample and measures the resulted shear stress. The measured stress is either leading or lagging with the applied strain for a certain phase δ. The shear stress σ thus writes:

$$\sigma = \sigma_0 \sin(\omega t + \delta) = \sigma_0 \sin \omega t \cos \delta + \sigma_0 \sin \delta \cos \omega t \quad (2.2)$$

where t, ω, and σ_0 are time, excitation frequency, and amplitude of shear stress, respectively. The storage modulus G' and loss modulus G'' can be further derived from Eq. 2.2 as:

$$\sigma = \gamma_0 (G' \sin \omega t + G'' \cos \omega t) \quad (2.3)$$

where γ_0 is the strain amplitude. For a viscoelastic material, the storage modulus G' indicates the ability to store energy and loss modulus G'' evaluates the ability to dissipate energy. The ratio between G'' and G' represents the loss factor tan δ. As most of the MR materials applications operates in oscillatory shear mode, thus their magneto-mechanical coupled dynamic properties can be evaluated by G', G'' and tan δ. This characterisation can be carried out by both rheometers, dynamic analyser, and customized test setups with setting essential variables: amplitude, frequency, and magnetic field. Examples of the oscillatory shear test results for MR fluid, MR gel and MR elastomer are presented in Fig. 2.10 and showed typical viscoelastic characteristics: storage modulus dramatically decreases when the strain exceed the linear viscoelastic regime and shear rate increases the storage modulus. The external magnetic field contributes to the significant increase of storage modulus due to the field-induced interparticle attractions enhanced stiffness chain-like particles microstructure in the MR materials.

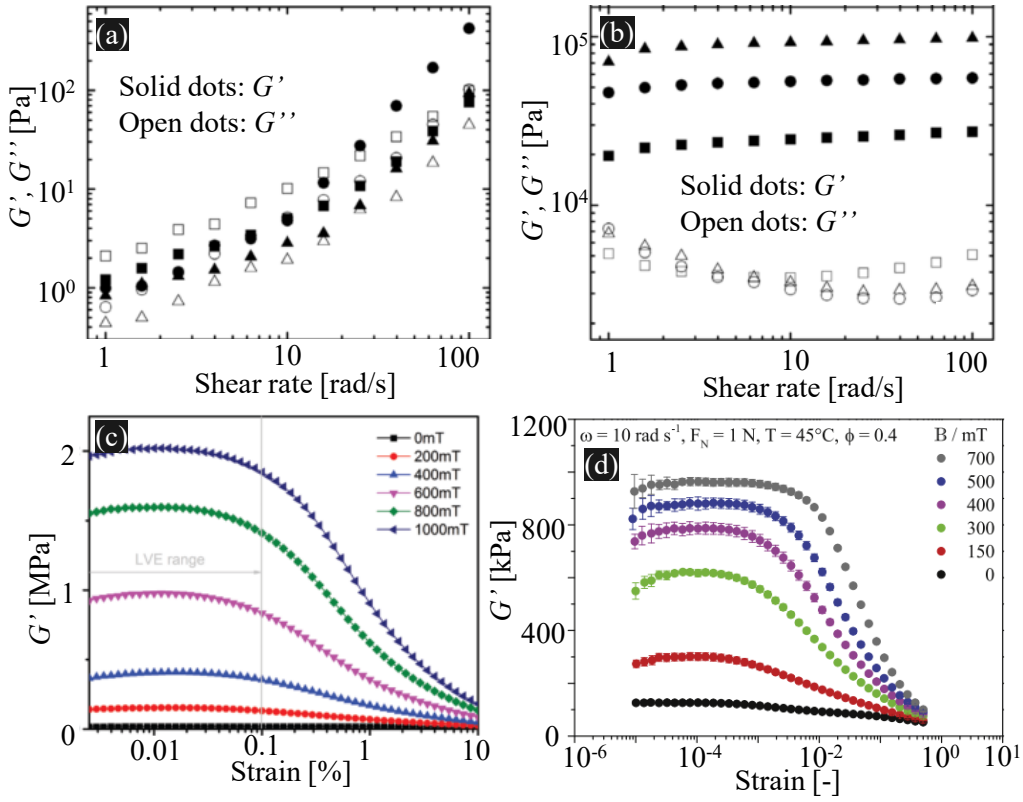

Fig. 2.10 Oscillatory shear characterisation results of (a) MR fluids under zero-field [81] (b) MR fluids under 220 mWbm^{-2} [81] (c) MR gel [82] (d) MR elastomer [78]

Except for the modulus, the oscillatory shear also provides insights of dynamic stress-strain hysteresis relationship which plays an essential role in mathematical modelling and control algorithm. The recorded raw shear stress or shear force data are plotted with the corresponding excitation strain or displacement waveform to form the hysteresis loops. For MR fluids, this method can indicate and compare the damping performance in the pre-yield and post yield region. As shown in Fig. 2.11(a), in post yield region of a MR fluid, the shear force can be maintained at the same level which indicate the maximum damping force can be provided by the developed devices, i.e., dampers [83]. The magnetic field increases the damping force and the enclosed area of the hysteresis loop which stats for the dissipated energy. For solid-like MR materials, the hysteresis is normally characterised within the pre-yield region to investigate its unique field dependent stiffening and softening

effect. Thus, the characterised hysteresis loops can be of a completely different shape from MR fluids. In Fig. 2.11(b), the shear stress versus shear strain of a MR elastomer under different magnetic fields were characterised and plotted by [80]. When no magnetic field applied, the hysteresis presents a perfect ellipse shape. As the magnetic flux density increases, the slop of the curve was increased which indicates the stiffness stiffening effect. Similar to MR fluid, magnetic field also contributes to the damping properties of MR elastomer.

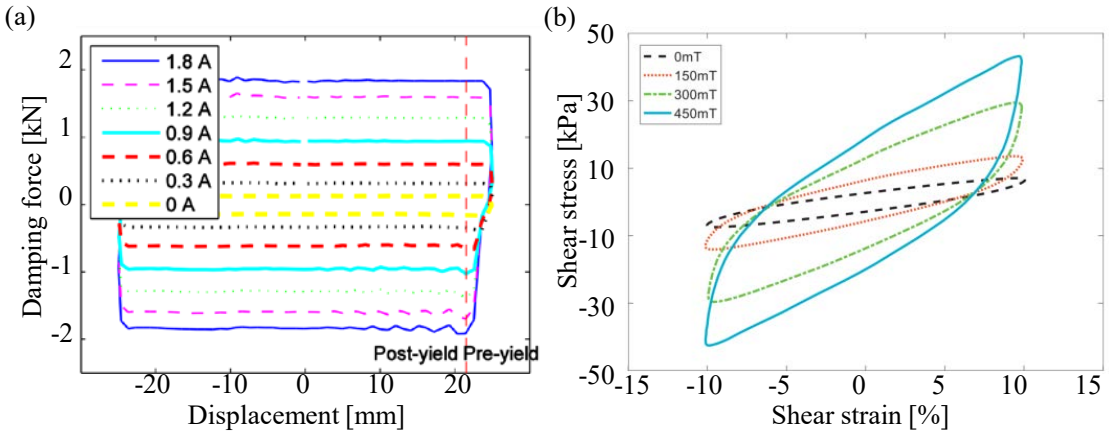

Fig. 2.11 Stress-strain or force-displacement hysteresis loops for (a) MR fluid [83] (b) MR elastomer [80]

However, the characterisation of dynamic stress-stain hysteresis for MR gel was not carried out in the past. Although the zero-field physical state of MR gels can be liquid as MR fluid, the hysteresis characteristics of MR gel could be drastically different and become more resemblant to MR elastomer as its oscillatory shear characterisation under magnetic field show similar performance as MR elastomers. As a promising novel controllable composite and the improvement for both MR fluid and MR elastomer, the characterisation of stress-stain hysteresis for MR gels is of urgent demand and could benefit their potential engineering developments.

2.4 Modelling of MR materials

Considerable amount of ongoing research in the field of MR materials are focused on the modelling of the mechanical properties. As a matter of fact, the modelling the coupled magneto-mechanical behaviour is a fundamental step to the deep understanding of the nonlinear viscoelastic properties and engineering applications. According to the literature, the works can be divided into two parts: physical models and phenomenological models. These two types serve for drastically different purposes.

For physical magneto-mechanism of MR materials, the most adopted theory is particle magnetisation model [84]. It essentially utilizes the difference of magnetic permeability between the matrix and ferroparticle to establish particulate models. By assuming that only adjacent particles can form interparticle attractions, and decreasing the multidirectional magnetisation of a particle as magnetic dipole, the magnetic moment m of a spherical ferroparticle in its linear magnetisation range can be derived as:

$$\begin{aligned} m &= 4\pi\mu_0\mu_m\beta a^3 H_0 \\ \beta &= (\mu_p - \mu_m)/(\mu_p + 2\mu_m) \end{aligned} \tag{2.4}$$

where a, μ_0, μ_m, μ_p, and H_0, are spherical radius, permeability of vacuum, relative permeability of matrix, relative permeability of ferroparticle and field strength, respectively. β is the permeability parameter. Once the ferroparticles are magnetised, with the assumption of neglecting local field corrections, their interaction by magnetostatic force thus writes:

$$\underline{F}_{ij}^{mag} = (\underline{m}\cdot\nabla)\underline{B} = -\frac{3m^2}{4\pi\mu_0\mu_m r_{ij}^4}\left[(3\cos^2\theta_{ij} - 1)\hat{r} + \sin(2\theta_{ij})\hat{\theta}\right] \tag{2.5}$$

where r_{ij} is the centre-to-centre distance between ferroparticles and θ_{ij} is the angle between r_{ij} and the magnetic field vector as shown in Fig. 2.12. By substituting Eq. 2.4 to Eq. 2.5,

and assuming all particles can the same strength m, the bare point dipole force and the interaction energy can be derived as:

$$\underline{F}_{ij}^{mag} = -12\pi\mu_0\mu_m\beta^2 a^2 H_0^2 \underline{f}$$

$$\underline{f} = \left(\frac{a}{r_{ij}}\right)^4\left[(3\cos^2\theta_{ij} - 1)\hat{r} + \sin(2\theta_{ij})\hat{\theta}\right] \tag{2.6}$$

$$V_{ij}^{mag} = \frac{m^2}{4\pi\mu_0\mu_m r_{ij}^3}(1 - 3\cos^2\theta_{ij})$$

Eq. 2.6 can quantitively explain a great deal of rheological behaviour for field-dependent rheology. However, the accuracy of physical model can only be guaranteed for low particle concentration as this technique does not include the presence of mobility and multiple pole interactions [85, 86]. Modelling and understating for highly concentrated MR materials constitutes a challenging task and requires further investigations.

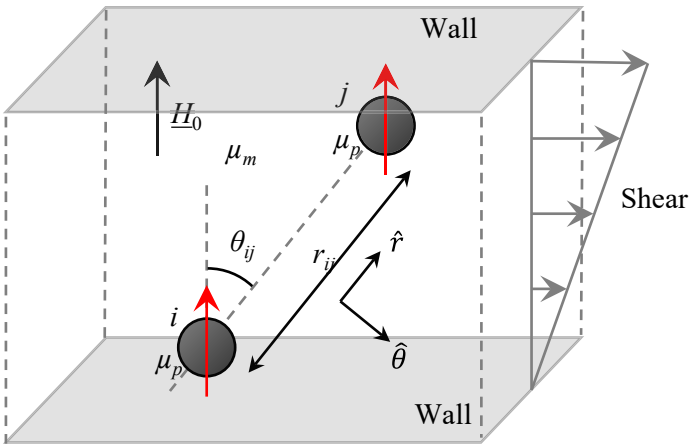

Fig. 2.12 coordinate system for two ferroparticles subject to shear motion in the magnetic field

For newly developed MR materials, especially for MR elastomers and MR gels, the characterised magnetorheological behaviours are modelled by phenomenological models as they directly formulate an expression through the obtained experimental results. Most MR materials express viscoelasticity, thus phenomenological modelling attempts are normally carried out based on a classic Kelvin-Voigt model which parallels a stiffness

spring (k) and a damping element (c), as shown in Fig. 2.13(a) [87]. Based on this model, Li *et al* [55]. augmented this model to portray the field-dependent viscoelasticity for MR elastomers as shown in Fig. 2.13(b) and formulated as:

$$\tau = k_1\gamma_1 + k_b\gamma$$
$$k_1\gamma_1 = k_2(\gamma - \gamma_1) + c(\dot{\gamma} - \dot{\gamma}_1) \quad (2.7)$$

where τ is the estimated stress, γ is the applied strain, $\dot{\gamma}$ is the strain rate. k_b is introduced to represent the field dependency of MR elastomer. The accuracy of the model is validated with oscillatory shear test for MR elastomer within the linear viscoelastic region. In a similar manner, a rheological model that considers the interface slippage between the ferroparticle and matrix of MR elastomer was proposed by Chen *et al.* [88], as shown in Fig. 2.13(c). The proposed model consists of three parts which are a viscoelasticity part, field-induced mechanical property part and an interface slippage part. Besides the combinations of spring, damping and slider elements, various model elements were adopted implemented to fit the magneto-mechanical behaviours for MR materials, for example, Bouc-Wen model [17, 89], LuGre model [90] and Dahl model [15]. Bouc-Wen is the most acknowledged due to its high accuracy when addressing the nonlinearity in force-displacement hysteresis and frequently used in control system for adaptive MR devices. Although significant works on capturing the nonlinearity behaviours for MR behaviour have been carried out, there has no model proposed and validated for the dynamic hysteresis of MR gels.

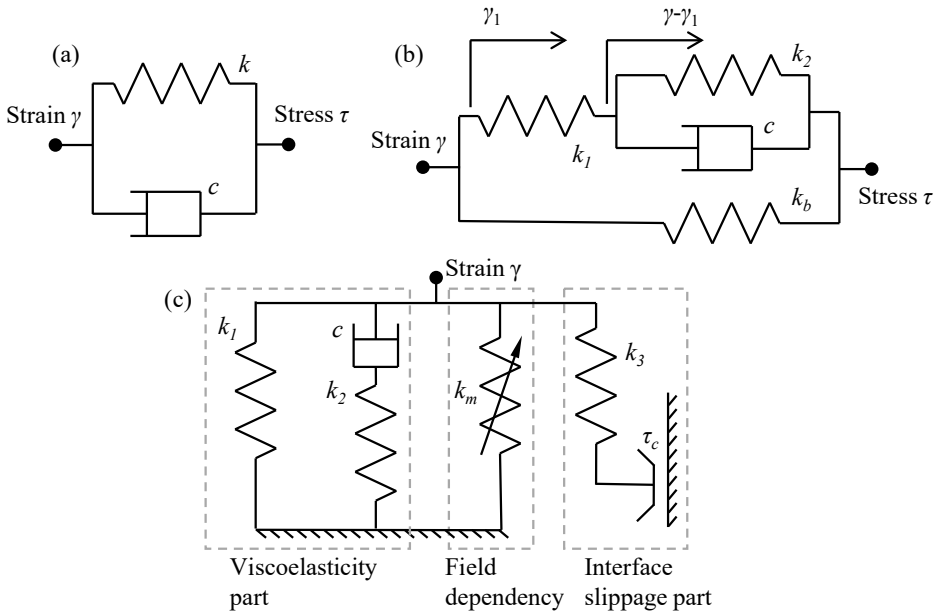

Fig. 2.13 Phenomenological models for viscoelastic materials (a) Kelvin-Voigt model (b) Four parameter MR elastomer model [55] (c) A field dependent rheological model [88]

2.5 Conclusions

This chapter presents a general review on the current development of MR materials (MR elastomer, MR fluid and MR gel), with special emphasis on the experimental characterisation and modelling. Based on this review, it can be concluded that MR materials have promising application potential for engineering industries, especially for civil engineering, involving seismic isolation and reduction for infrastructures. However, the current knowledge is not sufficient to deliver efficient and effective engineering applications. To date, MR elastomer devices still face with low MR effect and the energy consumption issue, and the improvements in the device design and analysis technique are of urgent demand. Moreover, as an improved system for both MR fluid and MR elastomer, MR gels start to attract research attentions in the recent year, but the lack of understanding and modelling of their dynamic behaviour and thixotropy impends MR gels from being widely adopted in engineering applications.

Chapter 3

Characterisation and Modelling of Isotropic and Anisotropic MR Elastomers

In this chapter a novel and compact material test rig featuring both permanent magnet (PM) and electromagnets was designed for MR elastomer shear tests. Finite element modelling was conducted using ANSYS Electronics Desktop to reveal the electromagnetic performance of the shear test rig. Isotropic and anisotropic MR elastomers with three different CIP volume percentages (17%, 22%, and 32%) were tested by the proposed test rig. The discussions on the influences of CIP volume fraction and microstructure of MR elastomer on the material performance were carried out. Furthermore, phenomenological modelling was conducted to predict the force-displacement relationships of both isotropic and anisotropic samples.

3.1 Introduction

MR elastomers exhibit fast and revisable changes of their material properties like stiffness and damping, upon the presence of an external magnetic field. The mechanical properties

of these are positively correlated to the strength of the external magnetic field. This unique feature has drawn numerous research and commercial interests; for instance, controllable devices have been developed and investigated to achieve adaptive seismic isolation, and structural control [11, 18, 59, 91, 92]. The performance of the aforementioned devices strongly depends on the MR elastomer material adopted. Therefore, understanding the behaviour of the MR elastomer is of significance and should be established prior to the device design in order to obtain a sufficient device performance.

The main MR elastomer components are silicone rubber, silicone oil and ferro-magnetic particles. Up to date, two types of MR elastomer can be characterized which are isotropic and anisotropic MR elastomers, depending on the microstructure formation of the materials. With the presence and absence of a magnetic field during the curing state of MR elastomer fabrication, anisotropic and isotropic MR elastomer can be obtained accordingly. The particles are uniformly distributed in the isotropic MR elastomer. However, the application of the magnetic field during the curing process aligns the ferro-magnetic particles thus forming columnar structures embedded in the elastomeric matrix [15]. This structure can be preserved in the MR elastomer after curing thus affecting the mechanical behaviour of the material like stiffness, damping and magnetorheological effect (MR effect) [93]. Not only the structure of the filling particles, but the volume of the iron particle is also an important character that influences the material properties of MR elastomer. Sun *et al.* measured the relative MR effect of MR elastomer samples with 60, 70, 80% weight fractions of Fe content and suggested that the 70%, which is equivalent to approx. 25% volume fraction, exhibits the highest relative MR effect [94]. In our research, the CIP volume fractions in MR elastomers are extended to 17, 22, and 32%.

The majority of the existing MR elastomer shear test rig and MR elastomer based adaptive device practices solely rely on permanent magnets or electromagnets to generate the magnetic fields, exhibit MR effect, and achieve adjustability of the material properties.

Dargahi *et al.* designed a shear test rig using permanent magnets to obtain the force-displacement relationships and the magnetic flux density was controlled by adjusting the number of permanent magnets (PMs) stacked together or the spacing between the PMs and the MR elastomer samples [80]. Using PMs to adjust the strength of the magnetic field cannot reach the same level of precision and accuracy as using the electromagnets. A large portion of shear test rig design features pairs of electromagnetic coils to realise a higher level of accuracy and precision than that of using PM [4, 93, 95-98]. However, this approach still has some limitations. For example, to generate a sufficient amount of magnetic flux, the number of winding and the applied current should be increased to a considerable value which will result in large size of coil and risk of applying high currents. Also, the overheating problem will be raised when the coils are working for a long time. Similarly, these issues are common to happen in the adaptive devices which have a single magnetic source. To mitigate the shortcomings of the devices with a single magnetic field source in the electromagnetic aspect, the concept of using hybrid magnets, i.e., PM and electromagnets have been brought into the development of magnetorheological materials based adaptive devices [19, 99, 100].

As an essential step towards the application development, modelling of MR elastomer are frequently investigated. The phenomenological model acts a major role to predict the force-displacement relationships of the materials, due to its versatile and simple formulation process. Li *et al.* developed a four-parameter model that accurately depicts the viscoelastic properties of MR elastomer [55]. Addressing the magnetic field dependency of MR elastomer, a generalised Prandtl-Ishlinskii model was constructed by Dargahi *et al.* to capture the magnetic-field-induced unique hysteresis behaviour for isotropic MR elastomers [80]. Reflecting on the strain stiffening effect generated by MR elastomer, Yu *et al.* proposed a phenomenological model which shows ideal fit with the experimentally characterised hysteresis behaviours of an MR elastomer based isolator [101].

3.2 Shear test rig featuring both PM and electromagnets

3.2.1 Design of the MR elastomer shear test rig

Fig. 3.1 (a) shows the schematic diagram of the proposed shear test rig. It includes a hybrid magnets system which features two electromagnetic coils and a PM. The size of the test rig is 200 mm × 180 mm × 85 mm. The dimension of PM and steel blocks is 35 mm × 35 mm × 5 mm. As shown in Fig. 3.1 (b), the shear plate contains a 45 mm × 70 mm × 15 mm copper block plate, two steel blocks and one PM. The copper block was extruded cut by a 35 mm × 35 mm square through the thickness direction to accommodate the stacked steel blocks and PM. Two fabricated MR elastomer samples and the shear plate were sandwiched between the left and right steel fixtures to form a double-lap structure. The MR elastomer samples were centred on the steel blocks and the fixtures. The size of the fixture is 62.5 mm × 35 mm × 35 mm. The two fixtures were bolted to the top of a c-shaped steel core to form an enclosed magnetic flux path. The two coils were installed on each branch of the steel core. Each coil contains 1900 turns of coated wire. The winding directions of the coils are opposite to each other to generate magnetic fluxes of the same clockwise or anticlockwise direction. N40 grade NdFeB PM was chosen for this test rig. Two load washers were installed at one end of the fixture to gauge the applied compression force to the MR elastomer samples before the left and right fixtures were bolted tight to the steel core.

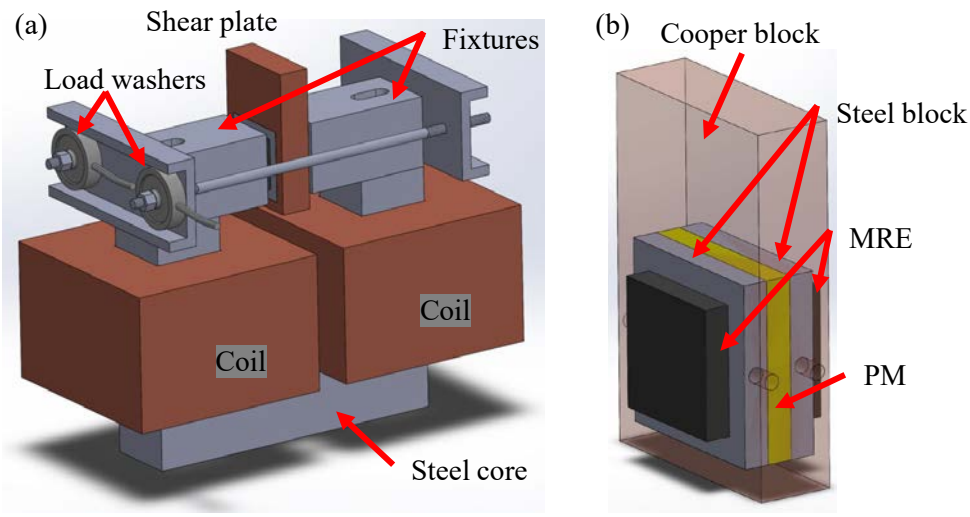

Fig. 3.1 Schematic diagram of (a) test rig (b) shear plate (MRE stands MR elastomer)

3.2.2 Finite element modelling

Finite element analysis (FEA) was conducted using ANSYS Electronics Desktop to characterize the static magnetic field distribution in MR elastomer samples under scenarios with different currents applied to the coils. The model was constructed following the designed test rig dimensions and materials. The N40 NdFeB PM was modelled with remanence $B_{\text{rem}} = 1.25\ \text{T}$ and coercivity $H_c = 9.5 \times 10^5 \text{Am}^{-1}$. The nonlinear B-H curves of MR elastomer and steel used in this finite element model are shown in Fig. 3.2. It should be noted that the B-H curve for MR elastomer used in this model is obtained from MRF-132DG magnetorheological fluid by Lord Corporation due to similar weight fraction of iron particle content and permeability of the matrix.

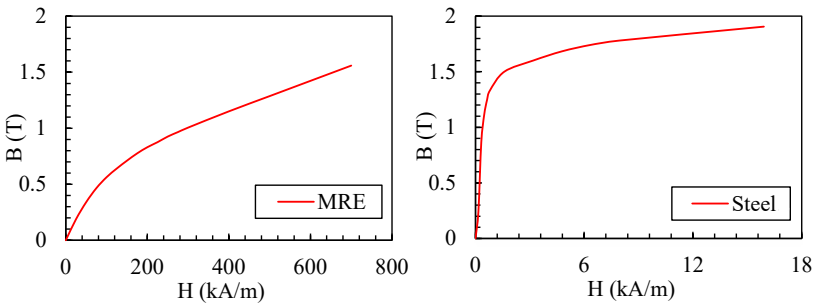

Fig. 3.2 B-H curve for MR elastomer and steel

Fig. 3.3 presents the FEA results for scenarios where the applied currents vary from 0.9 A, 0.66 A, 0.43A, 0.2 A, 0A and -0.45 A. It should be noted that upon the application of positive value current, the coils produce magnetic fluxes which travel opposing to the direction of the flux generated by the PM. Thus, the positive currents are meant to reduce the B values in the MR elastomer. As observed in Fig. 3.3(a), the flux density is almost zero (0.02T) at the positions of the MR elastomer samples. This indicates that the coils are capable of cancel out the 'bias' field provided by the PM with 0.9 A applied. By cutting down the applied to 0.43 A and 0 A, as shown in Fig. 3.3 (b) and (c), the flux density in MR elastomer samples rises to 0.54 T and 0.77 T, respectively. The relationship between flux density values in the MR elastomer sample and the applied current to each coil are summarized in Table 3.1.

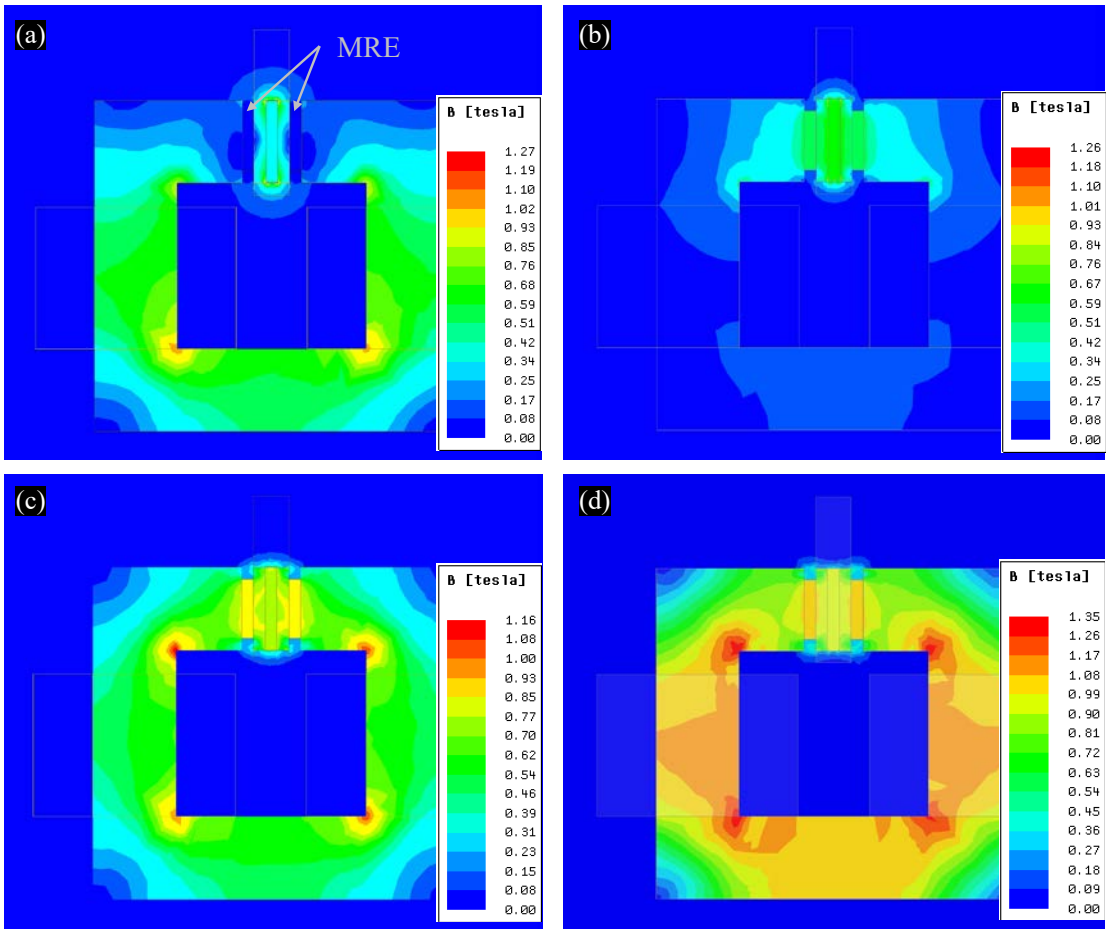

Fig. 3.3 FEA result for scenarios of (a) 0.9 A (b) 0.43 A (c) 0 A (d) -0.45 A (MRE stands MR elastomer)

Table 3.1 Flux densities in MR elastomer sample

Applied current [A]	Flux density [T]
-0.45	1.008
0	0.778
0.2	0.67
0.43	0.534
0.66	0.351
0.9	0.027

The flux density in the MR elastomer sample decreased to 0.02 T from 1.01T when the applied current increased from -0.45 A to 0.9 A. At 1.01T, the influence of the magnetic field to the adjustability of MR elastomer reaches saturation and this will be further validated by experiments in the following section.

3.3 Experiments

3.3.1 Material preparation

The materials required to produce the MR elastomer in this research are silicone elastomer base (SYLGARD 184, Dow Inc., United States), silicone oil (Type H201–500, Shanghai Hushi Co., Ltd., China) and 3-5 μm diameter CIP (Beijing Xing Rong Yuan Technology Co., Ltd., China). To fabricate isotropic MR elastomer, the first step is to mix and stir the silicone rubber and the silicone oil and CIP at 1000 rpm for 15 minutes. The weight ratio between the silicone rubber and silicone oil is 1:1. Then, the mixture was treated with an ultrasonic vibrator for 15 minutes to obtain a more uniform distribution of CIP and remove the air bubble in the mixture. To further eliminate the air bubble, the mixture was stored in the vacuum drying machine for 10 minutes. After this process, the mixture was cast into the mould and cured in the oven at 80 °C for 2 hours. Isotropic MR elastomer

can be obtained after curing. As for the preparation of anisotropic MR elastomer, the difference lies in the curing stage. 0.5 T magnetic field was generated by coils and applied to the mixture in the mould and the curing temperature was maintained at 80 °C for 2 hours by the heater. The direction of the magnetic field is parallel with the thickness direction of the samples. Thus, the formed chain-like structure also aligns with the thickness direction after curing. It should be noted that the material of the mould and the heater must be non-magnetic materials to ensure the uniformity of the magnetic field. A total of six types of MR elastomer samples were prepared and the details of the samples are summarised in Table 3.2.

Table 3.2 Details of MR elastomer samples

Material	MR elastomer type	CIP vol%	Width	Height	Thickness
iso17	isotropic	17%	25 mm	25 mm	5 mm
aniso17	anisotropic	17%			
iso22	isotropic	22%			
aniso22	anisotropic	22%			
iso32	isotropic	32%			
ansio32	anisotropic	32%			

3.3.2 Observation of microstructure

The microstructures of all six MR elastomer samples were viewed by scanning electron microscope (SEM) machine from Hitachi, Ltd. (model TM4000) at 500 times magnification with 15 kV accelerating voltage. Since the chain-like structures in the anisotropic samples are parallel with the thickness direction, the anisotropic samples were cut in the thickness direction prior to SEM observation. Fig. 3.4 shows the SEM micrographs of MR elastomer samples, where Fig. 3.4(a), (c) and (e) represents the results for the isotropic samples with 17%, 22% and 32% CIP volume fractions, respectively, and Fig. 3.4(b), (d) and (f) are for the micrographs of anisotropic samples with 17%, 22%, and

32% CIP volume fractions, correspondingly. It should be noted that the difference in the directions of the chain structure is due to the placing of the sample during SEM observation. For all anisotropic samples, the chains are parallel to the thickness direction of the sample. By comparing the results between isotropic and anisotropic MR elastomer samples, chain-like structures can be clearly observed in anisotropic samples. As the existence of the chain-like structures, the distances between CIPs are closer along the thickness direction for the anisotropic MR elastomer than that of isotropic materials.

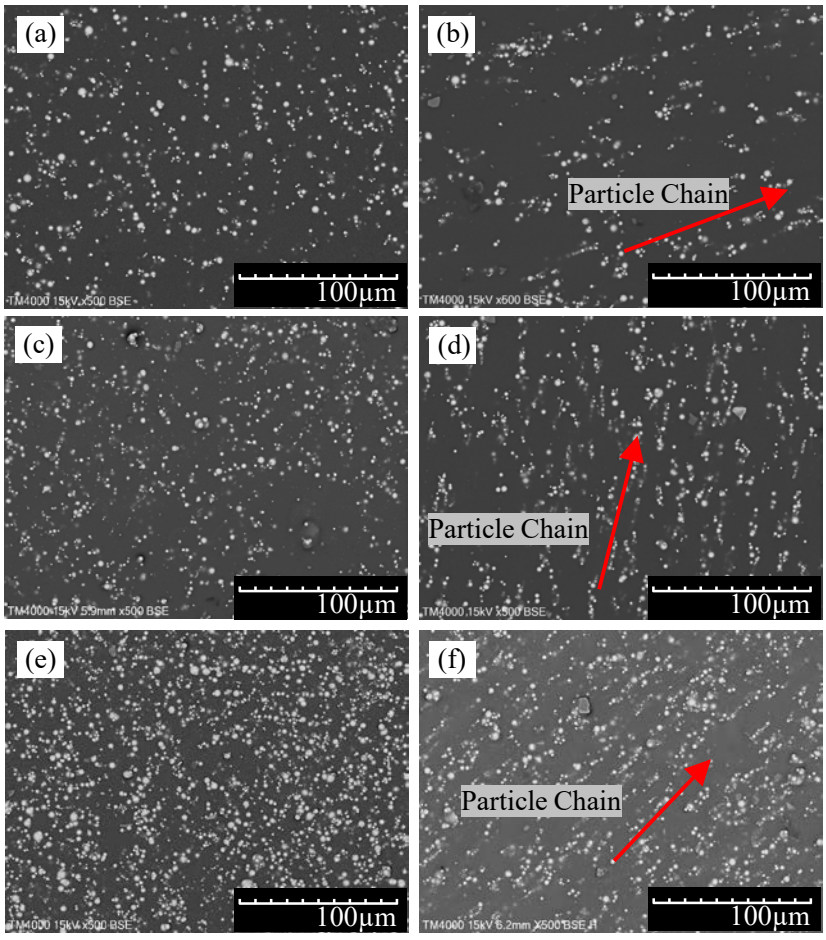

Fig. 3.4 Micrographs of (a) iso17 sample (b) aniso17 sample (c) iso22 sample (d) aniso22 sample (e) iso32 sample (f) aniso32 sample

3.3.3 Test set up

Experiments were conducted to obtain the dynamic behaviours of all six types of MR elastomer samples under various shear amplitude, excitation frequency and applied current. The test set up for the MR elastomer shear test is presented in Fig. 3.5. A universal testing machine (model: WAW-B, Jinan Shenggong Testing Machine Co., Ltd, China) was used for the experiments in displacement control mode. A load cell is adapted to the top of the shear plate. The other end of the load cell is connected to an adaptor which is gripped by the bottom crosshead. A linear variable displacement transducer (LVDT) was attached to the top crosshead to measure the displacement of the bottom crosshead. The two coils are connected to separate direct current power suppliers but are applied with identical current during the test.

The force-displacement hysteresis loops of the MR elastomer samples were recorded by using sinusoidal excitations with 0.1Hz, 0.5Hz, 1Hz and 2 Hz set as excitation frequencies and 1mm, 2mm and 3 mm chosen as amplitude. Considering the thickness of each MR elastomer sample is 5mm, 1mm, 2mm and 3 mm amplitudes are corresponding to 20%, 40% and 60% shear strain. The applied currents to the coils are 0.9 A, 0.66A, 0.43 A, 0.2 A, 0 A and -0.45 A, respectively. During each test, the universal testing machine produces an excitation signal at a fixed frequency and amplitude and the applied current was held at a constant level. Each test was repeated four times to ensure the reliability of the test results. Therefore, a total of 72 hysteresis loops were obtained for each type of material under the designed loading conditions and applied currents. The data acquisition device samples 500 data per second.

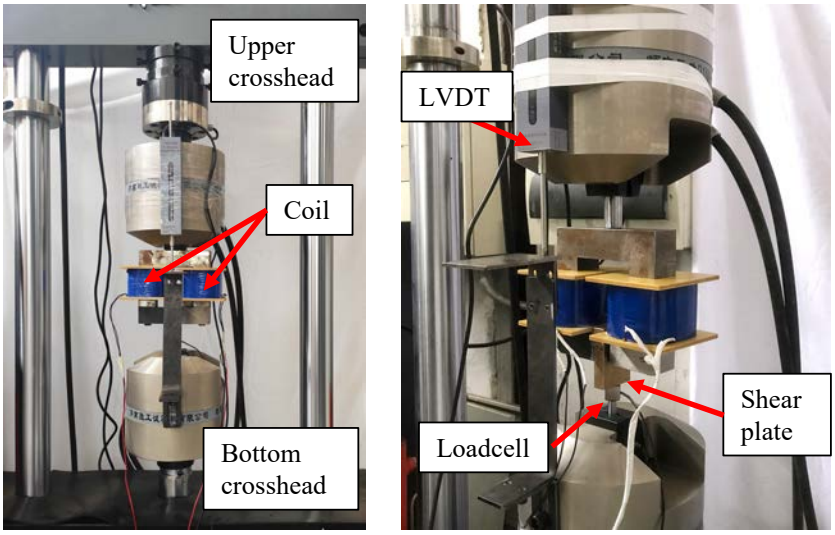

Fig. 3.5 Experimental set up

3.4 Experimental results and discussion

3.4.1 MR elastomer hysteresis characteristics

The measured force-displacement hysteresis loops showed that the hysteresis behaviour of MR elastomer samples is strongly affected by the excitation amplitude and magnetic field applied to the MR elastomer samples. Fig. 3.6 comparatively presented the effects of excitation frequency, amplitude and applied current for both isotropic and anisotropic MR elastomer samples. Due to the large amount of data, the measured hysteretic results for samples with the 17% CIP volume fraction were presented as examples. It should be noted that the forces in Fig. 3.6 are half of the measured forces, due to the double-lap configuration of the test rig.

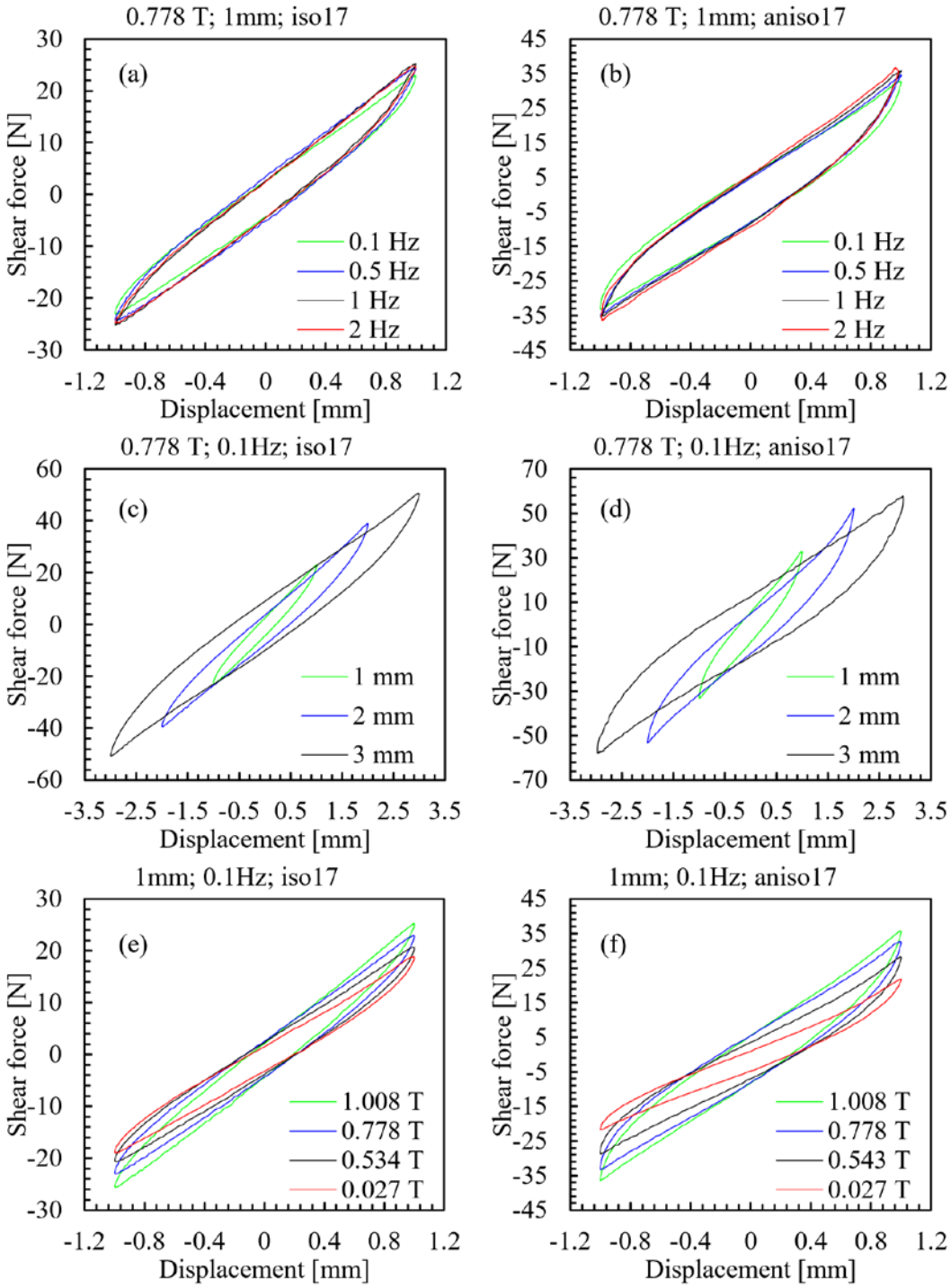

Fig. 3.6 Force-displacement hysteresis loops of (a) iso17 different frequencies (b) aniso17 different frequencies (c) iso17 different amplitudes (d) aniso17 different amplitudes (e) iso17 different fields (f) ansio17 different fields

From Fig. 3.6(a) and (b), which are responses of the isotropic and anisotropic MR elastomer under different excitation frequency, slight increases of maximum forces and dissipated energy (enclosed area of hysteresis loop) can be observed. This phenomenon is identical to the findings from the investigations conducted by [9]. Comparing the discrepancies of the performances between isotropic and anisotropic samples, under the same loading condition, the enclosed areas of the anisotropic sample are larger than that of the isotropic sample. This suggests the better energy dissipating property of anisotropic MR elastomer.

In Fig. 3.6(c) and (d), when running the shear excitations with different amplitudes, the areas of the dissipated and the maximum forces grow significantly with the increase of excitation amplitude. When adding of excitation amplitude, the maximum forces of isotropic sample grow steadily; whereas, the anisotropic has a much larger force increase when the amplitude grow from 1 mm to 2 mm than that of the increment from 2 mm to 3 mm. This indicates more linear mechanical properties of isotropic samples under the change of excitation amplitude when compared with anisotropic samples.

In Fig. 3.6(e) and (f), the increase of applied currents to the coils leads to reductions in dissipated energy and maximum force for both isotropic and anisotropic samples effectively. The effect of applied magnetic field on the anisotropic samples is greater than on the isotropic samples. This suggests the higher adjustability in the material performances of anisotropic samples. Owing to the pre-aligned CIP chain along the direction of magnetic fluxes in anisotropic samples, the distances between CIPs are shorter in the direction of fluxes than that in the anisotropic samples thus resulting in this significant improvement of MR effect for anisotropic samples [93].

The excitation frequency, amplitude and applied current have similar influences on the force-displacement hysteretic performance for both isotropic and anisotropic materials. Nevertheless, the anisotropic samples exhibit higher forces than that of isotropic samples

under the same excitation. With varying applied current, anisotropic samples have a larger range of adjustability. Differences in the shape of the hysteresis loops for the anisotropic and isotropic samples should also be noted. The slopes at the tips of hysteresis loops show an increasing trend for anisotropic samples, and this phenomenon is less obvious in the hysteresis loops of isotropic materials due to presence of pre-aligned CIP chain structure in anisotropic MR elastomer.

3.4.2 Effective stiffness

To further evaluate the influences of excitation inputs and magnetic fields on the material properties of all six types of MR elastomer samples, effective stiffness values were calculated from the hysteresis loops. Effective stiffness and its percentage change under the influence of magnetic can determine the adjustability of developed MR elastomer devices. Effective stiffness can be represented by Eq. 3.1 [11]:

$$K_{\mathrm{eff}} = \frac{F_{\mathrm{dmax}} - F_{\mathrm{dmin}}}{\Delta_{\mathrm{max}} - \Delta_{\mathrm{min}}} \tag{3.1}$$

where F_{dmax} and F_{dmax} are the forces measured at the maximum displacement (Δ_{max}) and minimum displacement (Δ_{max}) in one loading cycle, respectively. Fig. 3.7 illustrates the effects of applied current, excitation frequency and amplitude on the effective stiffness of MR elastomer samples. As observed in Fig. 3.7, anisotropic samples exhibit higher effective stiffness compared to the isotropic samples with the same CIP content under the same test condition. This trend matches well with the finding from the investigation of rheological properties of isotropic and anisotropic MR elastomer conducted by Lu *et al.* [93]. For samples with the same microstructure, higher CIP content results in higher effective stiffness. From Fig. 3.7(a), with the applied field increasing from 0.02 T to 1.01 T, the effective stiffness of all MR elastomer samples increase to the highest at 1.01 T. Anisotropic samples exhibited a larger range of stiffness change than isotropic samples

under the influence of applied current. However, in the scenario where the maximum current applied, the effective stiffness of ansio32 sample dropped to a lower value than that of the iso32 sample. For 17% and 22% CIP contents samples, the differences of effective stiffness between anisotropic samples and isotropic samples became smaller with the increase of applied current. Fig. 3.7(b) and (c) indicate that the effective stiffness of all MR elastomer samples is positively correlated to the excitation frequency and negatively corrected to the shear amplitude.

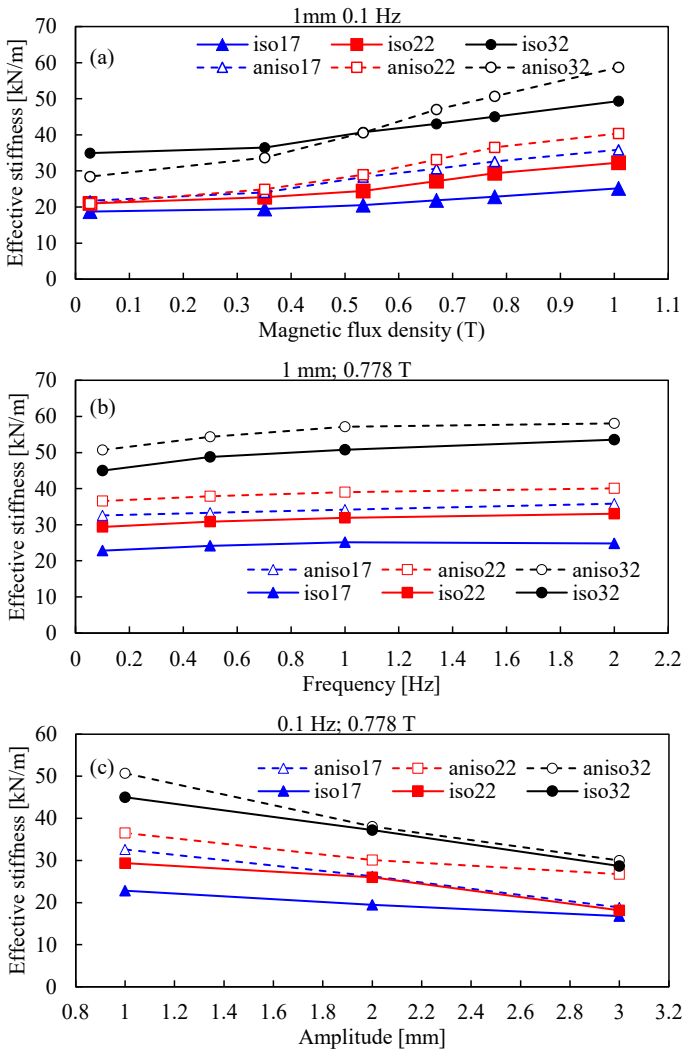

Fig. 3.7 Effective stiffness of MR elastomer samples under influences of (a) magnetic field (b) frequency (c) amplitude

Fig. 3.8 marks the percentage of increase of effective stiffness between the minimum (-0.45 A) and maximum (0.9 A) currents applied scenarios to quantitively analyse the adjustability of all six MR elastomer samples under various excitation inputs. In Fig. 3.8(a), which summarises the 0.1 Hz excitation scenario, anisotropic samples exhibit wider adaptive ranges that that of isotropic samples. Ansio32 has the highest increase% which is 106.61% under 1 mm and 0.1 Hz excitation; however, this value decreases to 25.90% as the amplitude increased to 3 mm. Though anisotropic samples have higher adjustability, more stable adaptive ranges can be observed in isotropic samples throughout the 1 mm to 3 mm amplitude range. This phenomenon could be explained by the difference between the microstructures in MR elastomer samples. In anisotropic samples, ferro-magnetic particles are closely lined up as columnar structures along the travelling direction of fluxes, as shown in Fig. 3.4(b), (d), and (f). When the columnar structures are subjected to the shear deformation perpendicularly, they become stretched; and, the distribution of CIP deviates significantly. As for isotropic sample, the filling particles are uniformly distributed in the elastomeric matrix. Since the magnetic forces between ferro-magnetic particles are highly dependent on the distance between the particles, the adjustability of the anisotropic samples become more dependent on the excitation amplitude than the isotropic samples. To present the influence of excitation frequency on the adjustability, Fig. 3.8(b) summarises the increase% against excitation frequency for the 1 mm amplitude scenario. Negligible influences of excitation frequency to the adaptabilities of all six types of MR elastomer samples can be observed.

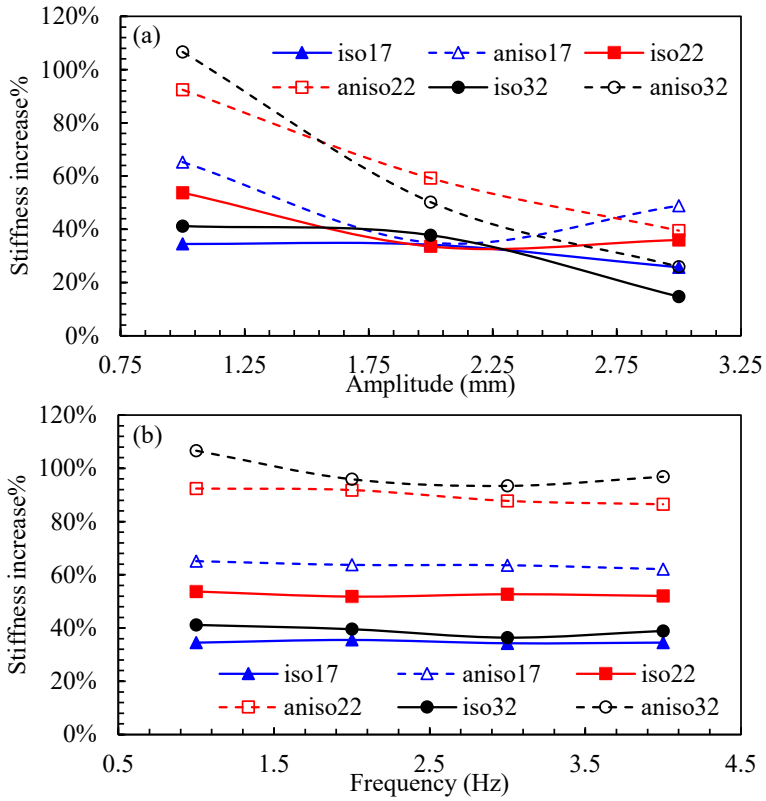

Fig. 3.8 Increase percentage of effective stiffness of MR elastomer samples under (a) different amplitudes 1 Hz (b) different frequencies 1 mm

3.4.3 Equivalent damping

Though the enclosed area of hysteresis loop indicates the energy dissipated during shear motion, equivalent damping was calculated to evaluate the performance of MR elastomer samples in terms of energy-dissipating ability, following Eq. 3.2 [11]:

$$C_{eq} = \frac{E}{2\pi^2 f A^2} \tag{3.2}$$

where E is the enclosed area of the corresponding hysteresis loop, f is the excitation frequency and A is the excitation amplitude.

Fig. 3.9(a), (b) and (c) show the variances of equivalent damping for six MR elastomer samples subjected to the influences of the applied field, excitation frequency and amplitude, respectively. The damping performances behave similarly to the effective stiffness which increases with the increases of the applied field; however, decreases with the increase of

excitation amplitude and frequency. Excitation frequency acts a significant role in the damping performance of MR elastomer samples. A sharp decreasing trend can be observed when the excitation frequency increases from 0.1 Hz to 2 Hz. It is worth noting that, at lower loading frequencies (0.1 and 0.5 Hz), the discrepancies of damping performances between different samples are apparent. Anisotropic samples have higher equivalent damping values than isotropic samples. Also, higher CIP percentage results in higher equivalent damping.

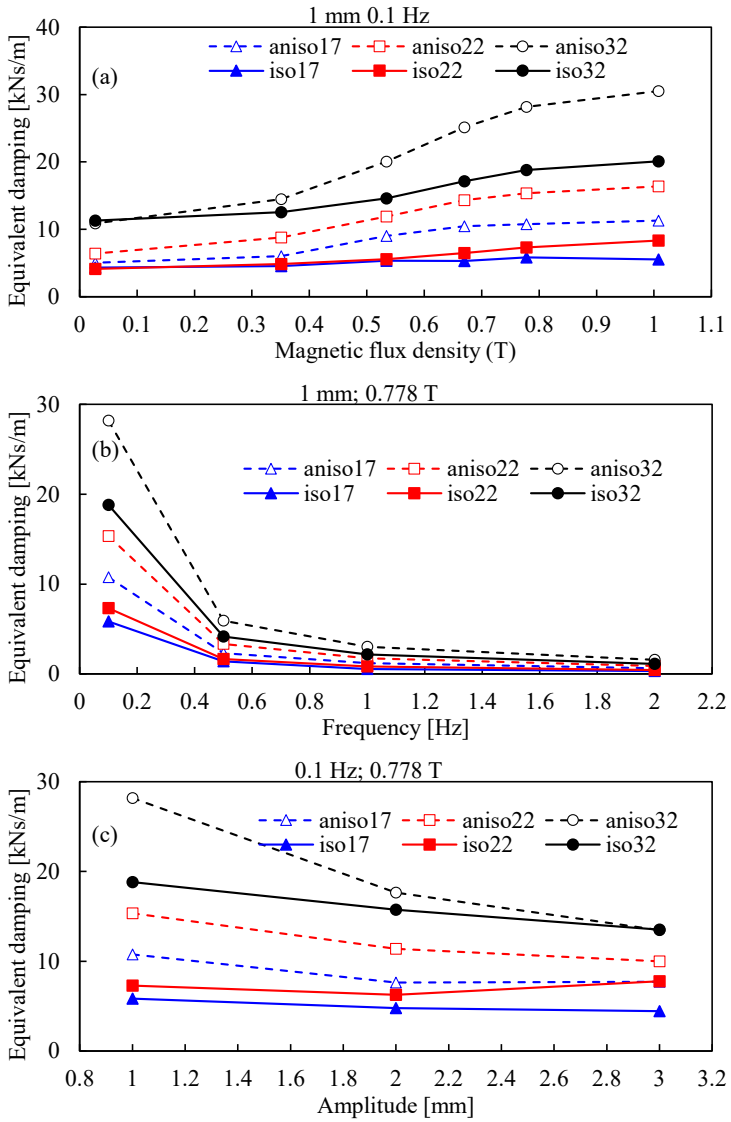

Fig. 3.9 Equivalent damping of MR elastomer samples under influences of (a) magnetic field (b) frequency (c) amplitude

3.5 Modelling of isotropic and anisotropic MR elastomer

The results of the MR elastomer shear test indicate that viscoelastic and strain stiffening are the two major features of both isotropic and anisotropic samples. With the intensifying of the magnetic field, the force-displacement hysteresis reflects a stronger stain stiffening effect. Hence, a simplification from the strain stiffening model proposed by Yu *et al.* was adopted in the modelling of the hysteretic responses for iso17 and aniso17 MR elastomer samples, as shown in Fig. 3.10 [101]. The model contains three parts which are an elastic spring element (k), damper viscous damping element (c) and the strain stiffening component. The F_0 term is not included in this model since the experiment was conducted after the initial shear force was eliminated by adjusting the crosshead of the material testing machine. The model is formulated as follow:

$$F = kx + c\dot{x} + a|x|x^3 \tag{3.3}$$

where F is the estimated shear force, x and $\dot{x}$ represent the displacement and velocity of the shear movement, and k, c, and a are the parameters for the linear spring, dashpot, and stress stiffening element, respectively.

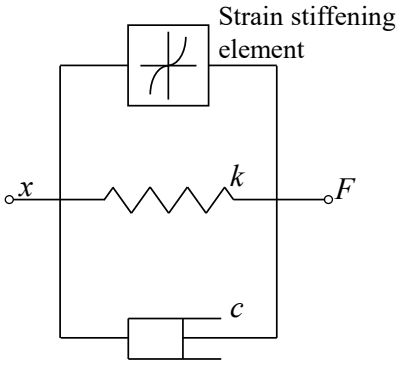

Fig. 3.10 The strain stiffening phenomenological model [19]

The combination of the model parameters, k, c, and a, that yields the minimum error between the estimated shear force and experimental data was solved by the least square method. Fig. 3.11 present the modelling results under the varying of excitation frequencies,

amplitudes, and magnetic fields for iso17 and ansio17 MR elastomer samples. The modelling results suggest that the unique stain stiffening effect and field-dependent viscoelastic properties of both isotropic and anisotropic samples can be well predicted by the stain stiffening phenomenological model under the excitation inputs and magnetic field considered.

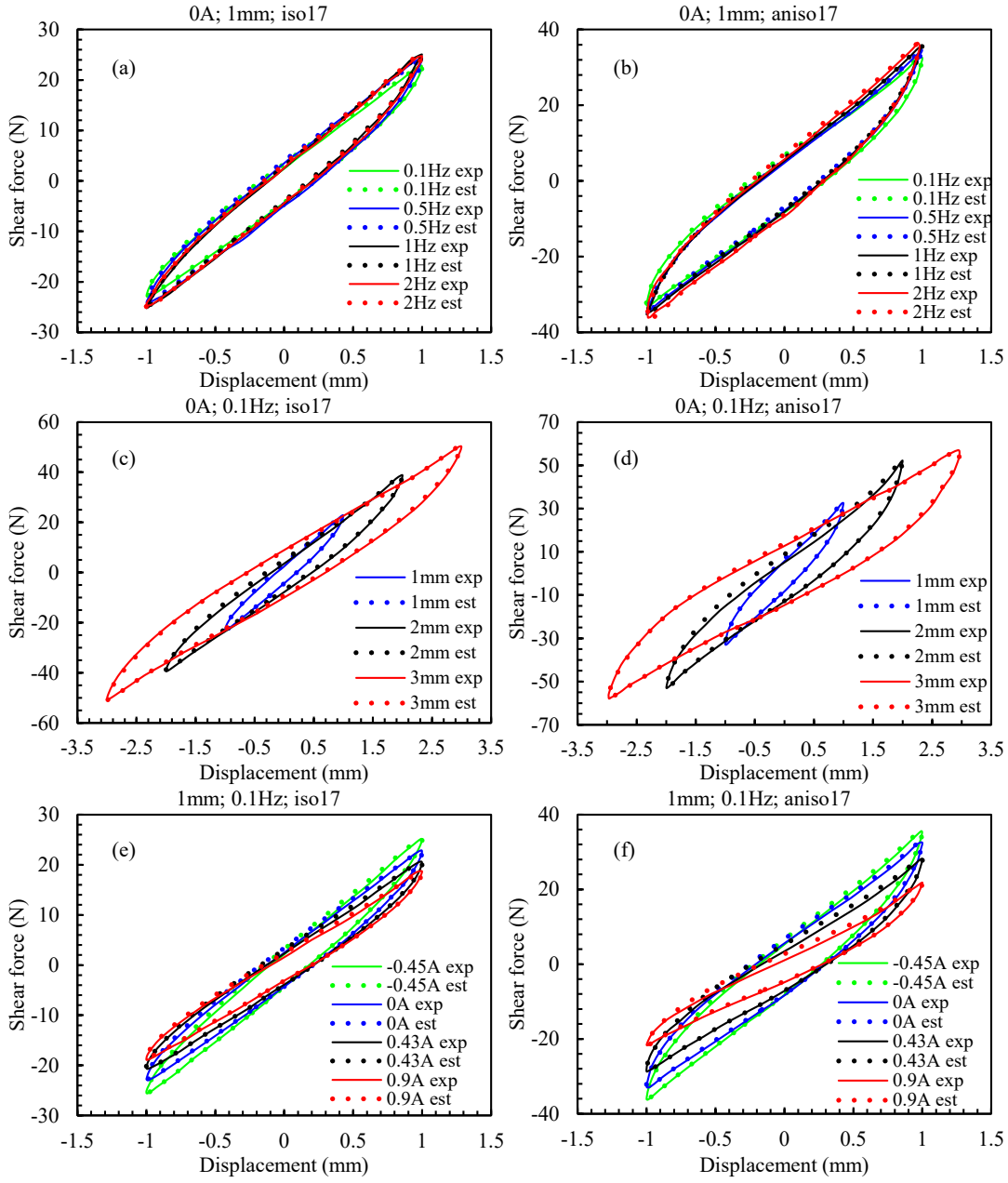

Fig. 3.11 Modelling results of (a) iso17 different frequencies (b) aniso17 different frequencies (c) iso17 different amplitudes (d) aniso17 different amplitudes (e) iso17 different fields (f) ansio17 different fields

The identified model parameters were further analysed to reveal their dependencies on the applied magnetic field. In Fig. 3.12 and Fig. 3.13, results from the parameter identification process for both iso17 and ansio17 samples are plotted to reveal the relationships between model parameters and the excitation frequency and the applied current. The parameters identified for isotropic and anisotropic showed identical and clear trends. For parameter k, as depicted in Fig. 3.12(a) and Fig. 3.13(a), with the value decrease with the increase of amplitude, but increase with the increase of excitation frequency. The reduce of applied current stands the intensifying of the magnetic field in the sample and increases the stiffness parameter. The damping parameter, c, values are summarised in Fig. 3.12(a) and Fig. 3.13(b).

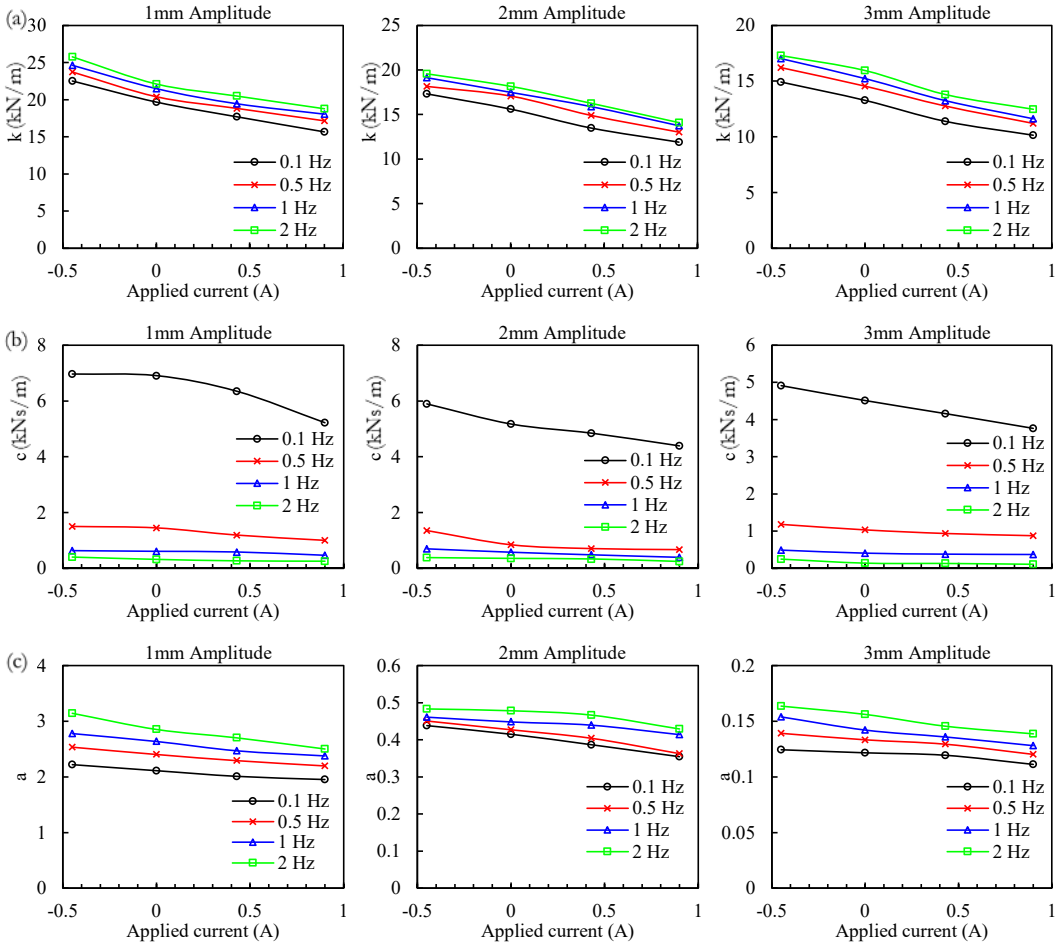

Fig. 3.12 Model parameters of iso17 samples (a) parameter k (b) parameter c (c) parameter a

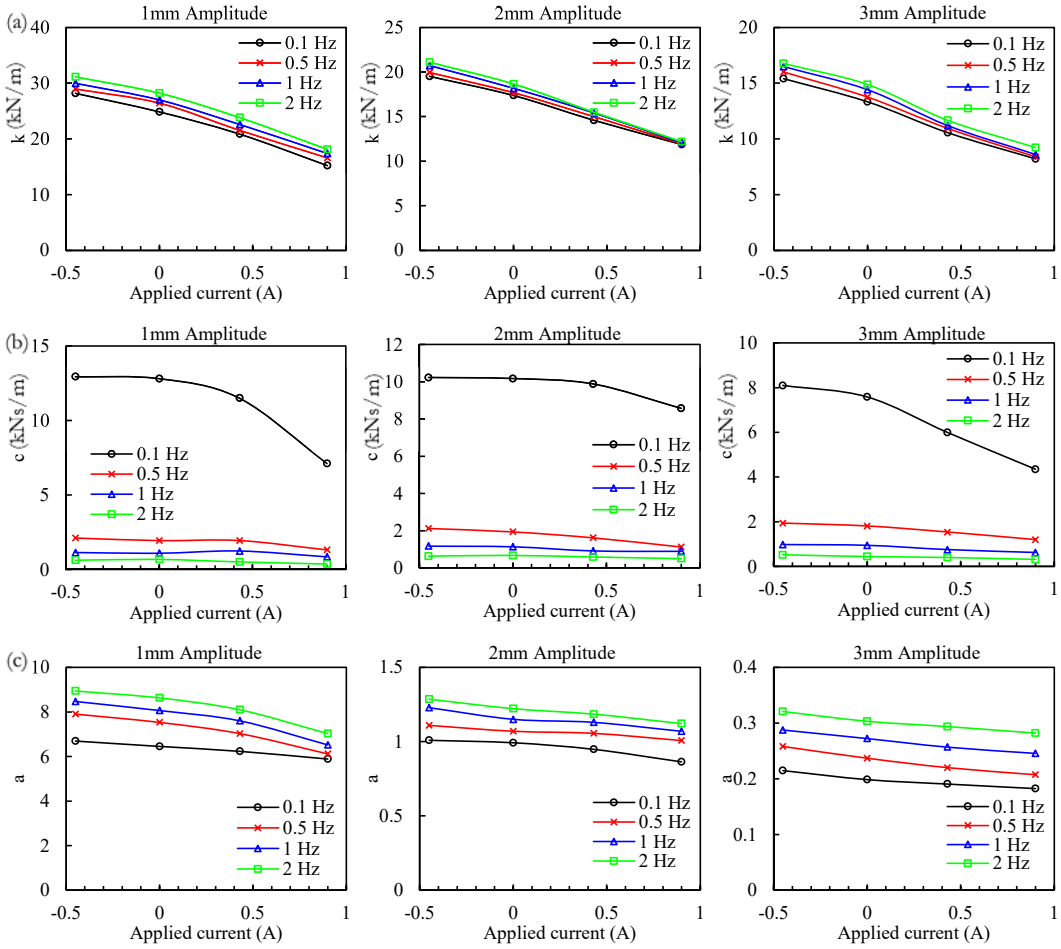

Fig. 3.13 Model parameters of aniso17 samples (a) parameter *k* (b) parameter *c* (c) parameter *a*

As the amplitude, excitation frequency and the applied current increase, the values of c decrease for both isotropic and anisotropic samples. These trends ideally agree with that of the calculated material properties, i.e., effective stiffness and equivalent damping, as discussed in section 3.4.3. As for the parameter *a*, which governs then magnitude of the strain stiffening effect, its value rises with the increase of excitation frequency and the intensifying of the magnetic field, however, decreases with the increase of excitation amplitude. For the isotropic sample, the smaller identified *a* value than that of the anisotropic sample well reflects the lower strain stiffening effect of isotropic MR elastomer.

3.6 Conclusion

This chapter presented a novel shear test rig that features a hybrid magnets system. The system consists of a set of electromagnet coils and a PM. The implementation of PM provides a magnetic field without power supply. In this way, the maximum electric current required to provide the maximum adjustability of the MR elastomer can be cut down and the overall energy consumption can be trimmed down. As the maximum applied current can be reduced, the risk of electric overload can be reduced; and more compact design of the coil can also be realised. These advantages suggest that adopting the hybrid magnets system can greatly enhance the reliability, compatibility and running time of the magnetorheological-material-based adaptive devices. Based on the hybrid magnets concept, the designed test rig provides a magnetic field with 0.77 T flux density when no power supplied to the coils. When the coils are energized, the variation range of flux densities can be altered from 0.02 T to 1.01 T. A series of MR elastomer shear tests were performed by using this shear test rig. Six types of MR elastomer were fabricated and tested, including isotropic and anisotropic samples with three different CIP volume fractions (17%, 22% and 32%). Results indicated that, when samples have the same CIP volume fraction, the anisotropic samples have higher stiffnesses, damping performances and better adjustability than that of the isotropic samples. Higher CIP content gives a higher effective stiffness and equivalent damping. The increase of excitation amplitude from 1 mm to 3 mm reduces the stiffness increase percentages from around 100% to 40% for anisotropic materials, and 50% to 30% for isotropic materials. Moreover, the force-displacement hysteretic behaviours of both isotropic and anisotropic MR elastomer can be well predicted by the strain stiffening phenomenological model effectively under the variances of excitation amplitude, frequency and applied current.

Chapter 4

Improved Magnetic Circuit Analysis of a Hybrid Magnet MR Elastomer Base Isolator

In this chapter, an improved magnetic circuit model approach to accurately analyse hybrid magnetic circuits involving laminated MR elastomer materials is proposed. The new approach considers the magnetic flux fringing effect and branched magnetic flux paths and is therefore able to produce effective and efficient estimation of the magnetic field in the device with complicated structure. With revealing the equations of the relationships between device design parameters and magnetic flux density values, this approach also greatly avails the optimization process at the device design stage. A laminated MR elastomer device featuring hybrid magnets was designed and manufactured as the benchmark case study. Accuracy of the improved magnetic circuit model is validated via finite element analysis results and experimental measurements.

4.1 Introduction

Dispersing ferromagnetic particles in elastomeric solids obtains a class of smart material normally termed MR elastomer [102]. It exhibits a unique and useful phenomenon which is tuneable material properties, i.e., stiffness and damping, upon the application of external magnetic field. Benefiting from this phenomenon, successfully applications have been reported in the fields of civil engineering [91, 103] and mechanical engineering [104, 105] for structural control and vibration reduction purposes; and, recently, its potentials have been further extended to developing sensors, robots and wearables [106-109].

One of the major branches of MR elastomer based application is isolators which can achieve adaptive isolation performance against different types of seismic conditions due to its tuneable stiffness and damping [110]. Drawing on the design of commercial laminated rubber bearings, the multi-layer configuration is normally adopted in MR elastomer isolators due to its excellence in carrying vertical loading with the minimal bulging effect in the elastomer layers. Li *et al.* developed the first adaptive base isolator with 47 layers of MR elastomer [11]. Based on this configuration, Li *et al.* further improved the adaptive range of base isolators by developing a highly adjustable base isolator with 1630% increase of lateral stiffness [59]. Harnessing the benefits of this highly adjustable isolator, Gu *et al.* constructed a real-time controlled smart seismic isolation system and conducted a series of concept-proof experiments with sound outcomes [111]. Following these successful developments, numerous research on the multi-layer structured MR elastomer isolators have been carried out. Xing *et al.* developed a novel base isolator with 20 layers of MR elastomer [112]. Although these applications all achieve sound vibration mitigation performances, solely relying on electromagnet coils to provide magnetic field for the devices brings significant thermal and energy consumption issues [113]. In the applications for base isolators or bridge bearings where higher lateral stiffness is required to resist small

disturbances like wind load and building live load in the majority of the service life, the coils in the device should be powered continuously [99]. Addressing these issues, the innovation of utilizing both electromagnet coils and permanent magnets (PM) has been proposed. The introduction of permanent magnets (PMs) provides MR elastomer devices with a "bias" magnetic field present when the electric current is zero, which can reduce energy consumption. A positive or negative electric current can be applied to increase or decrease the magnetic field and tailor the device properties. For example, hybrid magnets laminated MR elastomer adaptive isolators designed by Yang et al. [99] and Sun et al. [100] realized stiffness softening capability, maintaining stability without power during normal service life, and achieving effective base isolation during seismic events.

However, implementing the multi-layered structure and PM both adds difficulty and challenge to the design of device configuration and analysis of electromagnetic performance. For multi-layered structure, steel sheets with high relative permeability, which is normally around 5000, are chosen to bond with MR elastomer layers to give a higher magnetic conductivity. However, relative permeability of MR elastomer is usually as low as 1 to 7 [61]. Laminating these two types of material may result in magnetic fluxes leaking out from high permeability layers, forming unpredicted flux paths and irregular flux density distributions in the multi-layer structure. As for using PM, the complexities lie in the inhomogeneous magnetic field distribution on the PM surfaces and the prevention of irreversible demagnetization. Considering the strong magnetic field dependence of MR materials, revealing the magnetic field distribution inside of the laminated MR elastomer devices featuring hybrid magnets is critical and mandatory to achieve cost-effective and reliable designs. However, this cannot be achieved by experimental methods since current available magnetic field sensors are not capable of detecting the field distribution inside of a cured laminated structure without any structural modifications on the device. And

opening slots on the laminated structure to accommodate the sensor will cause the detour of magnetic flux path and unreliable measurements.

Numerically, standard practice is to undertake the design using finite element software, such as ANSYS Maxwell or COMSOL Multiphysics. However, the construction of FEA models requires comprehensive details of the device which are commonly not available at the initial design stage. To obtain an optimal design of an MR device often involves numerous rounds of trial-and-error. Another analysis approach in developing magnetorheological (MR) devices, namely magnetic circuit modelling (MCM), produces equational presentations of the relationships between the device performance and variables such as the magnetic field strength, material properties and dimensions of the components. MCM allows theoretical, quantitative analysis and optimization focusing on predominant design parameters without involving much effort in modifying the geometry of the design and physical properties of the used materials in the first place. MCM has been successfully used in developing, analysing, and optimizing MR fluid dampers [114-120], MR fluid actuators [121-123] and MR fluid valves [124-127].

However, MR fluid devices and MR elastomer devices should be treated separately when considering MCM as a design technique. For MR fluid devices, large damping force can be realized by controlling the flow of fluid through narrow channels permeated by the controllable magnetic field. Therefore, the magnetic path of MR fluid devices is normally simple and of small length-scale. Simple device configurations result in homogeneous magnetic field distributions in the MR fluid. In such configurations, the standard MCM assumptions of no branched magnetic flux paths and no flux fringing are accurate, and thus the conventional MCM method is viable. However, making these assumptions can dramatically degrade the accuracy and reliability in designing MR elastomer devices especially multilayer MR elastomer devices which include larger length-scale and branched magnetic flux paths. In addition, unlike the sealed structure of MR fluid devices, air gaps

and free spaces are usually allocated in MR elastomer devices to avoid friction or collision of moveable parts during shear movements. The existence of air gaps introduces considerable flux fringing effect and imposes design challenges as a consequence. Furthermore, the multilayer structure of MR elastomer devices results in inhomogeneous field distribution in the device. Wang et al. suggested a design methodology incorporating finite element analysis (FEA) to design an MR elastomer -based isolator featuring a ten-layered laminated conical-shaped core [128]. The magnetic field analysis showed that the average magnetic flux density varied over a factor 2 between the top and middle layers of MR elastomer. Xing et al. also pointed out substantial differences of magnetic flux density at different locations in the laminated structure of an MR elastomer bearing [112]. The inhomogeneous distribution of magnetic flux density among MR elastomer layers triggers different MR effects and causes discrepancies of mechanical performance of the devices. These phenomena suggest that the flux leakage and branched flux paths should be included in MCM for multilayer MR elastomer devices. Though structural complexities of MR elastomer devices imply challenges in implementing the MCM method, some pilot investigations have been conducted. Zhou [4] and Zhou et al. [57] iterated equational relationships between magnetic flux densities and device specifications of MR elastomer shear testing rigs through MCM. Böse et al. [129] adopted MCM for evaluating the performance of an MR elastomer valve. Yang et al. [130] computed the magnetic field distribution of a shear-compression mixed mode MR elastomer isolator by MCM and obtained close results to FEA. However, these existing MCM implementations for MR elastomer devices made the same no flux-fringing assumptions as adopted for MR fluid devices and no multilayer MR elastomer structures with a hybrid magnets configuration were investigated. Hence, this study develops a hybrid magnets multi-layer MR elastomer base isobar, for seismic mitigation of buildings and bridges, as a prototype device. To

provide design and analysis guidance, an improved MCM is proposed and validated with results from conventional MCM, FEA and experimental results.

4.2 Description of the benchmark device

Fig. 4.1 shows the schematic diagram and a half of the section view with the illustration of the main flux paths of the proposed hybrid MR elastomer isolator. The main body of the device adopts the proven design by Li et al. [11] which is able to produce a good level of magnetic field across the MR elastomer layers. That design is modified by the inclusion of a PM of thickness 5 mm and diameter 100 mm, sandwiched in the middle of the steel laminated MR elastomer core. 9 layers of MR elastomer and 9 layers of steel are laminated alternatively and bonded on both sides of the PM. The first layer attached to each of the two pole faces of the PM is steel. All steel and MR elastomer layers are 1 mm thick. A 5 mm air gap between top plate and steel yoke allows horizontal movement. Steel cylindrical blocks of height 37 mm were positioned between the MR elastomer core and the top and bottom plates. Ten small coils, each having 350 turns, are stacked together, and connected in parallel to a power supply. Detailed specifications for each component of the isolator are listed in Table 4.1.

Two magnetic field sources are specified in the device, namely the PM and the coil. When no current is applied to the coil, magnetic field is sourced from the PM. In this way, the MR elastomer layers will maintain a higher stiffness without requiring any external electric power supplied to the device. The magnetic flux generated by the PM travels through the laminated MR elastomer core, steel parts and the air gap, forming the major magnetic flux travel path. The intended current direction in the coil is such as to create magnetic flux opposing the magnetic flux generated by the PM hence reducing the magnetic flux densities in the MR elastomer layers. The stiffness of the MR elastomer material therefore

decreases. Hence, softening and adaptability can be achieved by applying and varying the current supplied to the coil.

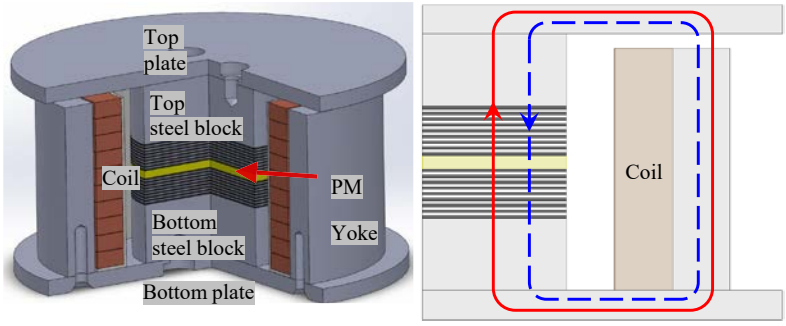

Fig. 4.1 Overview and schematic (not to scale) of the proposed isolator. The fluxes generated by the coil and the PM are represented by the blue dashed line and the solid red line, respectively (MRE stands MR elastomer)

Table 4.1 Specifications of the components of the isolator

	Material	Quantity	Axial Height (mm)	Diameter (mm)
Steel Block	Steel 1008	2	37	100
Steel Plate	Steel 1008	2	10	250
Yoke	Steel 1008	1	110	180 (inner); 220 (outer)
Steel Sheet	Steel 1008	18	1	100
MR elastomer	MR elastomer	18	1	100
PM	N40 NdFeB	1	5	100

4.3 Conventional MCM analysis

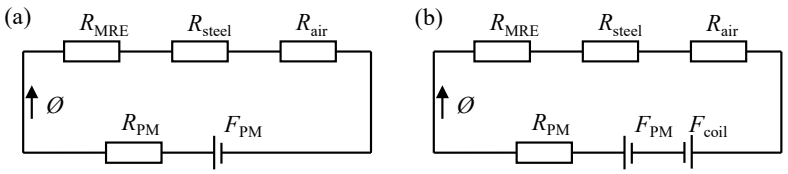

Fig. 4.2 Magnetic circuit models without considering magnetic fringing (a) without current applied (b) with current applied (MRE stands MR elastomer)

On the assumption that no fringing is considered, conventional MCM for the proposed isolator can be depicted as Fig. 4.2. By assuming all components of the isolator are in series connection, the same flux travels through every part and is equivalent to the total flux $Ø$. The hybrid magnetic circuit, Fig. 4.2(b), features the superposition of a magnetomotive force (MMF) from the PM, denoted F_{PM}, and an MMF from the coil, denoted $F_{coil,}$ which operates in the opposite direction to that of F_{PM}. MMF values for PM and coil can be calculated by Eq. 4.1:

$$\begin{aligned} F_{\mathrm{PM}} &= H_c l_{\mathrm{PM}} \\ F_{\mathrm{coil}} &= Ni \end{aligned} \tag{4.1}$$

where H_c is the coercivity of the PM, l_{PM} is the magnet thickness, N is the total number of turns of the coil, and i is the current in each turn. Since all components are in series, the total circuit reluctance is the sum of the reluctances for each type of material, R_{MRE}, R_{steel}, R_{airgap}, and R_{PM}, which are given by Eq. 4.2:

$$\begin{aligned} R_{\mathrm{MRE}} &= nl_{\mathrm{MRE}}/(\mu_{\mathrm{MRE}}A_{\mathrm{MRE}}) \\ R_{\mathrm{airgap}} &= l_{\mathrm{airgap}}/(\mu_{\mathrm{air}}A_{\mathrm{airgap}}) \\ R_{\mathrm{PM}} &= l_{\mathrm{PM}}/(\mu_{\mathrm{PM}}A_{\mathrm{PM}}) \\ R_{\mathrm{steel}} &= l_{\mathrm{yoke}}/(\mu_{\mathrm{yoke}}A_{\mathrm{yoke}}) + 2l_{\mathrm{plate}}/(\mu_{\mathrm{plate}}A_{\mathrm{plate}}) + 2l_{\mathrm{block}}/(\mu_{\mathrm{block}}A_{\mathrm{block}}) + \\ & nl_{\mathrm{steel\ sheet}}/(\mu_{\mathrm{steel\ sheet}}A_{\mathrm{steel\ sheet}}), \end{aligned} \tag{4.2}$$

where MRE stands for MR elastomer, n is total layer number of MR elastomer, also equal total number of steel sheet layers, l is the flux path length through each element, A is the flux cross-sectional area of each element, and $\mu = \frac{B}{H}$ is the element permeability, for H the magnetic field and B the magnetic flux density. For air, $\mu = \mu_0$. The N40 NdFeB magnet was assumed to have linear B-H curve in the second quadrant with remanence $= 1.25\ \mathrm{T}$ and coercivity $H_c = 9.5 \times 10^5 \mathrm{Am}^{-1}$. The magnet is modelled as a cylindrical surface current of density H_c around the magnet perimeter with the interior of the magnet treated

as having permeability $\mu_{\mathrm{PM}} = \frac{B_{\mathrm{rem}}}{H_{\mathrm{c}}} = 1.3158 \times 10^{-6}\mathrm{Hm}^{-1} = 1.047\mu_0$. The relationship between B and H for steel and MR elastomer are presented in Fig. 3.2 and symbolically expressed in Eq. 4.3:

$$\begin{aligned} H_{\mathrm{steel}} &= f_{\mathrm{steel}}(B_{\mathrm{steel}}) \\ H_{\mathrm{MRE}} &= f_{\mathrm{MRE}}(B_{\mathrm{MRE}}) \end{aligned} \tag{4.3}$$

B in each element is related to the flux and the element cross-sectional area by:

$$\emptyset = BA. \tag{4.4}$$

For the top and bottom plates of this circuit, *A* varies with radius. For the plate thickness chosen, the largest cylindrical cross-sectional area was smaller than the planar areas where the flux entered and exited the plate. The cylindrical cross-sectional area at the average of the inner yoke radius and the block outer radius was used. As a check against saturation, the MCM was repeated using the smallest area, at the block outer radius, and the results were found to change insignificantly. The calculations of the *A* and *l* values are specified in Appendix A.

The mathematical expressions of the magnetic circuit models constructed in Fig. 4.2(a) and (b) can be expressed as Eq. 4.5 and Eq. 4.6, respectively:

$$F_{\mathrm{pm}} = H_c l_{\mathrm{PM}} = \sum f_{\mathrm{steel}}\left(\frac{\emptyset}{A_i}\right) l_i + \sum f_{\mathrm{MRE}}\left(\frac{\emptyset}{A_i}\right) l_i + \frac{\emptyset l_{\mathrm{airgap}}}{\mu_{\mathrm{air}} A_{\mathrm{airgap}}} + \frac{\emptyset l_{\mathrm{PM}}}{\mu_{\mathrm{PM}} A_{\mathrm{PM}}} \tag{4.5}$$

$$\begin{aligned} F_{\mathrm{pm}} - F_{\mathrm{coil}} &= H_c l_{\mathrm{PM}} - Ni \\ &= \sum f_{\mathrm{steel}}\left(\frac{\emptyset}{A_i}\right) l_i + \sum f_{\mathrm{MRE}}\left(\frac{\emptyset}{A_i}\right) l_i + \frac{\emptyset l_{\mathrm{air}}}{\mu_{\mathrm{air}} A_{\mathrm{airgap}}} + \frac{\emptyset l_{\mathrm{PM}}}{\mu_{\mathrm{PM}} A_{\mathrm{PM}}} \end{aligned} \tag{4.6}$$

By substituting specifications and dimensions of each part of the isolator, the main flux *Ø* is obtained and can be converted to magnetic flux densities distributed in each element through Eq. 4.4. Summarising Appendix A, Table 4.2 lists the MCM parameters of the isolator elements.

Table 4.2 Conventional MCM parameters for the MR elastomer isolator

	n	l (mm)	A (mm^2)
Steel Block	2	37	7853.98
Steel Plate	2	110	4398.23
Yoke	1	110	12566.37
Steel Sheet	18	1	7853.98
MR elastomer Sheet	18	1	7853.98
Air Gap	1	5	12566.37
PM	1	5	7853.98

Results from the conventional MCM for current applied to each small coil ranging from 0 A to 1.357 A are presented in Fig. 4.3. The magnetic flux densities in all MR elastomer layers is seen to decrease from 0.49 T to 0 T when the applied i increased from 0 A to 1.357 A. For the total number of turns N = 3500, 1.357 A current gives 4750 Aturns MMF of the ten coils (where Aturns is the product of the current times the number of turns) which is equal to the MMF of the PM, $H_c l_{PM}$, therefore, at this current, the magnetic field of the PM is cancelled out theoretically by the field generated by the coil. Although this method provides rapid solutions for estimating electromagnetic properties, the assumptions include ignoring the flux leakage and fringing effects; hence the amount of flux travelling throughout the entire circuit model is constant and flux density values are identical for components sharing the same A value. Hence, for the laminated core area, flux density values in MR elastomer sheets and steel sheets are the same, which is an inaccurate description of the magnetic flux density distribution for devices featuring laminated cores.

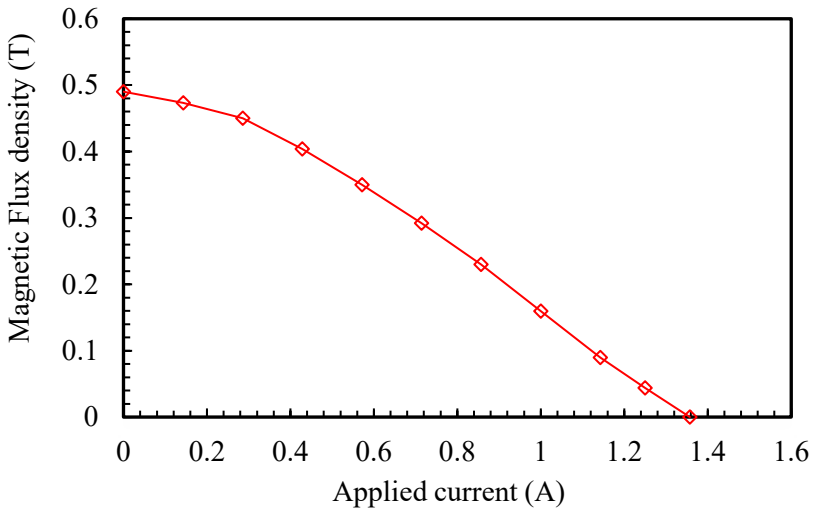

Fig. 4.3 Magnetic flux density in MR elastomer from MCM without considering fringing effect

4.4 FEA results

An axisymmetric finite element model of the prototype hybrid magnetic isolator was constructed and analysed through ANSYS Electronic Desktop. The software solved for the azimuthal component of the magnetic vector potential. Isotropic permeability was assumed for all materials. The N40 NdFeB magnet was assumed to have linear B-H curve in the second quadrant with remanence $B_{\text{rem}} = 1.25$ T and coercivity $H_c = 9.5 \times 10^5 \text{Am}^{-1}$. Solutions for current applied to each small coil, *i*, ranging from 0 A up to 1.357 A, at values corresponding to current MMF values 0 Aturns, 1000 Aturns, 2000 Aturns, 3000 Aturns, 4000 Aturns and 4750 Aturns, were computed in Fig. 4.4. Due to the axial symmetry of the device, ½-axisymmetric presentations of the magnetic flux density (B) plots are shown. Fig. 4.4(a) shows the B plot for 0 A in the coil, i.e., with the PM as the magnetic source. Magnetic flux fringing can be clearly observed at the air gap and around the laminated core area. Fig. 4.4(b)-(f) show the results as the *i* increases up to 1.357 A.

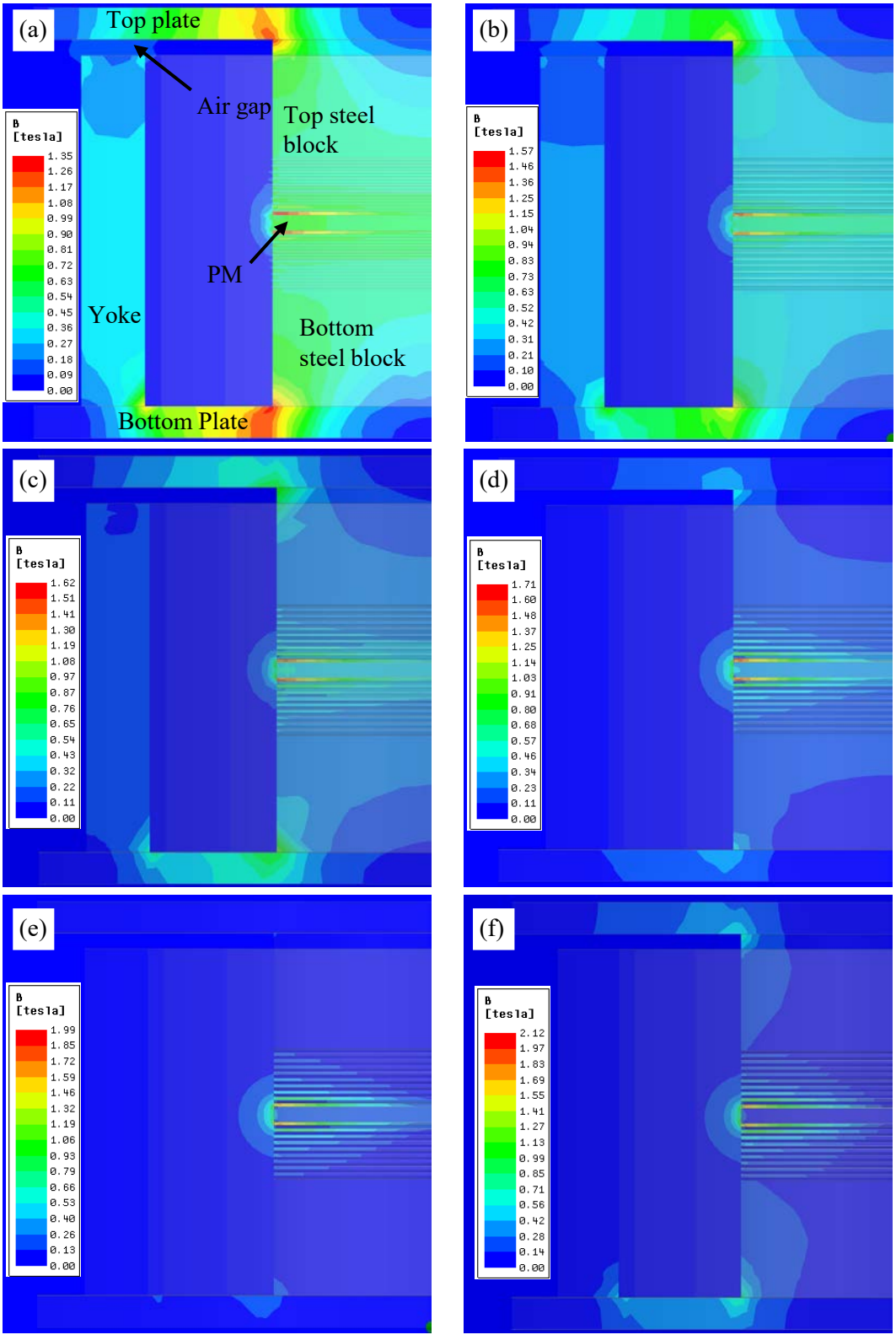

Fig. 4.4 Magnetic flux density plot from FEA (a) $i = 0$ A (b) $i = 0.286$ A (c) $i = 0.571$ A (d) $i = 0.857$ A (e) $i = 1.143$ A (f) $i = 1.357$ A

The FEA-calculated average flux density in each layer of the laminated core structure with different *i* applied is presented numerically in Table 4.3. The top MR elastomer and steel sheets (furthest from the magnet on the air gap side) are numbered as the 9th layer and marked as M9 and S9 respectively. For zero current, the average magnetic flux density in the MR elastomer layers decreases with distance away from the PM, falling from 0.58 T in the first MR elastomer layer near the PM to 0.51 T in the furthest MR elastomer layer from the PM. By comparing the FEA results with results from conventional MCM analysis, four major discrepancies are observed:

- The conventional MCM analysis only produces the amount of total flux travelling through the single flux path. The elements sharing the same cross-sectional area have the same flux density under these assumptions. For zero current in the coil, that *B* value is 0.49 T for every layer of the core structure including steel sheets, MR elastomer sheets and PM. However, FEA showed an inhomogeneous distribution of magnetic flux density, with average *B* value varying from 0.63 T in the PM layer to 0.51 T in the top MR elastomer layer.
- The conventional MCM analysis cannot capture the vector property of magnetic flux density. For example, in FEA, high magnetic flux densities were observed in the 1st and 2nd steel layers, namely 1.04 T and 0.70 T respectively. These values are unusual according to the conventional MCM since the flux density produced within the PM is 0.63 T. However, the explanation lies in the vector property of magnetic field: besides the longitudinal magnetic flux density component, there are the fringing magnetic fluxes leaking along the radial direction of the steel layers and the 1 mm thickness gives a narrow magnetic flux path. As a result, the small amount of fringing flux produces a high radial flux density component which contributes to produce high total magnetic flux density values in the steel layers. Within each MR elastomer sheet, the flux density is nearly all longitudinal

and is close to uniform in amplitude across the layer. However, in the steel sheets, the high permeability allows the flux a low reluctance radial path to the outer perimeter of the sheet and, especially for the 1st and 2nd steel sheets, a short leakage flux path to the other side of the PM.

- When the applied current in the coil increases to the equivalent amount of F_{PM}, the coil offsets the net magnetic flux density to 0 T everywhere in the conventional MCM. However, the FEA shows that in fact a flux density of 0.11 T remains in the PM. Associated with the magnetic fringing flux, the average flux density values in the 1st and 2nd steel layers still remained as high as for zero current in the coil.
- Flux fringing can also be observed at the air gap between the top plate and the yoke. In conventional MCM, the air gap is represented by a cylindrical annulus with the same inner and outer diametric as the yoke. However, as shown in the FEA magnetic flux density plot, instead of travelling straight across the modelled air gap, the flux fringes to a larger area. Referring to equation (2), this will result in an error in estimating the reluctance of the air gap and therefore output an unreliable MCM result.

Table 4.3 Average flux densities (T) in each layer of the core structure

	0 A	0.286 A	0.571 A	0.857 A	1.143 A	1.357 A
M9	0.51	0.40	0.28	0.14	0.00	0.10
S9	0.51	0.40	0.29	0.17	0.10	0.15
M8	0.51	0.40	0.28	0.15	0.01	0.09
S8	0.52	0.41	0.30	0.19	0.12	0.17
M7	0.51	0.40	0.28	0.15	0.02	0.09
S7	0.52	0.42	0.31	0.21	0.15	0.18
M6	0.52	0.41	0.29	0.16	0.03	0.08
S6	0.53	0.43	0.33	0.23	0.18	0.20
M5	0.52	0.42	0.30	0.17	0.04	0.06
S5	0.55	0.45	0.35	0.27	0.22	0.24
M4	0.53	0.43	0.31	0.18	0.05	0.05
S4	0.57	0.48	0.39	0.31	0.28	0.30
M3	0.54	0.44	0.32	0.20	0.07	0.04
S3	0.60	0.53	0.45	0.41	0.40	0.42
M2	0.56	0.45	0.34	0.21	0.09	0.02
S2	0.70	0.66	0.62	0.67	0.71	0.75
M2	0.58	0.47	0.36	0.24	0.12	0.04
S1	1.04	1.02	0.99	1.03	1.02	1.04
PM	0.63	0.54	0.43	0.32	0.20	0.11

4.5 The proposed MCM analysis

The discrepancies above originate from the overly simplified assumptions adopted, such as single magnetic path with no fringing, simple air gap path, etc. A modified approach should be constructed in order to obtain more accurate magnetic field distributions. In the following, several modifications are applied in the proposed MCM, including modelling flux fringing in the air gap and around the magnet.

4.5.1 Modelling of the air gap

Referring to the Eq. 4.2 to 4.5, due to the low permeability of air, the estimation made of the air gap cross-sectional area can dramatically affect the accuracy of the MCM. A smaller air gap cross sectional area leads to a higher reluctance value of the air gap element and a lower total amount of flux. In the conventional MCM, the magnetic flux is assumed to travel through the air gap along the shortest path, i.e., on straight field lines. However, as shown in Fig. 4.4(a), the flux travels in an expanded area at the air gap. The flux travel path at the air gap is observed to be about 10 mm wider than the thickness of the yoke. This matches closely with the air gap model proposed by Roters [131] which is shown in Fig. 4.5(a). In his model, the width of air gap element between two steel poles of equal width is extended for two times the gap height *g*. Although the greater lateral extent of the top plate would increase the actual air gap enlargement somewhat, the same enlargement of the air gap width on each side by the gap height *g* is assumed for the prototype isolator, as illustrated as Fig. 4.5(b). Since the yoke is a tubular component, the air gap should also be modelled as tubular and its cross-sectional area can be formulated as follows in terms of the yoke inner and outer diameters:

$$A_{\text{airgap}} = \pi \times \left(\frac{\emptyset_{\text{yoke outer}}}{2} + g\right)^2 - \pi \times \left(\frac{\emptyset_{\text{yoke inner}}}{2} - g\right)^2 \tag{4.7}$$

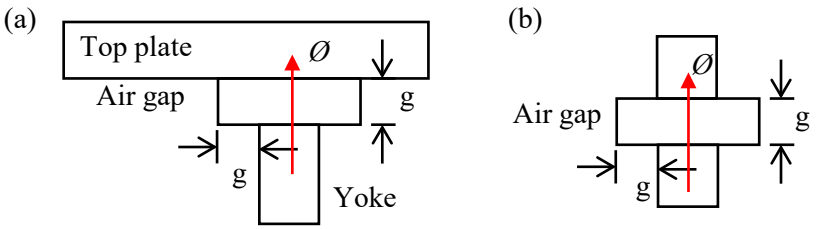

Fig. 4.5 Air gap models (a) gap model proposed by Roster [131] (b) air gap model for the proposed isolator

4.5.2 MCM with consideration of flux fringing

In addition to the modified air gap model, the modelling of the laminated core structure is also improved in the proposed MCM method. Considering the vector property of magnetic flux, the fluxes dispersed in each cylindrical layer in the laminated core structure can be categorised into two dimensions which are normal flux ($Ø$) and radial flux ($Ø'$) as shown in Fig. 4.6. Normal flux is taken as the flux passing across the disk top surface of each element while radial flux is the flux leaked out through the side surface of the element in the radial direction. By the principle of magnetic flux conservation, the difference of the fluxes crossing the top and bottom surfaces of a layer must equal the flux leaked out the side of the layer. Because the permeability of MR elastomer is much lower than that of steel and the radial path across the sheets is quite long, the radial flux leakage for the MR elastomer sheets is ignored, i.e., approximated as 0. The difference in $Ø$ between the adjacent MR elastomer layers equals the $Ø'$ of the steel layer in between them. Denoting the total amount of flux generated by the PM, the normal flux in the i^{th} MR elastomer layer and the leakage flux in the i^{th} steel layer are denoted as $Ø_{PM}$, $Ø_i$ and $Ø'_i$ respectively, their relationships are represented as Eq. 4.8:

$$\begin{aligned} \emptyset_{PM} &= \emptyset_1 + \emptyset_1' \\ \emptyset_i &= \emptyset_{i+1} + \emptyset_{i+1}' \end{aligned} \tag{4.8}$$

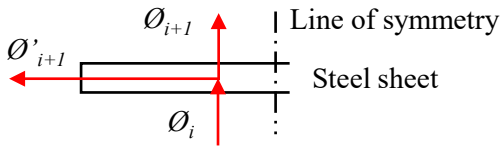

Fig. 4.6 Normal flux and radial flux (distributed around the disc perimeter)

Accordingly, the proposed MCM is constructed and shown in Fig. 4.7. Since fringing flux is neglected in all MR elastomer layers, there is only one category of flux component for MR elastomer layers which is $Ø_i$. In steel layers, the magnetic flux was separated into two

components which are the normal flux ($Ø_i$) and fringing flux ($Ø'_i$). These fringing fluxes leak out at the i^{th} steel layers then travels through the air path which has the reluctance of $R_{air,i}$ and goes back to the laminated structure forming the paralleled air reluctance elements in the circuit. The illustration for the flux leakage paths, i.e., R_{air1} and R_{air2}, are presented in Fig. 4.8. The calculation of $R_{air,i}$ values follows Eq. 4.2. In Eq. 4.2, l used is the length of path which crosses the centre of the cross section of $R_{air,i}$ (presented as red dotted line in Fig. 4.8); and A is using the cylindrical surface area of the steel sheet. Since the fringing fluxes leaked out from steel sheet layers in the radial direction, the radial reluctance of steel sheet (R_{sr}) is also included in the paralleled fringing path. $R_{air,i}$ values are summarised in Appendix B. R_{sz} is the reluctance of steel sheet in the normal direction. Assuming the flux leakage only occurs at the middle point of the axial height of the steel sheet, for $Ø_{PM}$ and $Ø_9$, they only travel for the half of the 1st and 9th steel sheets respectively on the normal direction.

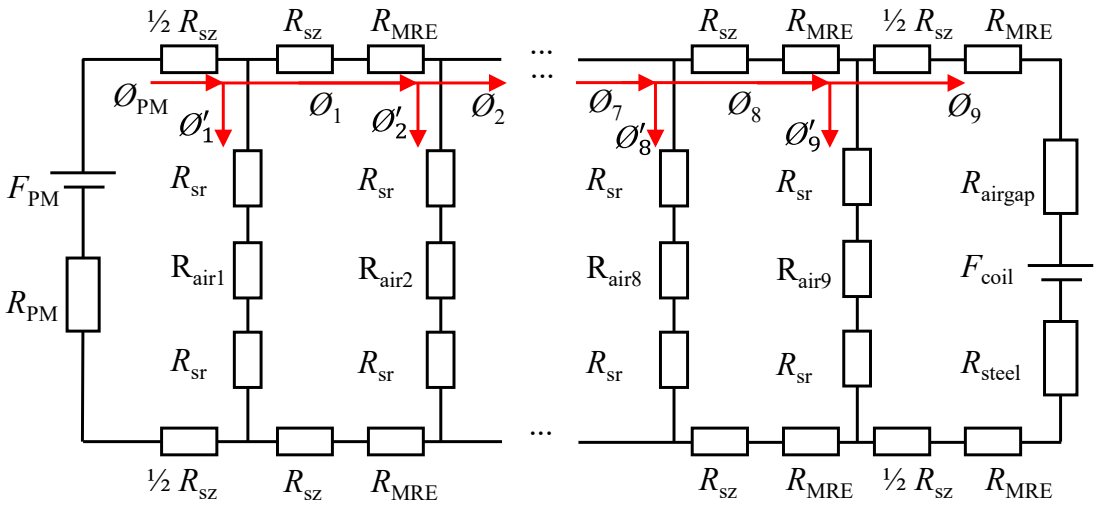

Fig. 4.7 MCM with considering Magnetic flux fringing effect

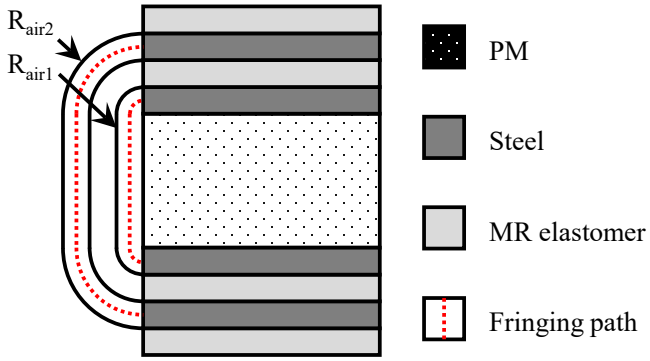

Fig. 4.8 Flux leakage path

Additionally, to include the influence of fringing flux at air gap between the top plate and the yoke, the air gap model presented in Fig. 4.5(b) and Eq. 4.7 was adopted in this MCM to provide a more accurate cross-sectional size for air gap. Following Kirchhoff's law, the mathematical expression of the proposed MCM can be expressed as Eq. 4.9:

$$
\begin{aligned}
F_{\mathrm{PM}} &= \varnothing_{\mathrm{PM}}\left(R_{\mathrm{PM}} + R_{\mathrm{SZ}}\right) + \varnothing_1'\left(2R_{\mathrm{SR}} + R_{\mathrm{air1}}\right) \\
\varnothing_1'\left(2R_{\mathrm{SR}} + R_{\mathrm{air1}}\right) &= \varnothing_2'\left(2R_{\mathrm{SR}} + R_{\mathrm{air2}}\right) + 2\varnothing_1\left(R_{\mathrm{MRE}} + R_{\mathrm{SZ}}\right) \\
\varnothing_i'\left(2R_{\mathrm{SR}} + R_{\mathrm{air}i}\right) &= \varnothing_{i+1}'\left(2R_{\mathrm{SR}} + R_{\mathrm{air}i+1}\right) + 2\varnothing_i\left(R_{\mathrm{MRE}} + R_{\mathrm{SZ}}\right) \\
F_{\mathrm{coil}} &= -\varnothing_9\left(R_{\mathrm{SZ}} + 2R_{\mathrm{MRE}} + R_{airgap} + R_{Steel}\right) + \varnothing_9'\left(2R_{\mathrm{SR}} + R_{\mathrm{air9}}\right)
\end{aligned}
\tag{4.9}
$$

By substituting Eq. 4.2, 4.3 and 4.8 into Eq. 4.9, the amount of flux in each layer can be yielded. To simplify the solving procedure, permeability for steel and MR elastomer is assumed as constant with $\mu_{steel} = 3.93 \times 10^{-3}$ Hm^{-1} and $\mu_{MRE} = 4.73 \times 10^{-6}$ Hm^{-1}. This assumption is valid since the flux densities in all steel components did not reach saturation; as for MR elastomer, the total axial height of MR elastomer sheets is small, i.e., 18 mm, which has insignificant influence on the result accuracy.

However, the flux density cannot be obtained through Gauss' Law directly since the fluxes in the normal and radial direction for each element should all be considered when

calculating flux density. Considering the vector property of magnetic field, Eq. 4.10 should be adopted to obtain the flux density in steel sheet.

$$B = \sqrt[2]{(\emptyset_i/A_n)^2 + (\emptyset_i^{'}/A_r)^2} \tag{4.10}$$

where A_n and A_r are the areas of the top surface and the side surface of the steel sheet.

4.6 Results and Discussion

The computed flux density at each layer using FEA, MCM and MCM considering flux fringing (MCMF) effect is illustrated in Fig. 4.9. The horizontal axis represents the layers of the laminated core. The results from conventional MCM are represented by the flat grey lines since this method cannot capture the variances of magnetic field in laminated core structures. The red bar and black bar represent the results from the improved MCM and FEA. The green line and blue line indicate the errors of the MCM with considering flux fringing effect and the conventional MCM compared with FEA in percentage which are calculated through Eq. 4.11. It should be noted that MCM and error of MCM is plotted on Fig. 4.9(f), due to the conventional MCM cannot provide estimations for the scenario where the same the same MMF as the PM were provided by the coil (when i = 1.357 A). Detailed values of magnetic flux densities and errors are summarised in Appendix C.

$$Error = \frac{ABS(model\ result - FEA\ result)}{FEA\ result} \times 100\% \tag{4.11}$$

(a)

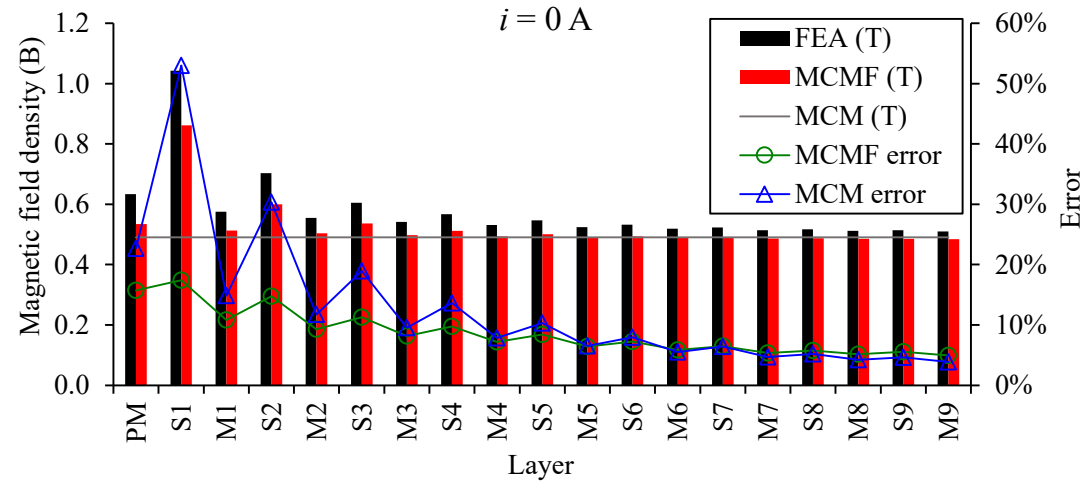
i = 0 A
FEA (T)
MCMF (T)
MCM (T)
MCMF error
MCM error
Magnetic field density (B)
Error
Layer
PM
S1
M1
S2
M2
S3
M3
S4
M4
S5
M5
S6
M6
S7
M7
S8
M8
S9
M9

(b)

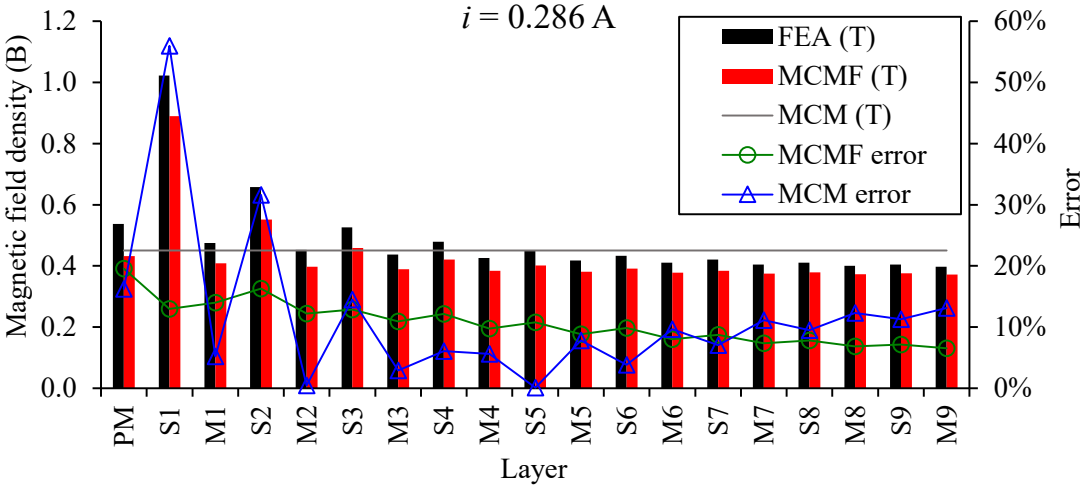
i = 0.286 A
FEA (T)
MCMF (T)
MCM (T)
MCMF error
MCM error
Magnetic field density (B)
Error
Layer
PM
S1
M1
S2
M2
S3
M3
S4
M4
S5
M5
S6
M6
S7
M7
S8
M8
S9
M9

(c)

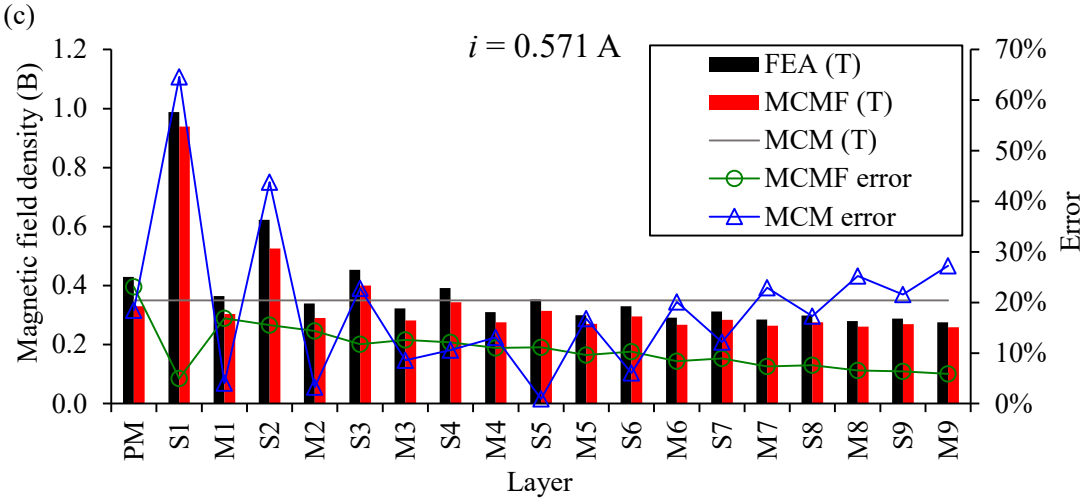
i = 0.571 A
FEA (T)
MCMF (T)
MCM (T)
MCMF error
MCM error
Magnetic field density (B)
Error
Layer
PM
S1
M1
S2
M2
S3
M3
S4
M4
S5
M5
S6
M6
S7
M7
S8
M8
S9
M9

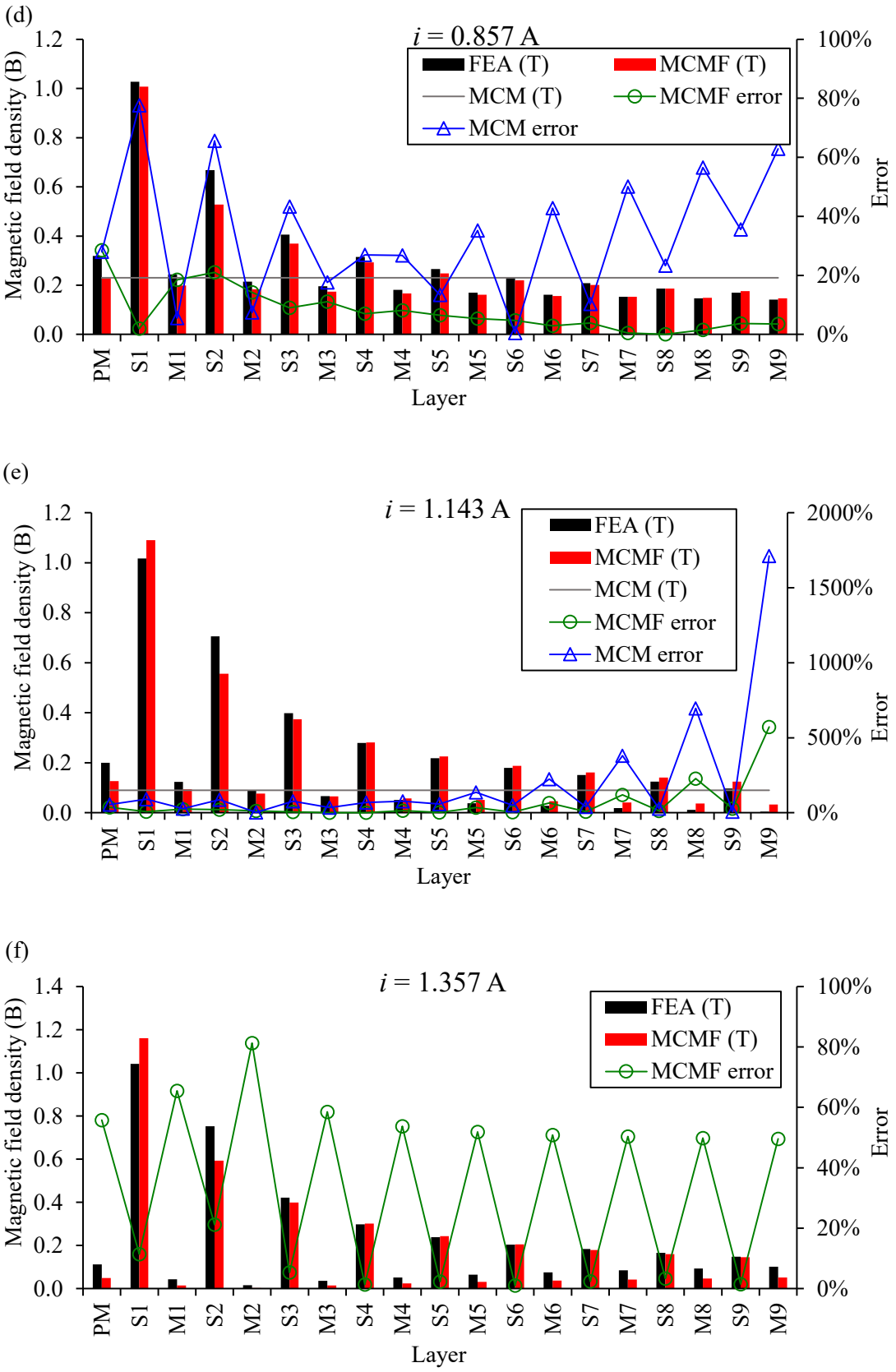

Fig. 4.9 Comparison of FEA, MCM and MCMF (MCM considering fringing effect) under (a) i = 0 A (b) i = 0.286 A (c) i = 0.571 A (d) i = 0.857 A (e) i = 1.143 A (f) i = 1.357 A

As shown in Fig. 4.9(a), for the scenario with no current applied, the overall error for all layers of the laminated core obtained from the proposed MCM and the conventional MCM are 8.71% and 12.73%. The proposed MCM can well portray the variance of magnetic field in different layers and the excessively high flux density values in the first 3 steel layers which are 1.02 T, 0.78 T and 0.64 T respectively, with error within 12%. For MR elastomer layers, the average error of the proposed MCM is 7.02%. The maximum and minimum flux density values in MR elastomer are 0.51 T and 0.48 T for the 1st and the 9th MR elastomer layers well matched with FEA results. The maximum error of flux densities value between the proposed MCM and FEA is only 0.18 T, however, that of the conventional MCM is 0.55 T.

By increasing the applied i to 1.143 A, as illustrated in Fig. 4.9(e), the overall error of the proposed MCM increased to 63.00%. Nevertheless, the overall error of conventional MCM soared to 202.86%. The magnetic flux density in the PM was effectively reduced from 0.53 T to 0.13 T when the applied i increased from 0 to 1.143 A, according to the improved MCM. At this scenario, although the percentage error increased due to the decrease of base number, the maximum error of flux density value between the improved MCM and FEA is only of 0.15 T (0.93 T for the conventional method). It can be concluded that the improved MCM can effectively capture the electromagnetic performance of the device when different i is applied.

With the increase of the applied current to the coil, the flux density in MR elastomer layers decreases, however, flux fringing effect at the laminated core still exhibits eminent flux density values in the steel layers. Additionally, the difference between flux densities of steel and MR elastomer layers became more noticeable when larger current was applied, especially for the layer adjacent to the PM. The computed improved MCM can well reproduce this behaviour. For example, for the first steel layer, it yields 0.86 T, 0.89 T, 0.93 T, 1.01 T and 1.09 T for applied i increased from 0 A to 1.143 A with the overall error less

than 9%. On the contrary, conventional MCM reached almost 70% error for these five scenarios. With further increase of the applied current to 1.357 A, which is the scenario that the conventional MCM failed to compute, the proposed MCM still achieves a high accuracy with overall percentage error of 32% and maximum error of flux density value of 0.16 T.

Compared with results from FEA and the conventional MCM, the effectiveness and superiority of the proposed MCM in depicting the magnetic flux density for the hybrid magnets laminated core and flux fringing effect have been revealed.

4.7 Further discussion

4.7.1 Experimental validation of magnetic field

In the real design of laminated MR elastomer based adaptive devices, currently, the magnetic field in the laminated structure can only be estimated by FEA and MCM; and there is no sensor available to directly measure the field distribution inside of a laminated structure without damaging the structure and changing the flux path. Therefore, developing a rapid and accurate MCM is of great significance addressing the structural complexity of laminated MR elastomer based devices.

A prototype hybrid magnets isolator was manufactured; and magnetic field measurement was performed to prove the veracity of the improved magnetic circuit model. The measurement locations were at the middle of the air gap, as indicated in Fig. 4.10 since these locations are in the magnetic flux path and can accommodate a gauss meter probe. Fig. 4.11 shows the setup of the measurement. The isolator was powered by HDS800PS30 power supply (Helios, Australia) configured in AMP-K6030 rack (Helios, Australia). The gauss meter is TM-197 (Tenmars, Taiwan).

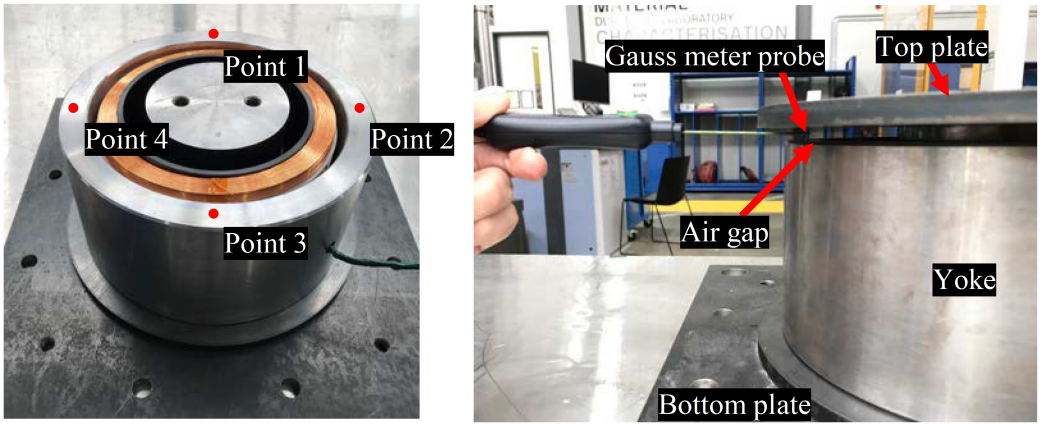

Fig. 4.10 Measurement positions

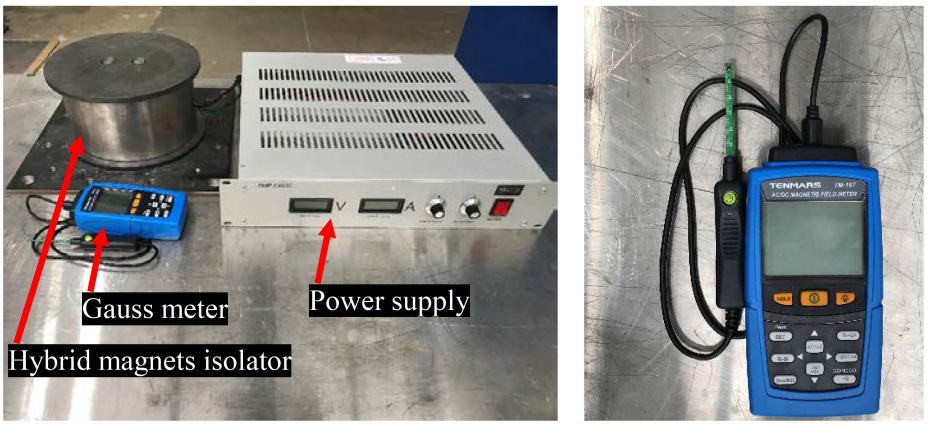

Fig. 4.11 Measurement setup and gaussmeter

The measured magnetic flux density values are summarised in Table 4.4. The average measured flux density of the four locations and the results of flux density in the air gap from the improved MCM and FEA results are plotted in Fig. 4.12. The FEA results were taken at the middle point of the top plate and the yoke. The measured value is lower than both the FEA result and the improved MCM. A similar phenomenon has been reported by Li *et al* [11]. The major reason of having lower experimental values is that the bonding surfaces of the laminated structure were not considered in theoretical methods. The bonding of the MR elastomer and steel layers in the real device is not as perfect as that in theoretical methods. In the 37-layer structure, there are 38 layers of adhesive applied and the glue and air bubbles may not have been sufficiently removed between the MR

elastomer and steel layers in the laminated structure, which may have caused this discrepancy. It is noticeable that the magnetic flex density gaps between the experiment, FEA, and Improved MCM are wide at low currents. As the current increases, the magnetic flux density converges This phenomenon could be resulted by the coupled influences from discrepancies of material permeabilities, nonlinearity of BH curves and air bubbles between the layers. As the MMF by coil increases to the same level as that of PM, the net MMF in the device approaches to zero, therefore, the flux density in the gap approaches to zero and errors becomes small. Although differences exist, the trends of flux density in the air gap are similar among the three groups of results when the applied current is changing. The flux densities decrease with the increase of applied current linearly to the minimum value when 1.143 A applied; then start to increase with the increase of applied current.

Table 4.4 Measured flux density (mT) at the four points in the air gap

	Point 1	Point 2	Point 3	Point 4	Average
0 A	141.6	117.2	136.8	126.0	130.4
0.286 A	89.7	78.9	84.8	95.6	87.3
0.571 A	57.9	50.0	56.4	49.5	53.5
0.857 A	35.3	27.5	21.1	18.2	25.5
1.143 A	33.4	20.1	15.7	15.2	21.1
1.357 A	43.7	41.2	38.8	29.4	38.3

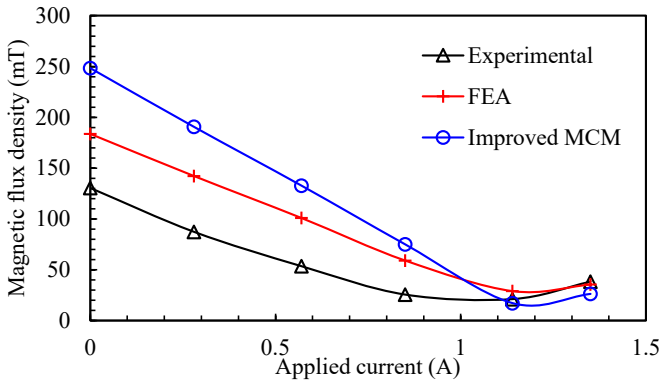

Fig. 4.12 Comparison of experimental, FEA and the improved MCM results

4.7.2 Recommendations on the design of isolator with hybrid magnetic

As for optimization of hybrid magnet systems in the adaptive isolators with laminated MR elastomer core structure, the selection and positioning of the PM and the configuration of coil are critical. For PM, according to suggestions from [132], realising the maximum magnetic energy product is preferred in order to make the volume of PM smallest and to give the highest efficacy of electromagnetic performance of the device. For a neodymium magnet, since its demagnetization curve is a straight line in the second quadrant, the max magnetic energy product can be reached when the magnetic flux density in the magnet is half of its remanence. According to the improved MCM, in the prototype device, the magnetic flux density in the PM is 0.61 T when no current applied to the coil. Since this value is around half of the remanence of an N40 neodymium magnet, e.g., 1.25 T, this device accomplished a most effective and compact configuration. Regarding the positioning of the PM, the design proposed used one layer in the middle of the laminated core structure rather than separating the PM into several thinner layers. This is to protect the PM from irrecoverable demagnetization when the coil is energised and also to avoid cracking of PM due to the large attraction force between the PM and steel during installation. The design of the coil should provide sufficient MMF to offset the magnetic field from the PM.

4.8 Conclusion

In this work, a novel MR elastomer based adaptive isolator featuring stiffness softening effect and an improved MCM has been proposed. Also, suggestions addressing the application of the hybrid magnet system were provided. Considering the magnetic field dependence of this device, theoretical analysis including conventional MCM and FEA have been conducted. FEA results revealed that the proposed device provides a wide range of

controllability of magnetic field, which can be offset to almost 0 T from 0.57 T in MR elastomer layers when 1.357 A is applied to each small coil, therefore offering outstanding adjustability in the mechanical properties. By addressing the flux fringing effects the proposed MCM achieves excellence in capturing the magnetic field distribution localized to each layer in the laminated structure for both non-current applied and large current applied scenarios. The proposed MCM also mitigated the failure of computing the maximum current applied scenario for the conventional MCM.

Chapter 5

Characterisation and Modelling of MR Gel

In this study, the MR gel sample with carbonyl iron particle (CIP) content of 60 wt% was prepared. The dynamic hysteresis responses of the MR gel sample have been characterized using a rheometer under sinusoidal shear excitations with broad ranges of strain amplitude (10% – 100%), excitation frequency (0.1 Hz – 2 Hz) and magnetic field (0 – 0.91 T). The experiments suggested that the dynamic behaviour of MR gel heavily depends on the excitation inputs and magnetic fields. In particular for low level of field (0.27 T), stress overshoot phenomenon occurred at the reverse of the shear flow. A Bouc-Wen model was implemented to fit the characterised stress-strain behaviour of MR gel however failed in predicting the overshoot phenomenon. A simple and accurate phenomenological model with only four parameters has therefore been proposed to capture this unique nonlinearity of MR gel, and the field-induced stress overshoot. For the generalisation purpose, the parameters of the proposed model are identified form the experimental data and used for the training of a support vector (SVM) assisted model. The SVM assisted model was validated with other group of experimental data showed accurate predictions of the hysteretic behaviour and overshoot of the MR gel under all excitation scenarios and the magnetic fields considered.

5.1 Introduction

MR gel, as a new branch of magnetorheological (MR) materials [133-136], holds the potential to be adopted in adjustable devices, due to that it offers extensive adjustability in material properties under the influence of the external magnetic field [137]. The compositions of MR gel are typically polymer gel as the matrix, ferromagnetic filling particles, and additives. Compared with the free-flowing liquid matrix of MR fluid, which is the most reported controllable fluid, the partially entangled polymer gel matrix has a higher viscosity and yield stress, which decides the lower sedimentation behaviour and superior sealing performance of MR gel [14, 82]. Moreover, the properties of the polymer matrix can be simply orchestrated by changing the concentration of copolymer, morphology, and cross-link profile; and, depending on the fabrication composition and fabrication process, MR gel appear as soft gel, and solid-like [28, 138-141]. Therefore, the availability of the controllable materials for adjustable devices can be greatly expanded, and the performance and adjustability of the controllable devices can be more precisely designated and tailored.

Being classified as both MR material and complex fluid, MR gel express strong dependencies on both magnetic fields and excitation inputs, i.e., strain amplitude and strain rate (or excitation frequency) [142]. Furthermore, adaptive devices are normally subjected to reciprocating loadings with large strain amplitudes, which generally lead to highly nonlinear stress-strain hysteresis. Under the application of the external magnetic field, the nonlinearity in the hysteretic behaviour becomes more drastic and complicated since the materials transform from gel-like liquid state, more sticky elastomeric material to solid materials. Essential efforts were made to establish understandings of this novel controllable complex fluid and mainly focused on reporting the innovative recipes for high adjustable material, experimental testing to revealing the rheological behaviour and

material stability [26, 29, 65]. The adjustability of yield stress from about 10 kPa to almost 200 kPa can be achieved by MR gel under the influence of the external magnetic field [143]. From the application perspective, the high storage modulus and adjustability of MR gel can contribute to a more compact device design and higher controllable ranges of the device. No particle sedimentation was observed in MR gel if the solvent content is lower than 25 wt% [29]. These findings suggested the potentials of developments of compact and stable controllable devices for various engineering prospects, including controllable damping devices and torque transmission actuators.

Towards the design of controllable-material-based devices and predicting the performance of the devices, it is an essential step to conduct characterization of the stress-strain hysteresis behaviour of the material. The common approach to obtain the stress-strain relationships for MR materials is performing sinusoidal shear tests using customised shear test rigs [29, 54, 80] or rheometers [55, 67] under different levels of magnetic fields. Commercial rheometers are widely merited for its simple set up and high precision for rheology studies and material characterisations. The raw waveform data recording function for large amplitude oscillatory shear test and the electromagnet accessories enable the stress-strain hysteresis characterisation for MR materials. However, the hysteresis behaviour of MR gel has not been characterized in the previous research.

Substantial efforts have been made on the modelling of other controllable materials to predict the stress-strain hysteresis loop under different excitation inputs and external magnetic field [144, 145]. These models were developed and can be adopted in the control algorithms to achieve active or semi-active control devices and systems for both engineering practices and numerical simulations. Two general types of models can be classified from the past investigations are physical model and phenomenological model. The physical models are constructed based on the interpretation of the microstructure of the material and generally have over-simplified assumptions and require a sophisticated

computation process [146-148]. On the other hand, phenomenological models are based on the empirical relations between the excitation inputs and hysteresis performances. They provide a versatile and straightforward model formulation process and consider the dependencies of frequency, strain amplitude, and external magnetic field. Commonly, the accuracy and simplicities of the model, i.e., less parameter and avoiding piecewise function and differential equations, significantly contribute to the effectiveness and response time of the controller [149].

Therefore, phenomenological models are extensively adopted in depicting the hysteresis responses of controllable materials and devices. Li et al. [55] proposed a four-parameter viscoelastic model for the prediction of dynamic hysteresis responses of MR elastomer. Dargahi et al. [80] established a Prandtl-Ishlinskii model with the sound performance of describing the dependencies of the field and excitation inputs for MR elastomer. Yu et al. [101] constructed a Bouc-Wen-operator-based hysteresis model, which can capture the strain stiffening of the MR elastomer base isolator under the influence of the applied external magnetic field. For controllable-fluid-based applications, Spencer et al. [89] proposed a simple Bouc-Wen model for the semiactive control of MR fluid dampers for engineering structures. In light of this successful implementation of Bouc-Wen model in MR fluid dampers, this model has been modified to further extend its applicability for large scale damper [150], self-centring bracing [151] and MR elastomer base isolators [12]. Although numerous variations of phenomenological models have been formulated to capture the stress-strain hysteresis for magnetorheological materials, their applications to MR gel have never been reported.

5.2 Experimental

5.2.1 Material preparation

The MR gel sample in this research is fabricated with 60 wt% of CIP (spherical, 3.5 μ diameter, provided by Beijing Xing Rong Yuan Technology Co., Ltd., China) and polyurethane (4608 oil-based polyurethane, provided by Jining Tainuo Chemical Co., Ltd., China). Polyurethane is normally synthesized by toluene diisocyanate and polypropylene glycol; and its viscosity can be easily tailored by the ratio between the diisocyanate and glycol. Higher diisocyanate concentration gives higher viscosity of the polyurethane [29, 65]. The polyurethane appears as soft gel state and has an amber hue before mixing. To prepare the MR gel, firstly, the polyurethane sample was stirred at 60 °C for 30 minutes with the mixer set at 500 rpm. Then the polyurethane was cooled down to 30 °C. The weighted CIP was added to the polyurethane and mixed for 1 hour at 500 rpm. Then, the mixture was treated with an ultrasonic vibrator for 15 minutes to get a more uniform distribution of CIP and remove the air bubble in the mixture. To further eliminate the air bubble and moisture, the mixture was stored in the vacuum drying machine for 2 hours and then placed 2 days at room temperature. Finally, the MR gel with CIP of 60 wt% was prepared. Fig. 5.1(a) is the photo of the prepared MR gel sample settled in the beaker. In Fig. 5.1(b), as beaker is tilted, the MR gel surface bulges towards the tilting direction. Then the MR gel surface gradually levels to the horizontal plane under the influence of gravity after approx. 15 seconds, as presented in Fig. 5.1(c). This behaviour suggests that MR gel has the higher stability and viscosity, compared with free flowing MR fluid; however, yet reached the elastomeric state as MR elastomer.

Fig. 5.1 Photos of the MR gel sample (a) settled in the beaker (b) the beginning of tilting (c) approx. 15 seconds after tilting

5.2.2 Experimental setup and measurements

The dynamic hysteresis characterization of the MR gel sample was performed on the MCR 302 rheometer (Anton Paar Co., Austria) using PP20 model parallel plate measurement system (Anton Paar Co., Austria), as presented in Fig. 5.2(a). The rheometer is equipped with the raw data module which enables the recording of raw stress and strain waveforms. The parallel plate measurement system has a uniform gap height between the PP20 measuring tool and the base plate, thus yields a uniform magnetic field distribution in the gap. In all experiments, the gap was set at 1 mm. Since the radius of the PP20 measuring tool is 10 mm, the volume of MR gel sample controlled for each test is $\pi \times 1\text{^}2 \times 0.1 = 0.314$ ml. The MR gel sample is applied at the centre of the base plate in the gap. The magnetic field in the gap was controlled by the coil sets embedded under the rheometer bottom plate. The maximum current applied to the coils is 5A by the power supply (PS-MDR/5A, Anton Paar Co., Austria). To find the correlation between the fiend density and the applied current and to assess the homogeneity of the magnetic field, the magnetic fields at three locations beneath the base plate were measured by a teslameter (FH54, Magnetic Physics Inc., Germany) with a hall probe (HS-TGB5, Magnetic Physics Inc., Germany) inserted under the base plate at the centre, as illustrated in Fig. 5.2(b) and (c). The three locations

are the projections of the centre, middle of the radius (5 mm from the centre) and the edge (10 mm from the centre) of the PP20 measurement plate. During the measurement, 0 A to 5 A (1 A step) currents were applied to the coil; and MR gel sample was applied to the centre of the base plate with the gap height set at 1 mm. Since the hall probe cannot be accommodated inside of the gap when sample was placed, the probe inserted in the slot beneath the base plate. The measured correlation between the field density and the applied current is presented in Table 5.1. Small discrepancies in the field densities at the three locations were observed, around 5%. The average of the field density at the three locations was used in the following sections to indicate the levels of magnetic fields. When the current is increased from 0 to 5 A, the magnetic field density increases almost linearly from 0 T to 0.91 T.

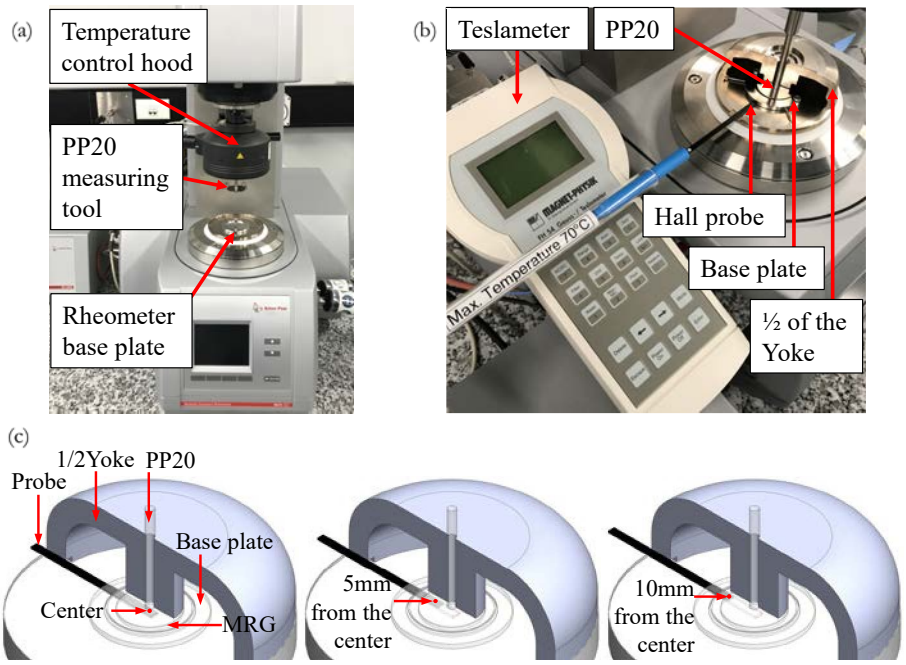

Fig. 5.2 Set up of (a) characterization tests (b) measurement of magnetic field (c) locations of field measurement

Table 5.1 Correlation between the magnetic field density and applied current

Current (A)	Centre (T)	5mm from centre (T)	10mm from centre (T)	Average (T)
0	0	0	0	0
1	0.26	0.26	0.28	0.27
2	0.47	0.46	0.49	0.47
3	0.64	0.62	0.66	0.64
4	0.78	0.77	0.80	0.79
5	0.90	0.88	0.93	0.91

During the measurement of magnetic field and characterisation tests, a set of magnetic chambers (MDR H-PTD 200, Anton Paar Co., Austria) were placed on the rheometer base plate to form an enclosed magnetic flux path. The temperature was controlled at 25 ± 0.2 ˚C for all measurements by a temperature module (C-PTD 200, Anton Paar Co., Austria) connected to the base plate and a temperature control hood (H-PTD 200 hood, Anton Paar Co., Austria) applied over the magnetic chamber. It should be noted that the temperature fluctuations vary with the applied current. By applying 0, 1, and 2 A currents for 300 seconds, the temperature increment can be well limited within 0.03 ˚C. At 3, 4, and 5 A, the temperature increases for 0.05, 0.12 and 0.19 ˚C over 300 seconds, respectively. From the past research [152, 153], such level of temperature increment only decreases the dynamic yield stress of polymer-based MR materials by less than 0.15%. In this research, the testing time is controlled under 300 seconds which allows 30 cycles of 0.1 Hz test.

The characterisation tests of the hysteresis responses of the MR gel were conducted under strain-controlled sinusoidal excitations with various frequencies, strain amplitudes and magnetic fields considered. To date, such characterisation has yet to be reported for MR gel. For controllable fluid like MR fluid, its hysteresis behaviour has normally been characterised under excitation frequency from 0.5 Hz to 1.5 Hz [83]. In this research, a wider range of frequency was considered for MR gel, which were 0.1, 0.5, 1 and 2 Hz. The

strain amplitudes for the measurements were set from 10% to 100%. Measurements of each excitation input were carried out with six levels magnetic field applied (currents applied to the coil set: 0, 1, 2, 3, 4, 5 A), since the storage modulus reaches the maximum when the magnetic field density increased to about 0.8 T [29]. All tests were conducted under stain control. The temperature was set at 25 °C for all tests. 513 data points were samples for each measured hysteresis loop.

5.2.3 MR gel dynamic characteristics

The recorded stress-strain hysteresis of the MR gel sample indicated strong and complicated dependencies on excitation frequency, strain amplitude, and the external magnetic field. Fig. 5.3 shows the stress-strain relationships of the MR gel sample under the influences of the frequency, strain amplitude, and magnetic field. The enclosed area of the hysteresis loop represented the dissipated energy under the sinusoidal shear motion. The stiffness can be represented by the slope of the major axis of the hysteresis curve. Primarily, the increases of excitation frequency, strain amplitude and magnetic field contributes to both the energy dissipation and stiffness of MR gel. The presence and intensifying of the external field form and strengthen the CIP chain structures in the gel matrix and result in the drastic growth of the elastic component in the MR gel. The dynamic response of MR gel is similar to pure viscous material without the magnetic field; however, under the magnetic fields, it become to be ellipse shaped as the viscoelastic materials. This unique transition from the magnetic field off and on states of MR gel differs from other MR materials like MR fluid and MR elastomer. MR fluid and MR elastomer exhibit box-shaped and ellipse-shaped hysteresis loops, respectively [80, 83]; and the presence of external field does not change the general outlines of their hysteresis loops. An apparent stress overshoot effect was observed and will be discussed in the following section.

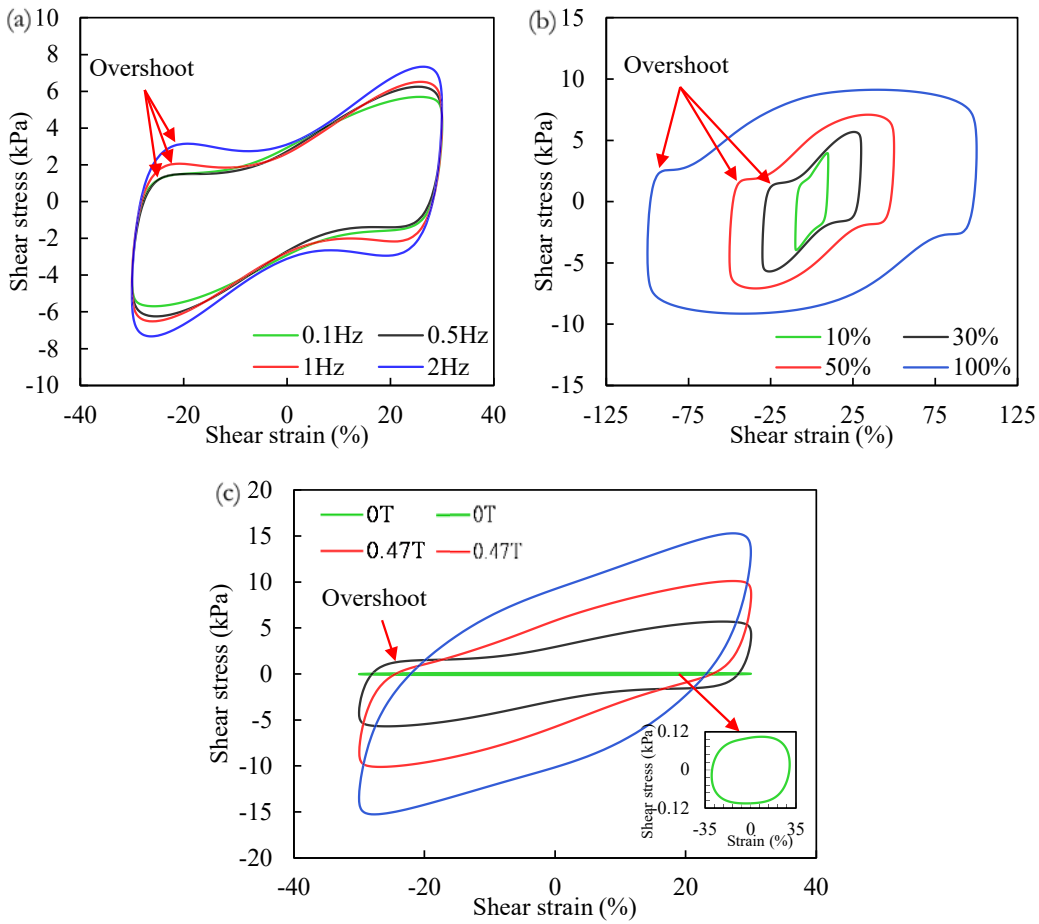

Fig. 5.3 Hysteretic responses of MR gel (a) influence of frequency (30% strain; 0.27 T) (b) influence of strain amplitude (0.1 Hz; 0.27 T) (c) influence of magnetic field (0.1 Hz; 30% strain)

Fig. 5.3(a) compares the influence of excitation frequency on the stress-strain responses of MR gel when strain amplitude is fixed at 30% and 1 A current applied to the coil. The growing frequency effectively increased the dissipated energy and the stiffness of the MR gel. This phenomenon is in line with the findings from Yang et al. [82] and Xu et al. [29]. Fig. 5.3(b) represents the hysteresis loop with different strain amplitudes applied under the same level of excitation frequency (0.1 Hz) and magnetic field (0.27 T). Although the increase of strain amplitude increases the measured maximum shear stress, the reducing slope indicates a decreasing trend of storage modulus with the rise of strain amplitude.

Similar results were reported in [65, 154]. Fig. 5.3(c) depicts the influence of the applied magnetic field when the excitation inputs are fixed at 0.1 Hz and 30% strain. The plot for the 0 T scenario, located at the bottom right corner of Fig. 5.3(c), has a nearly circular shape, and the gradual slope of the hysteresis loop suggested a minor effect of elasticity. Due to the absence of the magnetic field, CIP contents are randomly distributed in the polyurethane matrix rather than forming columnar structures [25, 26]. The application of the external magnetic field results in a nonlinear viscoelastic-material-like behaviour. Further intensifying the magnetic field (up to 0.91 T) outputs an increasing trend of both stiffness and energy loss of MR gel under the sinusoidal waveform.

Furthermore, significant stress overshooting phenomenon can be observed at the shear rate reversing points of a strain cycle, only under the application of magnetic field, especially for the lower-level magnetic fields (0.27 T). The occurrence of overshooting is because of that the reversed strain deformation is accumulated slower than the shear stress in the shear flow is unloaded [155]. Numerous similar stress-strain responses were reported in the rheological studies of a wide range of soft matter and complex flow [156-159] and suggested that the occurrence of overshooting is strongly dependent on the strain rate of the shear flow [160]. As suggested by [161], wall slippage and surface roughness of the measurement tool may also lead to stress overshoot phenomenon; and, the overshoot induced by wall slip normally appears as abrupt drop and fluctuation of the shear stress. The smooth and contentious hysteresis loop of MR gel means that the measurement is not significantly affected by wall slip.

With the involvement of the magnetic field, the overshoot of MGR is not simply dependent on excitations and shows more unique dependency on the applied current. As shown in Fig. 5.3(a) and (b), when 0.27 T applied, this phenomenon showed up in all excitation frequencies and strain amplitudes. Form Fig. 5.3(c), although under the same excitation frequency and strain deformation, as the magnetic field further increased to 0.47

T and 0.91 T, the overshoot became less visible and then disappeared. It could be explained that the intensified magnetic field strengthens the yield stress of the CIP chain structures in MR gel; the reverse of strain rate occurred before the shear stress reaches the yield level of MR gel under a large magnetic field. This phenomenon has not been found in the dynamic characterization studies of other controllable materials.

However, stress overshoot frequently appears in practical engineering applications and is always challenging and critical for researchers to capture in the control system, since the ignorance of overshoot will cause false feedback and failure of control [150, 162]. Thus, modelling practices for MR gel were performed in the following section.

5.3 Modelling of the hysteresis behaviour

5.3.1 Hysteresis modelling using Bouc-Wen model

As the hysteresis behaviour for MR gel has not been revealed in the past, modelling of this unique response is lack of practice and in urgent demand. Here, we use Bouc-Wen model to fit the stress-strain behaviour of MR gel since it is the universally accepted model for portraying nonlinear behaviour of materials and structures, and has been successfully used in reproducing the nonlinear behaviour of MR fluid/MR elastomer materials and devices [12, 101]. This could be beneficial in modelling for MR gel since MR gel exhibits both viscous and viscoelastic behaviours depending on the presence of the external magnetic fields. An existing Bouc-Wen model developed by Yang *et al.* for an MR elastomer isolator was implemented to model the MR gel dynamic behaviour, with the formulation presented as follow [12]:

$$\begin{aligned} \tau_{\mathrm{est}} &= \alpha k_0 \gamma + (1-\alpha) k_0 z + c_0 \dot{\gamma} \\ \dot{z} &= A\dot{\gamma} - \beta|\dot{\gamma}||z|^{n-1} z - \delta\dot{\gamma}|z|^n \end{aligned} \tag{5.1}$$

where τ_{est}, γ and $\dot{\gamma}$ are the predicted shear stress, shear strain and strain rate respectively; a, β, δ, A, and n are the non-dimensional parameters which govern the shape and size of the predicted hysteresis loops; k and c are the parameters for the elastic spring and dashpot element, respectively; z is the imaginary variable to represent the time-series function of the shear strain. Generic algorithm was applied to find the combinations of model parameters that yields the minimal value root mean square error (RMSE) between the experimental data and τ_{est}. RMSE can be expressed by Eq. 5.2 as follow:

$$RMSE = \sqrt{\frac{1}{N}\sum_{j=1}^{N}[\tau(j) - \tau_{\mathrm{est}}(j)]^2} \tag{5.2}$$

Where N is the number of samples in one hysteresis loop, and $\tau(j)$ and $\tau_{est}(j)$ stand the j^{th} measured shear stress and the estimated shear stress from the Bocu-Wen model, respectively. The predictions from the Bouc-Wen model are compared with the experimental results in Fig. 5.4. Fig. 5.4(a), (b) and (c) presents the fitting of the model under the scenarios of different excitation frequencies, strain amplitudes and applied currents, respectively.

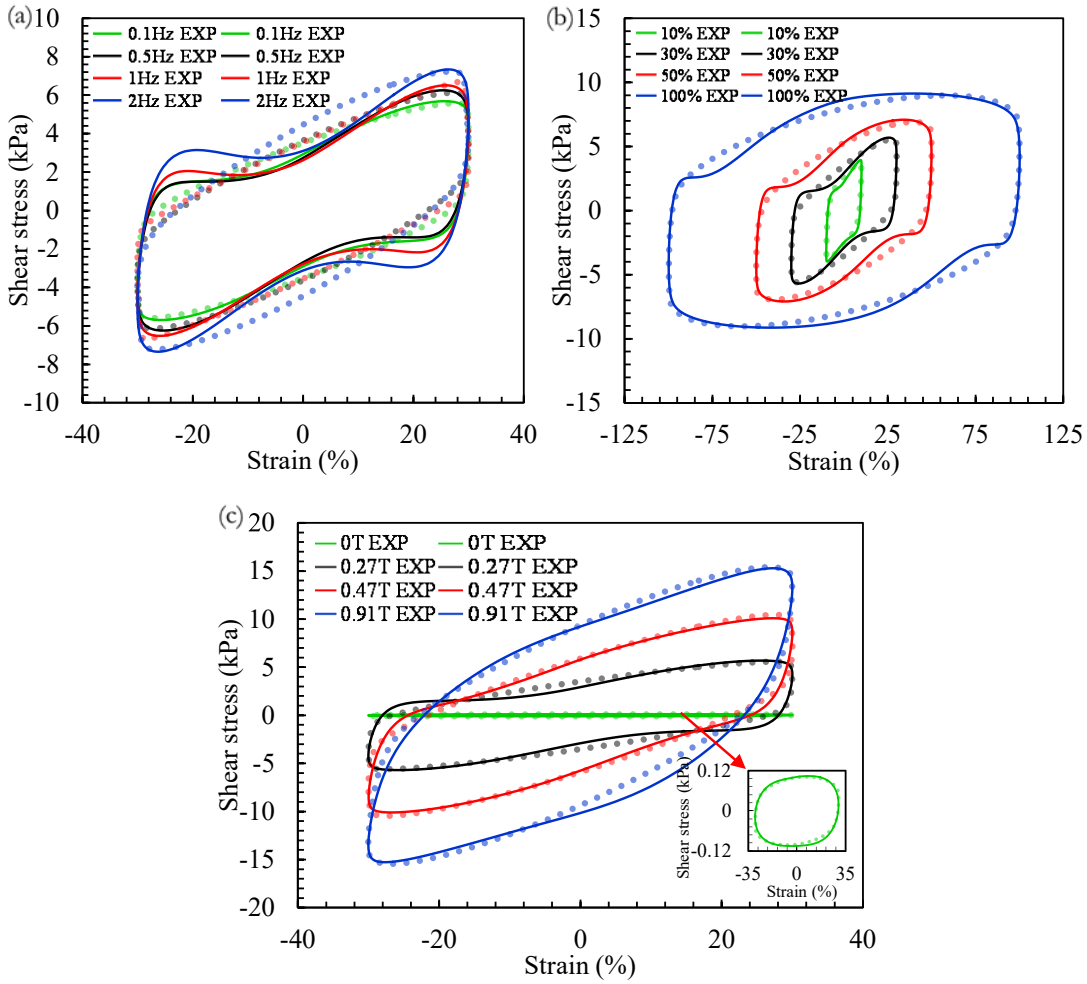

Fig. 5.4 Comparisons between experimental data and simulation result from Bouc-Wen model for: (a) different frequencies, 0.27 T, 30% strain (b) different strain amplitude, 0.27 T, 0.1 Hz (c) different magnetic field, 30%, 0.1 Hz

Overall, the Bouc-Wen model is able to predict the general outlines of the MR gel hysteresis loops and the transitions before the revering points of the shear motions; but fails to portrait the overshoot phenomenon after the revise. In Fig. 5.4(a) and (b), under 0.27 T scenarios where MR gel exhibits significant stress overshot, the Bouc-Wen model ignored all details for the stress overshoot and only estimated shear stress as gradual increasing lines. Although, in Fig. 5.4(c), the Bouc-Wen model showed acceptable performances for the viscous-like response under 0 T and the viscoelastic behaviours under 0.47 T and 0.91 T as expected, the ignorance of the overshoot behaviour will still

lead to the false feedback for the controller and failure of control in the application stage. The following sections propose a simple and accurate 4-parameter phenomenological model which can characterize the unique overshoot behaviours of MR gel with considering the dependency on the magnetic field to mitigate the lack of practice of MR gel hysteresis modelling.

5.3.2 Formulation of a 4-parameter overshoot model

The experimental results in Fig. 5.3 indicated the hysteresis responses of MR gel without the application of the magnetic field form an almost circle and barely has the sign of overshoot and elastic behaviour. As the field density increases to 0.27 T, two major features of viscoelasticity and overshoot can be identified. Therefore, when stress overshoot occurred, the shear stress can be decomposed into two parts, which are a viscoelastic part and the overshoot part. The viscoelasticity part of MR gel is modelled through using the Kelvin-Voigt model, which parallels a linear spring element (k) and a viscous dashpot (c) [87]. The Kelvin-Voigt model can be formulated as:

$$\tau_{\text{viscoelastic}} = k\gamma + c\dot{\gamma} \tag{5.3}$$

where γ is the shear strain and $\dot{\gamma}$ is the shear rate. The overshoot stress (τ_o) component, considering its shape and occurring location, is represented by a two-parameter overshoot element formulated as follow:

$$\tau_o = \begin{cases} (1+\gamma_{\text{nor}})ba^{-a(1+\gamma_{\text{nor}})}, \dot{\gamma} \geq 0 \\ (1-\gamma_{\text{nor}})ba^{-a(1-\gamma_{\text{nor}})}, \dot{\gamma} < 0 \end{cases} \tag{5.4}$$

where b is the governing the magnitude of the overshoot stress component, a is controlling the shape variation and location of the overshoot element, γ_{nor} is the normalized strain (γ). To illustrate the effect of parameter a on the shape and the location of the overshoot stress, the normalized τ_o values are plotted in Fig. 5.5. When a value is set at 3, the clear overshoot peak can be observed. With the further increment of a, the peaks start to merge

to the shear flow reverse points and become resemblant to the shape and location of the overshoot observed from MR gel characterization under the lower magnetic field scenarios. When a is lower than 3, the shape of the overshoot element shows a close match with the nonlinear viscoelastic behaviour of the MR gel under the higher magnetic fields (0.47 T and 0.91 T). As for 0 T case, where the hysteresis loop presents an almost perfect circular shape, the overshoot element is deactivated (parameter b set as 0). Subsequently, by paralleling the overshoot element with the viscoelasticity model, the proposed model can be formulated as follow:

$$\tau_{\text{est}} = \begin{cases} k\gamma + c\dot{\gamma}, & Applied\ current = 0 \\ k\gamma + c\dot{\gamma} + \tau_o, & Applied\ current \neq 0 \end{cases} \tag{5.5}$$

where τ_{est} is the estimated shear stress from the proposed model. Fig. 5.6 is the structure of the proposed model. With the combination of the overshoot element and the Kelvin-Voigt model, the estimated shear stress plotted in Fig. 5.6 becomes identical to the characterized dynamic behaviour the of MR gel with stress overshoot phenomenon.

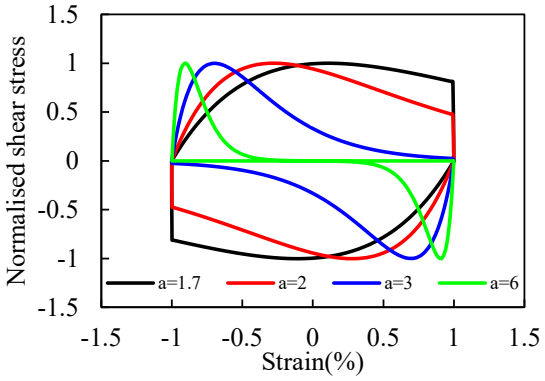

Fig. 5.5 Shape variation of the proposed overshoot element

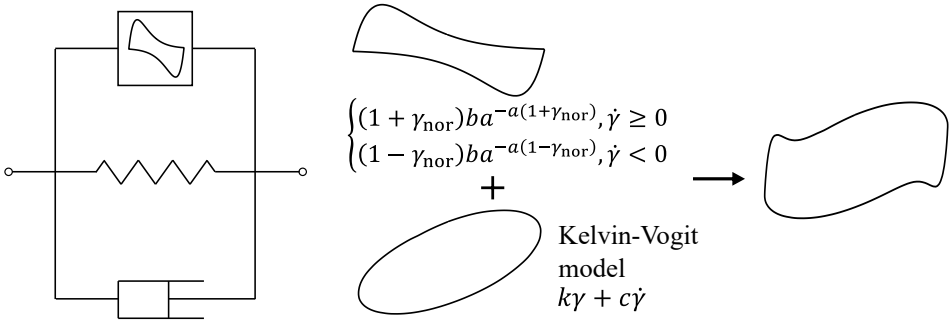

Fig. 5.6 The proposed overshoot phenomenological model

5.3.3 Parameter identification and analysis

Considering the proposed model contains only four parameters, i.e., k, c, a, and b, and has no differential equations, the four parameters can be identified using the least square optimisation method to yield the minimal RMSE (Eq. 5.2) between the experimental results (τ) and the estimated shear stress (τ_{est}) by the 4-parameter overshoot model. For the 0 T scenarios, a values are not considered, and parameter b was set to 0 since the overshoot element is only active while the magnetic field is applied. Fig. 5.7 shows the simulation results from the proposed model for scenarios reported in Fig. 5.3. In Fig. 5.7, the solid and dotted lines represent the experimental data and estimated data by the 4-parameter stress overshoot model, correspondingly. The proposed model accurately captures the hysteresis responses of MR gel for all excitation inputs and magnetic fields considered. At the scenarios and locations where the stress overshoot occurred, the model also showed ideal prediction. The full list of simulation results and experimental data are prepared in Appendix D.

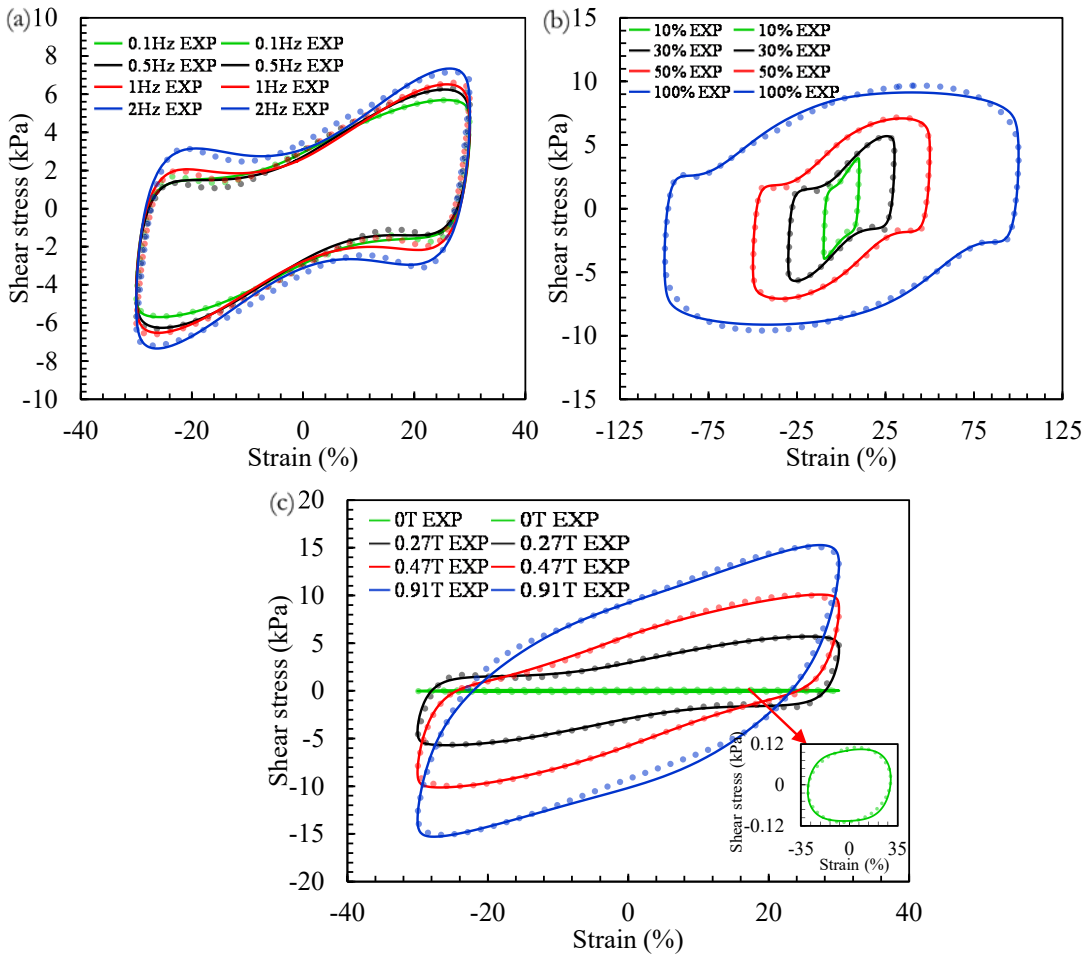

Fig. 5.7 Experimental data and simulation result by the 4-parameter overshoot model under: (a) different frequencies, 0.27 T, 30% strain; (b) different strain amplitude, 0.27 T, 0.1 Hz; (c) different magnetic field, 30%, 0.1 Hz.

The identification results of the four parameters are summarised in Table 5.2 (B represents magnetic field density). To further illustrate the influence of excitation inputs and the magnetic field on the model parameters, the 3D plots are prepared in Fig. 5.8 via Thin Plate Spline algorithm [163]. The clear relationships between the parameter and the variations of the magnetic field and excitation strain amplitude can be observed. In Fig. 5.8 (a), the vertical axis represents the magnitude of parameter *a*, which has a clear decreasing trend with the increase of the external magnetic field and with the decrease strain amplitude. At a larger stain amplitude and a lower magnetic field level, *a* value is

larger. By comparing *a* values under different excitation frequencies, it can be concluded that *a* decrease with the increase of the frequency. Similarly, in Fig. 5.8 (b), parameter *b* is decreased by the intensifying of flux density and the increase of strain amplitude; however, it increases with the increase of the excitation frequency. Corresponding to Fig. 5.5, the larger *a* value gives a more marginalized location from the centre of the horizontal axis of the peak of overshoot stress.

Moreover, larger *b* value yields a larger stress overshoot magnitude. These trends match closely with the findings from the experiments, suggesting that the lower field density and larger strain amplitude result in a sharper and more significant stress overshoot. For the parameters of the elastic spring (k) and the dashpot element (c), which are summarised in Fig. 5.8 (c) and (d), respectively, they undergo increasing trends as the magnetic flux is increased, and the strain amplitude is decreased. The increasing of excitation frequency slightly increases the k values; however, it reduces the c values. These trends agree with the physical interpretations of the parameters, i.e., the external magnetic field contributes to both the damping and stiffness of the MR gel; however, the strain amplitude has the opposite effect on the stiffness and damping.

Table 5.2 Model parameters *a*, *b*, *k*, and *c* under: (a) 0.1 Hz; (a) 0.5 Hz; (a) 1 Hz; (a) 2 Hz.

(a)

	Amplitude=10%				Amplitude=30%			
B (T)	a	b	k	c	a	b	k	a
0	N/A	0	1.53E-03	8.52E-03	N/A	0	8.70E-04	6.09E-03
0.27	3.57	35.10	3.01E-01	2.71E-01	4.67	70.69	1.68E-01	1.78E-01
0.47	3.44	32.80	5.96E-01	3.62E-01	4.45	64.54	2.92E-01	3.13E-01
0.91	2.63	24.41	8.15E-01	5.12E-01	2.86	51.33	3.28E-01	3.74E-01
	Amplitude=50%				Amplitude=100%			
B (T)	a	b	k	c	a	b	k	a
0	N/A	0	6.75E-04	5.57E-03	N/A	0	5.07E-04	5.03E-03
0.27	6.04	95.54	1.06E-01	1.75E-01	7.27	111.61	5.06E-02	1.42E-01
0.47	4.86	83.25	1.90E-01	2.99E-01	6.00	90.00	8.49E-02	2.30E-01
0.91	2.91	55.70	2.21E-01	3.15E-01	3.02	62.83	1.20E-01	2.36E-01

(b)

	Amplitude=10%				Amplitude=30%			
B (T)	a	b	k	c	a	b	k	a
0	N/A	0	1.89E-03	2.49E-03	N/A	0	1.17E-03	1.86E-03
0.27	3.79	44.38	3.16E-01	6.11E-02	4.46	78.85	1.87E-01	3.31E-02
0.47	3.43	43.56	6.52E-01	9.45E-02	4.27	75.59	3.32E-01	6.83E-02
0.91	3.30	39.52	8.27E-01	1.27E-01	3.73	46.94	3.57E-01	9.64E-02
	Amplitude=50%				Amplitude=100%			
B (T)	a	b	k	c	a	b	k	a
0	N/A	0	7.82E-04	1.72E-03	N/A	0	7.58E-04	1.60E-03
0.27	5.07	98.20	1.29E-01	3.59E-02	5.87	115.77	6.31E-02	3.09E-02
0.47	4.82	81.61	2.16E-01	6.93E-02	5.30	94.36	1.09E-01	5.66E-02
0.91	3.77	62.25	2.29E-01	8.50E-02	4.05	68.08	1.19E-01	6.05E-02

(c)

	Amplitude=10%				Amplitude=30%			
B (T)	a	b	k	c	a	b	k	a
0	N/A	0	2.25E-03	1.14E-03	N/A	0	1.89E-03	9.66E-04
0.27	3.05	20.90	3.29E-01	2.73E-02	4.24	83.06	1.87E-01	1.66E-02
0.47	3.00	19.48	6.79E-01	5.69E-02	4.07	80.16	3.38E-01	3.50E-02
0.91	2.99	17.44	8.91E-01	7.88E-02	3.81	60.68	3.60E-01	4.84E-02
	Amplitude=50%				Amplitude=100%			
B (T)	a	b	k	c	a	b	k	a
0	N/A	0	8.64E-04	9.12E-04	N/A	0	8.42E-04	8.84E-04
0.27	5.26	126.28	1.30E-01	1.78E-02	5.88	145.74	6.64E-02	1.60E-02
0.47	5.17	102.71	2.30E-01	3.46E-02	5.48	120.38	1.12E-01	2.97E-02
0.91	3.72	74.50	2.35E-01	4.14E-02	4.31	84.36	1.22E-01	3.02E-02

(d)

	Amplitude=10%				Amplitude=30%			
B (T)	a	b	k	c	a	b	k	a
0	N/A	0	7.81E-03	2.16E-03	N/A	0	4.92E-03	1.65E-03
0.27	3.44	31.62	3.52E-01	1.78E-02	4.16	90.58	2.13E-01	9.68E-03
0.47	3.31	31.38	6.91E-01	3.45E-02	4.16	91.27	3.69E-01	1.95E-02
0.91	3.06	30.13	9.34E-01	4.03E-02	3.94	84.84	4.32E-01	2.47E-02
	Amplitude=50%				Amplitude=100%			
B (T)	a	b	k	c	a	b	k	a
0	N/A	0	4.25E-03	1.52E-03	N/A	0	3.77E-03	1.39E-03
0.27	4.47	149.98	1.76E-01	9.63E-03	5.23	166.31	8.59E-02	9.87E-03
0.47	4.39	135.18	2.80E-01	1.89E-02	5.14	145.85	1.38E-01	1.74E-02
0.91	4.11	115.96	3.00E-01	2.37E-02	4.16	130.97	1.53E-01	1.89E-02

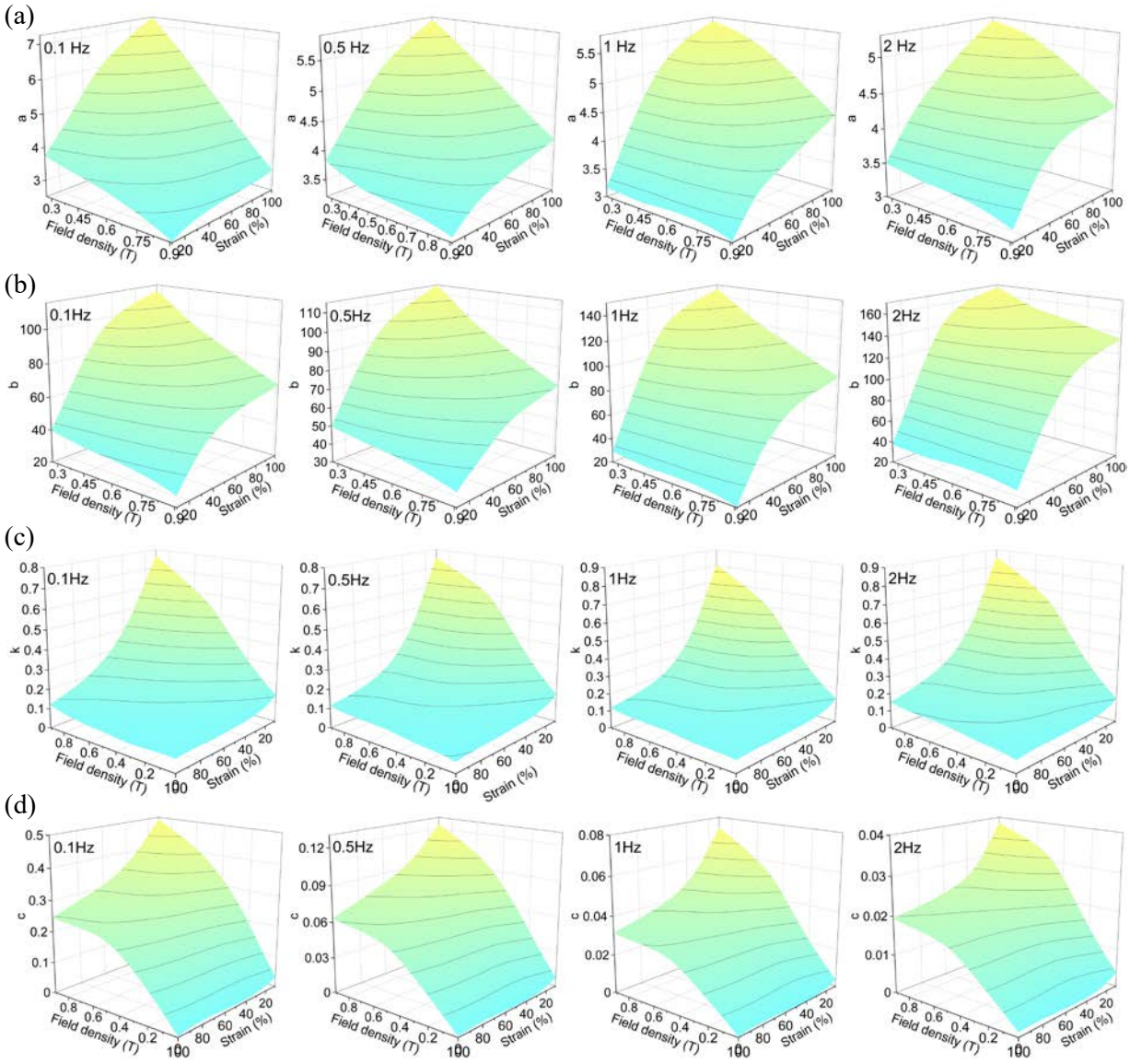

Fig. 5.8 Model parameter identification results (a) parameter *a*; (b) parameter *b*; (c) parameter *k*; (d) parameter *c*.

To quantitively evaluate the accuracy of the proposed model, mean absolute percentage error (MAPE) was calculated for all cases following:

$$MAPE = \frac{1}{N}\sum_{j=1}^{N} ABS[\frac{\tau(j) - \tau_{\text{est}}(j)}{\tau(j)}] \times 100\% \tag{5.6}$$

The overall MAPE value of 12.023% suggests that the proposed model can accurately predict the dynamic hysteresis behaviour of MR gel under a broad band of excitation strain amplitude, fervency, and different levels of magnetic field.

5.3.4 Support vector machine (SVM) assisted model

In the practical use of phenomenological models for the controllable materials and devices, the controlling systems are expected to have adaptive performance under fluctuating excitations and magnetic fields. Since the model parameters are normally identified from experimental characterizations with the test conditions like frequency, amplitude, and magnetic field, held at constant levels, models should be generalised prior to the application in the controlling system. In the past research, model parameters are generally generalized by using the average parameter values under the same magnetic field level and finding the equational expressions between the averaged parameter values and the magnetic field to reduce the complexity of generalization process. This approximation is valid for the scenarios where the material or device performance is majorly dependent on the magnetic field.

However, the characterized MR gel dynamic behaviour and the identified model parameters are heavily reliant on both the magnetic field and the excitation inputs. The simplification by averaging parameters does not apply to the MR gels. Moreover, establishing the equational expressions for the parameter values with three variables, i.e., frequency, strain amplitude, and applied magnetic field, is challenging to achieve ideal results.

Support vector machines (SVMs), as supervised learning models, have been successfully implemented in material science and engineering for accurate prediction, classification, and regression analysis [164-167], and can tackle the multi-variable fitting problems in the model generalization process. In this research, an SVM assisted model is formulated as presented in Fig. 5.9; and consists of two parts: a trained SVM model and the proposed overshoot phenomenological model. With frequency (f), strain amplitude (A) and magnetic field density (B) as inputs, the trained SVM predicts the model parameters, i.e., a, b, k, and

c. Subsequently, the proposed phenomenological model uses the parameters predicted by the trained SVM models to produce the estimation of stress-strain hysteresis loops for MR gel under the given inputs, i.e., *f*, *A*, and *B*.

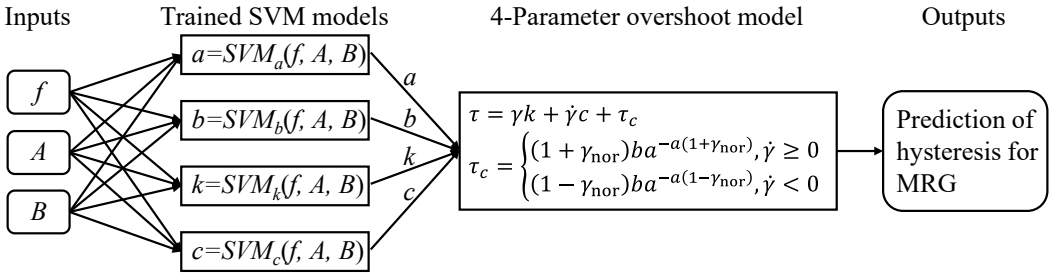

Fig. 5.9 The architecture of the SVM assisted model

In the training process for SVM, the identified values of the four parameters in Table 5.2 were used as training data, which considers frequencies of 0.1, 0.5, 1, and, 2 Hz, strain amplitudes of 10%, 30%, 50%, and 100% and field densities of 0, 0.27, 0.46, and 0.91 T. The SVM model contains four sub-SVMs for the four model parameters. Radial kernel function was chosen in the four sub-SVMs. For nonlinear data distribution, the kernel function maps the data into higher dimensions to make the distribution more linearly. Two parameters (gamma, and cost) in the kernel function control the fitting of the SVM. Gamma and cost affect the range that the straining samples reach and the penalty for making errors in prediction, respectively. Higher gamma values generate more support vectors and wider reach of data sample. Too large or too small cost will result in poor model predictions by over-fitting or under-fitting, respectively. To achieve optimal prediction accuracy, the gamma and cost values for the kernel function in each sub-SVM were tuned separately until the R-squared value between the estimation and training data reaches a value higher than 0.95. Table 5.3 summarised the tunned gamma and cost values for the four sub-SVM models. In Fig. 5.10, the estimated parameter values from the trained SVM model and the identified model parameters used in the training were plotted. The

overall R^2 value is 0.997 and suggests that the trained SVM provides accurate predictions of all parameters with frequency, amplitude, and field density are all considered as inputs and can reproduce the hysteresis loops for the test scenarios used for straining process.

Table 5.3 Gamma and cost values for SVM model

	gamma	cost
a	0.5	200
b	0.09	300
k	0.05	800
c	0.5	50

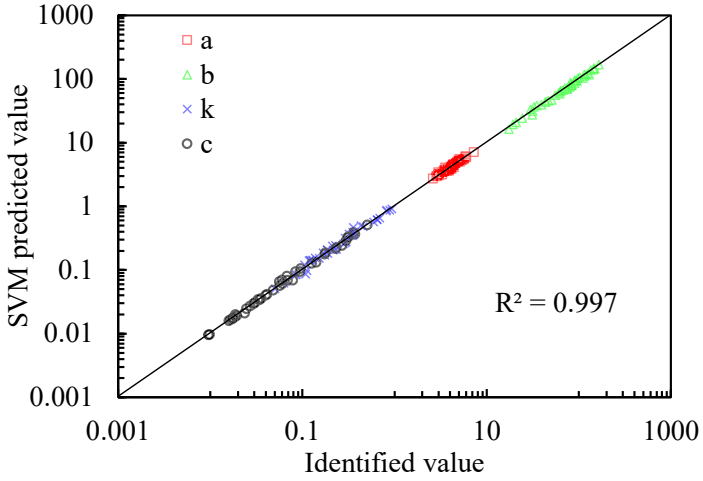

Fig. 5.10 Correlation of the SVM estimation and identified model parameters.

However, the SVM assisted model should be further validated for test scenarios that were not used in the training process to prove the effectiveness of generalization. The hysteresis loops of MR gel under strain amplitudes of 20%, 40%, 60%, and 80%, frequencies of 0.1, 0.5, 1, and, 2 Hz, and field densities of 0, 0.27, 0.46, and 0.91 T were used as inputs for the formulated SVM-assisted model. The measured hysteresis loops and estimations from the SVM-assisted model are compared in Fig. 5.11 and 12, which suggest well agreement between the experiments (solid lines) and the prediction (dotted lines). Fig. 5.11 (a), (b), (c) and (d) show the result for 0.64 T scenario under the frequencies of 0.1, 0.5, 1, and 2 Hz,

respectively; In each of these four plots, hysteresis loops under different strain amplitudes (20%, 40%, 60%, and 80%) are compared. The ideal fitting between the experimental data and the results from the SVM assisted model suggests that the proposed model is capable of describing the effects of both excitation frequency and strain amplitude for MR gel. The effectiveness of the SVM assisted model of depicting the influence of magnetic fields is presented in Fig. 5.12, for 20% strain and 2 Hz frequency; and, the model traced the experimental results closely for all magnetic fields considered. These results suggested that the proposed SVM-assisted model can accurately describe the hysteretic behaviour under the influences of frequency, strain amplitude, and magnetic field for MR gel; and, the application of SVM in the model for generalization purpose is practical.

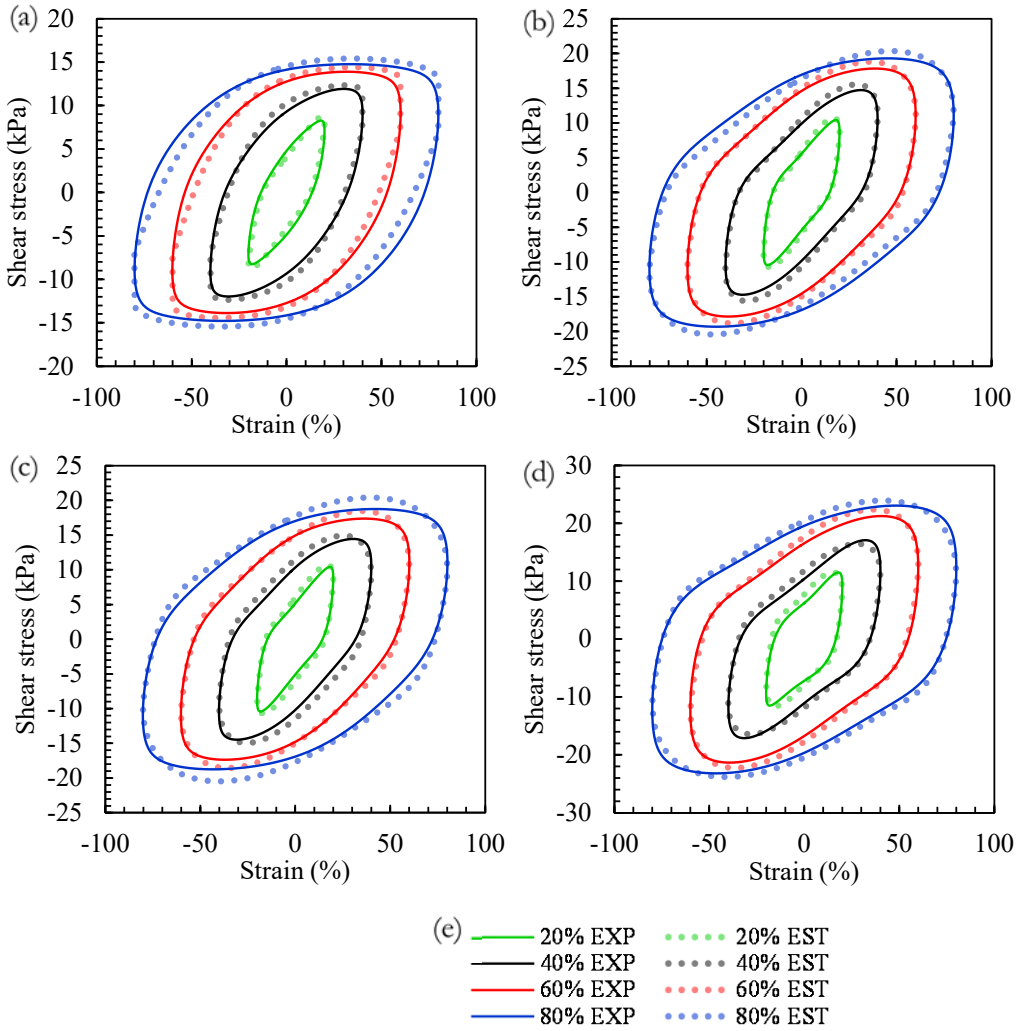

Fig. 5.11 Experimental data and simulation results of the SVM assisted model result under 20%, 40%, 60%, 80% strain when 0.64 T applied (a) 0.1 Hz; (b) 0.5 Hz; (c) 1 Hz; (d) 2 Hz; (e) the legend for Fig. 5.11(a) to (d).

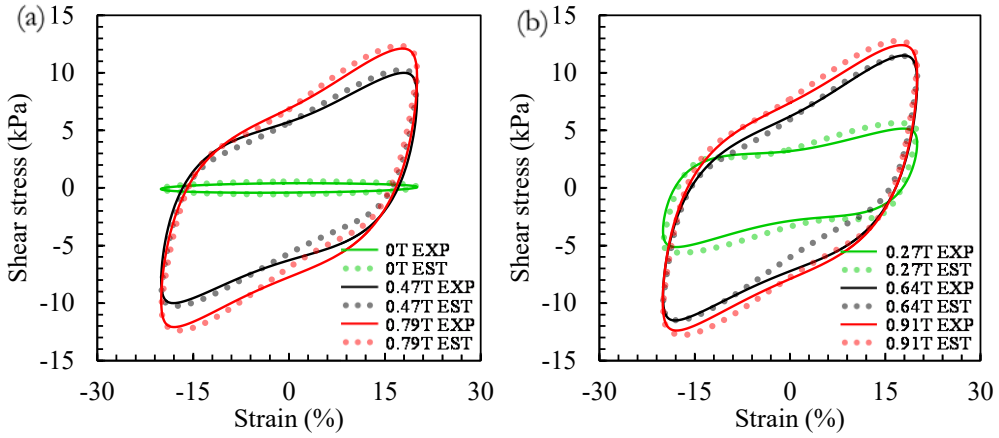

Fig. 5.12 Experimental data and simulation results of the SVM assisted model result under 20%, 2Hz when (a) 0, 0.47, 0.79 T applied; (b) 0.27, 0.64, 0.91 T applied.

5.4 Conclusion

As a recently developed controllable material, MR gel exhibits high adjustability in the material properties and excels in the sedimentation performance which can benefit the development of controllable devices. However, the nonlinearities of MR gel under the application of different levels of the magnetic field is unique from other controllable materials, i.e., MR fluid and MR elastomer. Moreover, in the characterized stress-strain hysteresis loops, clear overshoot of shear stress was observed at the reverse of shear flow when low magnetic field applied (0.27 T). The occurrence of this phenomenon could cause severe instability and false control feedback of adaptive devices.

This research characterized its dynamic hysteresis performances under a broad band of excitations and external magnetic field to take the full advantages of MR gel and achieve precision control of the adaptive devices. A simple and accurate four-parameter phenomenological model was proposed and validated with the characterized hysteresis data of MR gel. This model is based on the variation of a classic Kelvin-Voigt model with adding a proposed overshoot element. The proposed phenomenological model showed good agreement with experimental data; and its identified parameters were analysed for the dependencies on the magnetic field and excitation inputs. By implementing SVM to the proposed phenomenological model, an SVM assisted model was formed and showed excellence in tracing the stress-strain performances of MR gel under all the excitation frequency, strain amplitude, and magnetic field considered. And the magnitude and location of stress overshoot under a low magnetic field were also accurately described. These results proved that the proposed models have the effectiveness of predicting the dynamic hysteresis behaviours for MR gel under varying magnetic fields and excitations; and the applicability of employing in the control algorithms.

Chapter 6

Characterisation and Modelling of Thixotropy for MR Gel

In this chapter, a mini review is prepared to elaborate the physical explanation, characterisation, and modelling of thixotropy first. A thixotropy model for MR gel based on the available flocculation models is then formulated. MR gel is the characterised by thixotropy loop tests and shows typical thixotropic behaviours on rheometer. However, the results from thixotropy loops are only limited in the qualitative aspects. A stepwise test protocol is proposed for characterising the thixotropy of MR gel with considering the influences of resting time, shear rate and magnetic field. Predictions from the proposed model is validated with the experimental results and showed good agreement. Finally, discussions on the thixotropy of MR gel from the engineering application perspective will be presented.

6.1 Introduction

Magnetorheological gels are comprised of micron-sized ferromagnetic particles, i.e., nickel particles, iron particles and carbonyl iron particle (CIP), and polymeric gel matrix, i.e., polyurethane and carrageenan [168, 169]. The free-flowing ferromagnetic particles dispersed in the gel matrix can form chain-like and columnar microstructures that parallel to flux direction of applied field. Through adjusting the flux density, the tannable material properties can be achieved, so-called magnetorheological (MR) effect. Compared with the other classes of the MR material, MR gel can be placed in the intermediate between MR elastomers and MR fluids and mitigates their inherent limitations. In MR elastomers, the elastomeric matrix trapped the mobility of ferroparticles, thus resulting in approx. 50 times lower MR effect than that of MR gel which can exhibit over 200 times increase in the storage modulus [29, 54]. Owing to the higher viscosity of polymeric matrix than the carrier oil of MR fluid, MR gel showed significant enhancements in the shear stress, sedimentation performance and application stability compared with MR fluids [70].

Despite the fact that using polymer as matrix offers fascinating performance improvements for MR materials, compositions of high viscosity polymer and particles normally exhibit reversible and irreversible structural changes which highly depends on the shear flow rate and the recent history of flow [31]. The time-dependent reversible change under flow is defined as thixotropy [170]. This phenomenon is reflected to the microstructures in the suspensions, i.e., junctions of polymers and particle flocs, which take finite time to evolve to another state and back again when subjected to different flow conditions and resting. During the thixotropic transition, three kinds of interactions were normally identified: structure break-down by flow stress, build-up by collisions in the flow and Brownian motion. Due to Brownian motion, the atoms and molecules are constantly agitated and the elements in the suspension will move to positions or state where sufficient

attractive force can be provided to form these elements into microstructures. The thixotropic behaviour in the particle filled polymer suspensions is thus inevitable.

At the macroscopic level, after the steady state of the composite is reached, the correlation of yield stress and shear rate can be well portrayed by rheological models, i.e., Bingham, power law and Hershel Bulkley models. But the shear stress evolution over time between successive steady flows of different shear rates, as shown in Fig. 6.1, cannot be properly described by the yield stress models. In Fig. 6.1, the red dashed lines refer to the resulted shear stress in respect of the transitions of shear rates (the black solid line) over time. As the linear increased shear rate is applied to a material which has been rested for t_1 seconds, the shear stress grows linearly to the static shear stress noted as τ_{0s}. After t_2 seconds, τ_{0s} gradually decreases to a dynamic yield stress τ_{0d} under a constant shear rate as the balanced state of flocculation and de-flocculation processes was reached. As the instantaneous increase and decrease of shear rate occurred at t_3 and t_4, the delayed response of shear stress is caused by the thixotropy in the composite. It has been shown recently in several investigations that the magnitude of τ_{0s} and the delayed response of shear stress is associated with resting time and shear rate; and the steady state τ_{0d} does not relate to the past flow history [171, 172].

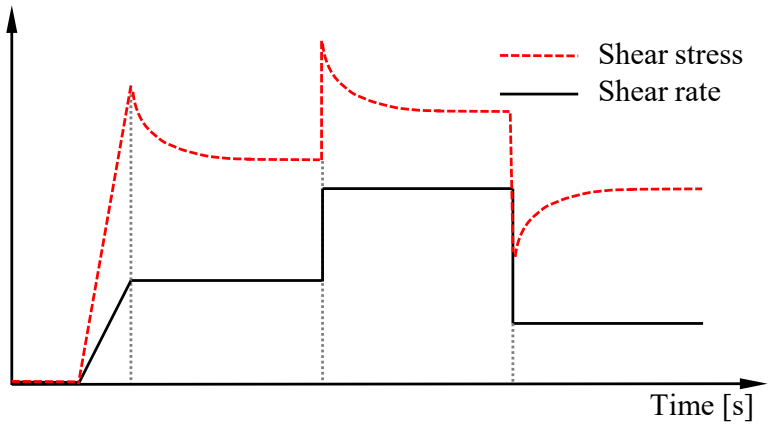

Fig. 6.1 Shear stress evolution under changing flows

However, thixotropy in magnetorheological suspensions is complicated by the involvement of magnetic fields which not only vary the steady states τ_{0d} values, but also constantly interfere the flocculation and de-flocculation of the ferroparticle microstructures. As a result, the evolutions from static yield stress to the steady state will also depend on the magnitudes of the magnetic field. In the recent investigation by Wang *et al.* [173], cellulose nanocrystal filled MR fluids were fabricated and exhibited 7000-fold increase in the shear stress as the magnetic flux density increased from 0 to 0.3T. The thixotropy loop induced 3000 time increase in the enclosed loop area which refers to the magnitude thixotropic behaviour. Li *et al.* reported the similar finding that magnetic fields tend to increase the enclosed areas of thixotropic loop [174]. Stepwise experiments were also performed and showed that the recovery of ferroparticle microstructure is rather quickly under the magnetic field. Although characterising time-dependent rheological behaviour by thixotropy loops has limitations, which will be detailed in *section 2.4*, the current findings suggested that magnetic field acts differently on the rheological behaviours and the evolutions of microstructure in the MR fluids.

For polymeric-gel-based MR gel, the influence of magnetic field on the thixotropy has not been investigated before. As a promising candidate to improve the stability, sedimentation performance and control precision of shear mode controllable devices, i.e., dampers, suspensions, and clutches [8, 175, 176], the ignorance of thixotropic effects may result in the degradation of control precision during the starting state and transitions between two stead states of the developed applications. Thus, the characterisation of the time dependent rheological effects for MR gel is of urgent demand.

6.2 Literature review

6.2.1 Physical explanations of thixotropic behaviour under magnetic fields

One of the classic explanations of thixotropy is presented in [177]. Interactions between particles and carrying matrix decide the potential energy well, noted as ΔE, for a particle. As shown in Fig. 6.2, the particle will be trapped in the well unless an energy higher than the ΔE was given to the particle by the external stress or strain. In the macroscopic view, flow occurs after certain number of particles leave their potential energy well, which is call yield stress behaviour. For a thixotropic system, the ΔE increases when the resting time prolongs, as the result of the interaction of Brownian motion and evolution of the dispersion microstructure during resting.

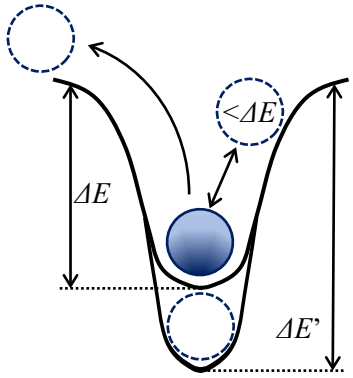

Fig. 6.2 A physical explanation of thixotropy for a particle filled dispersion without magnetic field

For a thixotropic system containing ferroparticles under magnetic fields, this theory becomes inadequate to quantitively explain the energy required for a particle to leave the well at the microscopic level, due to localized anisotropy caused by the formation ferroparticle chain structures. Particles in or near the chain structure require much higher energy to leave the well than that of a free-flowing particle. Also, the size of the chain structure affects the energy required for a particle to leave the structure as larger chains

have lower magnetic reluctances that gives higher flux densities and attracting forces on particles. As a result, the thixotropic behaviour in ferroparticle suspensions could be explained from the macroscopic level when flow occurs.

To illustrate the influence of magnetic field on the particle interactions and flow behaviour, Fig. 6.3 was prepared. In Fig. 6.3, black lines indicate the flow curves for different degrees of flocculation and can be treated as imitations for the flow curves for different sizes of the ferroparticle chain structures under varying magnetic field with assumption that the flocculation will not break-down when subjected to increasing shear rates. In reality, the sizes of the flocculation are not constant because break down and rebuild of the microstructure take place constantly. Thus, extreme shear thinning (blue dotted line on Fig. 6.3) occurs when the flocs are completely broken into particles.

As the magnetic field involves, the attractions between particles become stronger and the evolutions between degrees of flocculation become dependent on the field. On Fig. 6.3, the equilibrium curves intersect with lower flow curves for the decreased flocculation sizes as the shear rate increase; and the involvement of magnetic field results in different initial flocculation status and decreasing pattern of flocculation size throughout the shear process. When a balance state between the de-flocculation and flocculation of the particles is reached, the equilibrium curve will follow the flow curve of a particular size.

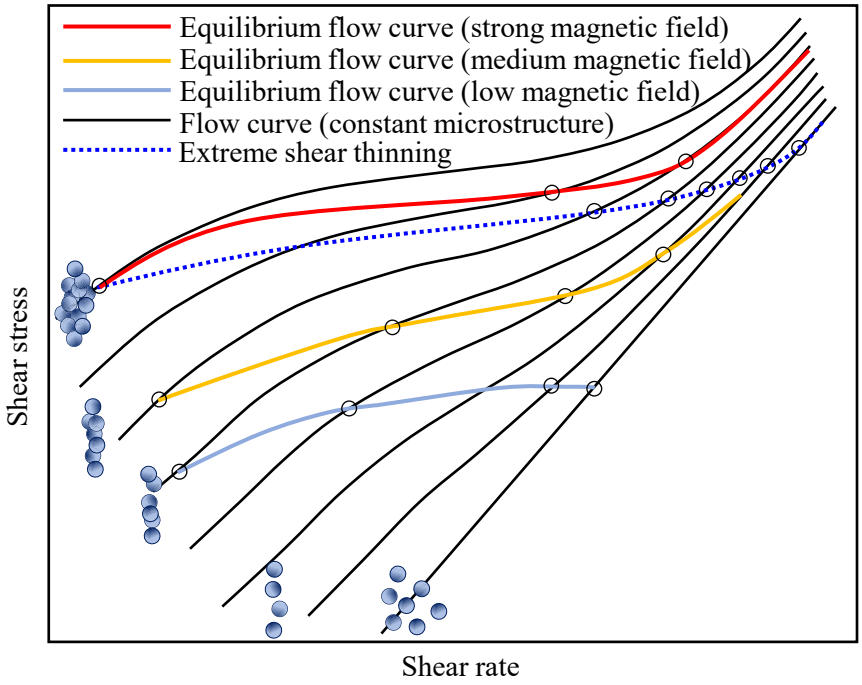

Fig. 6.3 Microstructures and flow curves of a ferroparticle dispersion

6.2.2 Thixotropy models

Towards the modelling of thixotropic effect, two major techniques were reported: phenomenological models and micromechanical models [178-180]. Micromechanical models focus a scientific interpretation in terms of the material compositions, mechanisms, and physics laws. On the contrary, phenomenological models aim to provide general description of the mechanical behaviour of material under complicated characterisation conditions. However, no definitive model is available for both approaches due to complicated nature of thixotropy and the wide range of thixotropy materials. In this review, only phenomenological models will be discussed as they are more versatile and easier to be introduced to the MR materials compared with micromechanical models.

For a phenomenological model of rheological behaviors, viscosity is one of the fundamental parameters to be described, i.e., $\eta = \tau/\dot{\gamma}$ where τ is the shear stress and $\dot{\gamma}$ is the shear rate. To portray the time dependent microstructure, flocculation parameter λ is

introduced as a function of time. This parameter represents the instantaneous status of structure or the "degree of jamming" [181]. In literatures, structure evolution equation for λ is assumed to be dependent on the instantaneous flow condition $\Pi_{\dot{\gamma}}$ and the instantaneous structure [182]. Thus, the thixotropic behavior can be represented as:

$$\tau(t) = f_1\left[\lambda(t), \Pi_{\dot{\gamma}}(t)\right]$$
$$\frac{d\lambda(t)}{dt} = f\left[\lambda(t), \Pi_{\dot{\gamma}}(t)\right] \quad (6.1)$$

Coussot *et al.* [183] adopted the similar principle and proposed the expression of λ to represent the thixotropy:

$$\eta = \eta_0(1 + \lambda^n)$$
$$\frac{d\lambda(t)}{dt} = \frac{1}{\theta} - \alpha\dot{\gamma}\lambda \quad (6.2)$$

where η_0, n, θ and a are material parameters. This model has been proven to be effective for Bentonite suspensions though validate with the magnetic resonance imaging and simulation [184]. Based on this advancement, this model has been adopted to model the thixotropy for cement paste [171, 185]. Roussel [186] derived Eq. 6.2 to the following form:

$$\tau = (1 + \lambda)\tau_0 + k\dot{\gamma}^n$$
$$\frac{d\lambda}{dt} = \frac{1}{T\lambda^m} - \alpha\dot{\gamma}\lambda \quad (6.3)$$

where T, m and a are thixotropy parameters and the flocculation state λ is dependent on the flow history. For a state where the steady shear stress is reached, the λ becomes zero which means the thixotropy apparent yield stress $\lambda\tau_0$ is fully eliminated under a constant shear flow. λ will evolve to larger values after resting of the materials. In equivalent to this structure evolution equation for parameter λ, fading memory integrals were applied by Wallevik *et al.* [187] to provide a more practical interpretation of the flocculation and dispersion of the grains.

For the MR materials, the current practices are limited to fit the characterized rheological behavior to models that contains the structure evolution equation. Li *et al.* [174] applied

the structure kinetics model to fit the recover behaviour (storage moduli *G* gradually increase under constant shear rate) of a ferrofluid during a low shear rate interval after a higher rate interval. The structure kinetics model can be written as:

$$\frac{d\lambda}{dt} = h_1(1-\lambda)^a - h_2\dot{\gamma}^b\lambda^c + h_3\dot{\gamma}^d(1-\lambda)^e \tag{6.4}$$

On the right-hand side of Eq. 6.4, the first to the third term are for the rate of formation of the flocculation, flow-induced micro structural break-down and the formation of the structure by shear motion, respectively. h_1, h_3, and h_3, are model constants and parameters *a* to *e* are model fitting parameters. For the recovery stage, only the first term was considered. However, the results are limited in fitting the recovery of storage moduli of the ferrofluid under one magnetic field level.

6.2.3 Characterisation methods of thixotropy

The rheological features exhibited from a thixotropy systems can be summarised as time dependent viscosity decrease under flow in conjunction with reversibility when the flow is decreased or paused. Based on these features, several measurement techniques such as hysteresis and step test were proposed to quantitively characterise thixotropy in various materials. However, reversible and irreversible microstructure changes, time effect and shear history all can introduce fault and limitations to the measurements. The following sections will present discussions on the measurements based on hysteresis and stepwise tests and justifications of applying these methods to characterise thixotropy in MR gel.

6.2.3.1 Thixotropic loop

Characterising thixotropy using hysteresis loops was firstly reported by Green *et al* [188]. It plots the shear stress responses following the sequence of increasing sweep of shear rate from zero to the maximum and then decreasing sweep from the maximum to zero. If the

sample is thixotropic, the measured result will show a hysteresis loop with the increasing sweep exhibiting higher shear stress values than the decreasing curve. This difference is caused by the transient nature of thixotropy. To be specific, the break down and recover of microstructures happen slower (shearing time is enough to reach steady state) than the increasing and decreasing of shear rates to the next value, respectively. The area enclosed by the two curves is used as a characteristic for thixotropy.

However, the measurement is heavily affected by the test procedure. The major concern on this test is that the test time and shear rate change simultaneously. The shear history of each measurement point thus differs from all other points. Also, number of measurement points, shear rate change between points and measurement time of each point will result in variance of loop shape. For the same increasing and decreasing shear rate range, longer measurement time and more points lead to smaller loop area. And there has no imperial guideline proposed on the setting these variables for the tests.

Moreover, the measured hysteresis area is not a physical rheological parameter. The possibility of investigating the influence of the shear rate on the microstructure evaluation over time is limited. For example, hysteresis presented in [173, 174] for MR fluids can only indicate the influence of the magnetic field on the shape and area of the loops; and larger filed density exhibits a larger loop area. The results are limited to be a qualitative identification for thixotropy and a comparison of thixotropy for MR fluids with different compositions, rather than uncover the relationships between the material resting time, shearing time, shear rate and microstructure evolutions for MR suspensions under magnetic fields.

6.2.3.2 Stepwise tests

To mitigate the coupling issue of time and shear rate for the hysteresis loop, methods based on stepwise changes of shear rate or shear stress were proposed. By applying the constant

shear flow to the sample until the stress response reached the steady state one can repetitively produce a reliable reference test status. This status is normally followed by intentions applications of a higher or lower value of shear rate or shear stress. This method also provides the possibility for checking the reversibility of the experimental data by bring the shear rate or shear stress back to the initial level [174].

The stepwise experiments can also characterise another important aspect of thixotropy: flocculation process [186]. By alternatively applying the constant shear flow and zero shear rate resting interval, the flocculation status after different resting can be reflected by the response at the beginning of each shear flow. However, this aspect is normally missing in investigations of MR suspensions. In MR suspensions based adaptive devices, the shutting down or pausing of the shear motion input of the device can be considered as resting the MR suspensions in the device. Different resting time results in different static yield stress of MR suspensions, as the flocculation process constantly occurs during resting. The change of static yield stress in associate with different resting time normally cause the stress overshoot, latency of control and overfeed of magnetic field.

6.3 A thixotropy model for magnetorheological gels

In the case of model suitable to predict the thixotropy of MR gel and potential application point of view, features other than scientific exactitude should be addressed and are listed as follow:

- the evolution between the static yield stress and dynamic yield stress over time of the magnetorheological gel under different levels of magnetic field should be described by the model;
- effect of resting time under different magnetic fields should be included in the model as a reflection on the initial flocculation state λ;

- the model should be easy to apply and have least number of parameters.

The thixotropy model for MR gel is developed based on the basic thixotropy principal Eq. 6.3. As Bingham model is proven to be effective to describe the rheological behaviour for MR gel [139], Eq. 6.3 can thus be written as Eq. 6.5 with n set to 1, K replaced by plastic viscosity μ_p and m assumed to be 0 for the scenario where the yield stress at rest increase linearly with time.

$$\tau = (1 + \lambda)\tau_0 + \mu_p \dot{\gamma} \tag{6.5}$$

$$\frac{d\lambda}{dt} = \frac{1}{T} - \alpha\dot{\gamma}\lambda \tag{6.6}$$

In the case of constant shear rate, the assumption that the characteristic time of flocculation is longer than that of de-flocculation process, the first term in Eq. 6.6 can be thus neglected. After integration, Eq. 6.6 yields:

$$\lambda = \lambda_{\mathrm{initial}} e^{-\alpha\dot{\gamma}t} \tag{6.7}$$

where a is the fitting parameter. When the time t is equal to zero, the λ yields the initial flocculation state $\lambda_{initial}$ of the MR gel after resting. However, for the practical measurement, the shear stress response can only be recorded after the shear occurred which makes the $\lambda_{initial}$ at t = 0 s point hard to be captured by the rheometer. t_0 and λ_0 were introduced to represent the time consumed to characterise the first data point and its corresponding fluctuation state at t_0. As the magnetic field may introduce variation of shear stress evolution pattern, the constant e is replaced by a variable β for a more accurate and flexible fitting outcome of the phenomenological model. The Bingham model assumes the dynamic shear stress to be linear with shear rate. The measured results in Fig. 6.6 show linear trend but still have certain deviations. For a shear rate where the Bingham model cannot precisely output the steady state shear stress τ_0, the accuracy of the thixotropy model will be greatly degraded. This is because of the thixotropy in MR gel normally shows a smaller magnitude of shear stress evolution when compared with the two or even three

times change observed in concrete. A term τ_m is added to the model to compensate the inaccuracy of Bingham model. τ_m can be calculated through:

$$\tau_m = measured\ steady\ state\ shear\ stress - (\tau_0 + \mu_p \dot{\gamma}) \quad (6.8)$$

This term can also contribute to capture the shear stress increase caused by the remanence in CIPs which will be detailed in section 4.4. The developed thixotropy model for MR gel thus writes:

$$\tau = \left(1 + \lambda_0 \beta^{-\alpha\dot{\gamma}(t-t_0)}\right)\tau_0 + \mu_p \dot{\gamma} + \tau_m \quad (6.9)$$

The flocculation state λ_0 and thixotropic yield stress $\Delta\tau$ at t_0 can thus be derived and represented as Eq. 6.10 and Eq. 6.11.

$$\lambda_0 = \frac{shear\ stress\ at\ t_0 - measured\ steady\ state\ shear\ stress}{measured\ steady\ state\ shear\ stress} \quad (6.10)$$

$$\Delta\tau = shear\ stress\ at\ t_0 - measured\ steady\ state\ shear\ stress \quad (6.11)$$

6.4 Experimental results

6.4.1 Material and testing setup

The MR gel sample with 60% weight fraction of CIP (spherical, 3.5 μ diameter, Beijing Xing Rong Yuan Technology Co., Ltd., China) was studied. The gel matrix is polyurethane (type CT001, Shanghai Shengju Co., Ltd., China). Polyurethane is normally synthesized by toluene diisocyanate and polypropylene glycol; and its viscosity can be easily tailored by the ratio between the diisocyanate and glycol. Higher diisocyanate concentration gives higher viscosity of the polyurethane [29, 65]. The fabrication process of MR gel includes four steps: weighting the polyurethane and CIP following the weight ratio of 2:3; mixing the two components evenly at 60 ˚C for 30 minutes with the mixer set at 500 rpm; placing the mixture in the vacuum drying machine at the temperature of 25˚C for 2 hours to remove air bubble; resting the mixture at 25˚C for two days. The fabricated MR gel appears

as black viscous gel as shown in Fig. 6.4(a). When magnetic field applied, the sample appears as semi solid with small column structures as shown in Fig. 6.4(b). The magnetization curves of the MR gel sample and CIP were measured by a vibrating sample magnetometer (VSM, Lake Shore 7407, USA) at 22°C and presented in Fig. 6.4(c). The superparamagnetism at zero field strength indicated that no large floc was formed in the suspension and proved the stability of the fabricated MR gel.

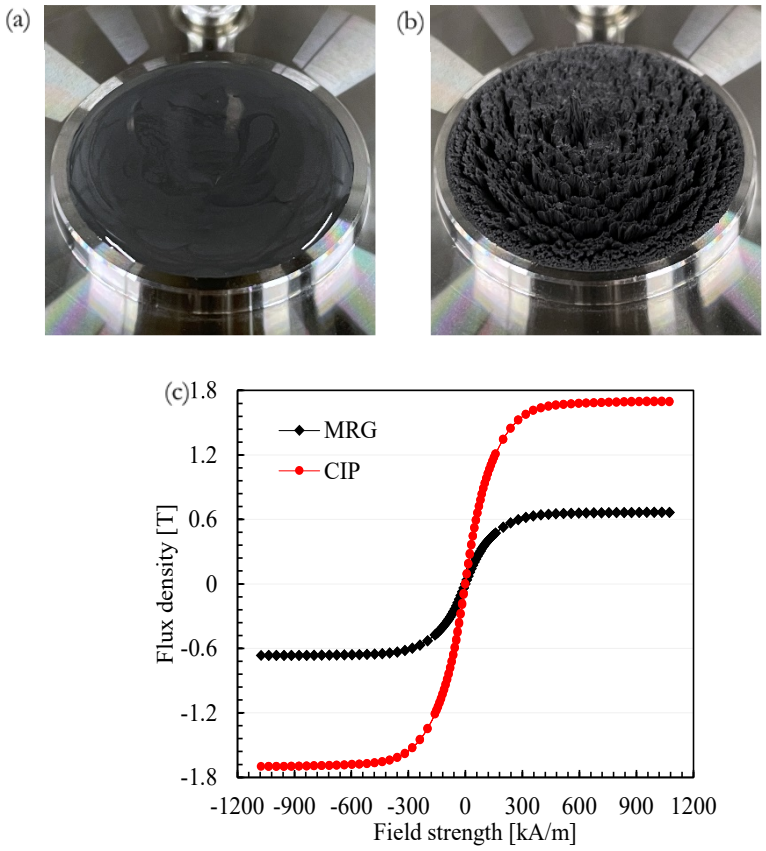

Fig. 6.4 Photo of MR gel and magnetization curves (a) Fabricated MR gel sample (b) MR gel under magnetic field (c) 60% CIP MR gel and CIP magnetization curve

The rheometer used in this work is MCR 302 rheometer (Physica MCR 302, Anton Paar Co., Austria) equipped with the twin gap measurement system as presented in Fig. 6.5(a). The schematic of the tween gap system is shown in Fig. 6.5(b). In this measurement geometry, the magnetic field (red arrow line) is produced by application of direct current

to the coil which is embedded under the nonmagnetic housing. The direct current is supplied by a separate power unit (PS-MDR/5A, Anton Paar Co., Austria) and controlled by the rheometer software. The nonmagnetic housing serves as the container for the MR gel sample while having a slot opened at the bottom to accommodate a hall probe for the magnetic field measurement. A magnetisable disk is embedded in the nonmagnetic housing and guides the magnetic flux to the inner cylinder (20 mm diameter) where contains the MR gel sample. The two-part yoke is applied as a magnetic bridge to form uniform magnetic field oriented vertically to the measurement gaps. The rotor (TG16, Anton Paar Co., Austria) is magnetisable; and the plate of the rotor (16 mm diameter; 1mm thickness) forms two 0.3 mm measurement gaps with the nonmagnetic housing and the yoke. This enclosed geometry well prevents the sample centrifuging out issue of parallel-plate geometry which has the sample sandwiched between two plates with the lateral side unshielded. The deformation of MR gel under magnetic field causes an increased normal force. The two gaps balance the normal forces on top and bottom of the rotor plate thus improve the measurement stability.

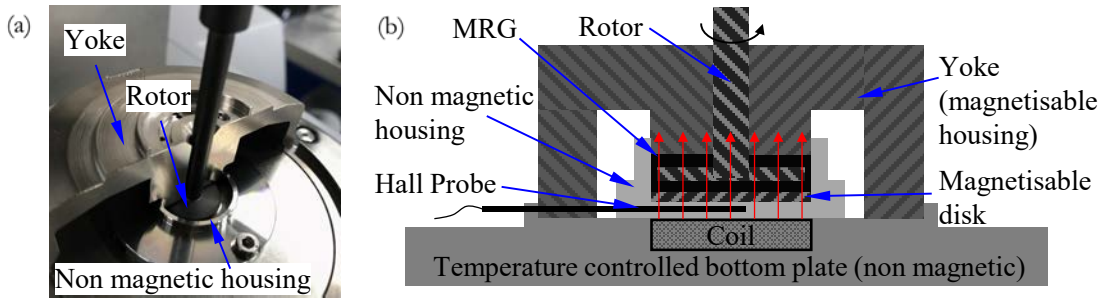

Fig. 6.5 Twin gap measurement geometry (a) photo of twin gap geometry (b) schematic of twin gap measurement geometry

Three types of tests (steady shear test, thixotropy loop test and stepwise thixotropy test) were designed to portray the time dependent rheological behaviours of MR gel which will be detailed in the following sections. For all tests, four levels of current applied to the coil

are 0, 0.2, 0.4, 0.6 A which can generate 0, 0.1, 0.2, 0.3 T flux density, respectively. The magnetic fields were measured by a teslameter (FH54, Magnetic Physics Inc., Germany) with a hall probe (HS-TGB5, Magnetic Physics Inc., Germany). Temperatures was maintained at 21˚C ± 0.05 ˚C for all measurements by a circulating temperature module (C-PTD 200, Anton Paar Co., Austria) connected to the temperature controlled bottom plate. The volume of MR gel loaded in the nonmagnetic housing for each test is 0.4 mL. Demagnetisation was performed immediately after every test to eliminate the remanence in the magnetisable rotor.

6.4.2 Steady state behaviour

The steady shear tests were firstly conducted to characterise the basic rheological behaviours of MR gel at their steady states under the four levels of magnetic field. Successive shear rate steps of 3000, 4000, 5000, and 6000 s^{-1} were considered. It should be noted that each shear step should be long enough that the measured shear stress value reaches the steady value. In this experiment, each step takes 30 s when the flocculation parameter λ decreases to zero in Eq. 6.9. The measured results (solid lines) are fitted with Bingham model (dotted lines) as presented in Fig. 6.6. The expropriated values of yield stress τ_0 and plastic viscosity μ_p under the four magnetic fields are summarised in Table 6.1 and show the decreasing trend for plastic viscosity and increasing yield stress as the increasing of magnetic Field.

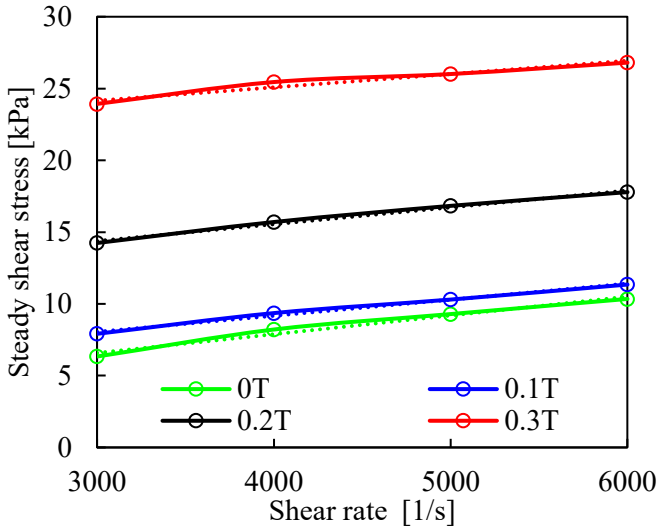

Fig. 6.6 Steady shear stress of MR gel

Table 6.1 Fitted yield stress and plastic viscosity values of MR gel

Magnetic flux density [T]	0	0.1	0.2	0.3
Yield stress [kPa]	2.942	4.807	10.204	21.624
Plastic viscosity [Pa s]	1.2312	1.102	0.98	0.8526

6.4.3 Thixotropic loops of MR gel

In Fig. 6.7, the thixotropy loops are presented for shear rate ranging from 0 to 6000 s^{-1} under the magnetic field of 0, 0.1, 0.2, and 0.3 T. Each hysteresis loop is comprised of two curves for the increase (red lines) and decrease (blue lines) of shear rate. On a single curve, 20 points were recorded with measurement time of 1.5 s for each point. The fabricated MR gel showed thixotropic behaviour for all magnetic fields. The thixotropy for zero filed scenario indicated the loss of junction and deflocculation of CIP. The enclosed area of the thixotropy loop grows with the increase of flux density. However, this phenomenon cannot be simply concluded as the magnetic field increase the thixotropy in MR gel. The magnetic fields also increase the yield stress of the MR gel thus resulting a decrease trend

of thixotropy in relative to the yield stress at the corresponding level. The change of hysteresis shape also suggests an interesting impact of magnetic field at deflocculation process. The down curves for the scenarios with magnetic fields showed concave shapes which can be interpreted as that the magnetic field tends to prevent the break down or accelerate the recovery of microstructures structure in MR gel. However, to present the full picture of the influence of magnetic field and resting on the thixotropy in MR gel, the constant shear test should be conducted, and the flocculation should be investigated which will be presented in the following section.

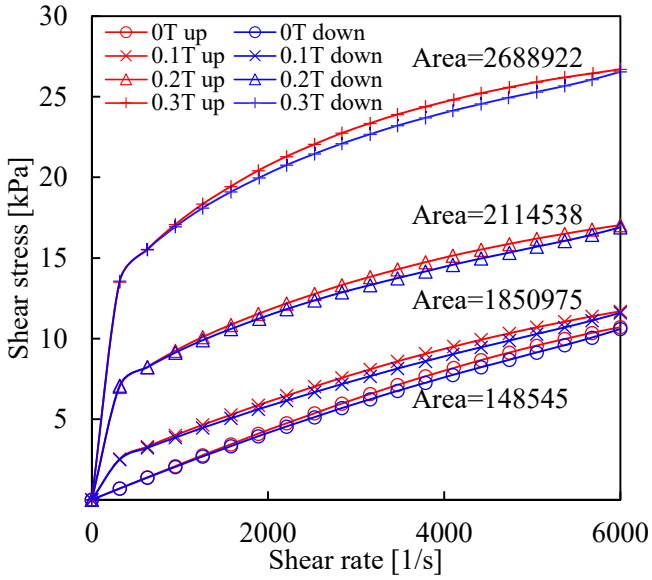

Fig. 6.7 Thixotropy loops of MR gel under the magnetic field of 0, 0.1, 0.2 and 0.3 T

6.4.4 Stepwise thixotropy tests of MR gel

As the thixotropy is a time-dependent and reversible behaviour, a reference state in MR gel should be carefully chosen to compare the influences of the resting time, shearing time, shear rate and magnetic field. Theoretically, the completely flocculated and de-flocculated states can be treated as candidates for referencing the influences on rebuilt and break down of microstructures. In fact, none of the two states can be reached. For the completely flocculated state, MR gel contentiously flocculates under magnetic field and the irreversible

structural changes occurs, i.e., hard cake and remanence of the aggregated ferroparticles. As for the completely de-flocculated state, infinity shear rate is required.

Thus, to characterise time-dependent rheological behaviour of MR gel, an equilibrium state under a constant shear rate and magnetic field is the most suitable since the balance between the structural break down and rebuilt is reached. If the equilibrium state of a constant shear rate follows a resting time, the de-flocculation process stops, and the microstructure starts to rebuild. By varying the length of the resting time, different levels of recovery can be then characterised applying an instantaneous shear motion of the same shear rate. Under different combinations of shear rates and magnetic fields, although the resulted dynamic yield stresses are different, the effect of different resting periods can be compared, as long as the shear motion and the magnetic field is constantly applied until MR gel reaches the steady state.

This work proposes a test protocol for MR gel based on the stepwise experiments with choosing the equilibrium state under a constant shear rate and magnetic field as the reference states. The test waveform (Fig. 6.8) comprises of three types of intervals which are pre-shearing interval (black sold line), resting intervals (red sold line) and shearing intervals (blue sold line), with total running time of 315 seconds. The value of shear rate is not specified on Fig. 6.8 as in each test only one of the four designated shear rates (3000, 4000, 5000 and 6000 s^{-1}) is configured. A 30-second pre-shearing was performed at the beginning of each test. It should be noted that, compared with other rheological characterisations, the purpose of the pre-shearing adopted in this work is to bring the MR gel to the "most deflocculated" reference state (see section 6.2.2), rather than eliminating the discrepancy in the initial microstructure of the measured samples and avoiding transient behaviour. The first resting interval lasts 1 s and is placed after the pre-shearing. Then, the first shearing interval is applied for 30 s at a designated shear rate to characterise the shear stress evolution between the initial flocculation state and the steady state. Then,

the resting intervals (4, 10, 30 and 90 s) and shearing intervals take place alternatively. In this way, the fluctuation state at the beginning of each resting interval (or at the end of each pre-shearing and shearing interval) are the same and the influence of resting time on the flocculation process can be compared. For each shearing interval, the measuring time of one data point is 1 s thus total 30 points were sampled for each shearing interval. The magnetic is maintained at the same level throughout all intervals and four levels of flux density were considered which are 0, 0.1, 0.2, and 0.3T. New MR gel sample is applied for each test and demagnetisation were performed at the end of each test.

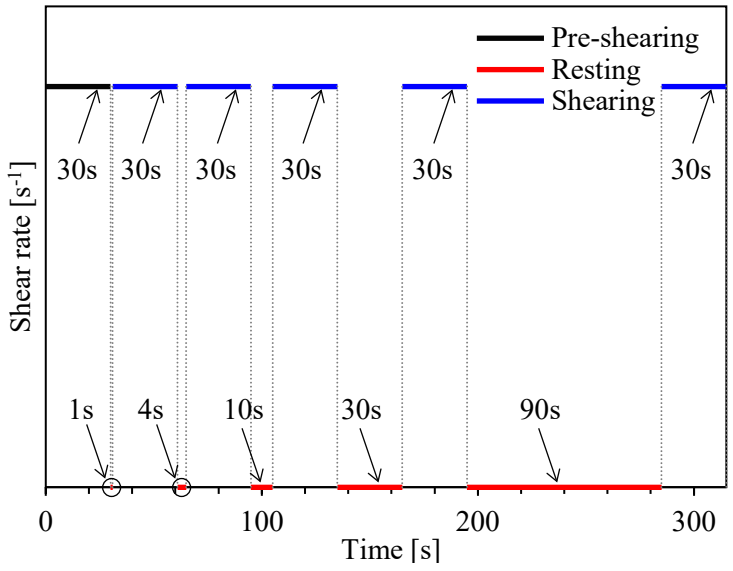

Fig. 6.8 Excitation waveform of stepwise thixotropy tests

The measured shear stress response of shearing intervals for the shear rates of 3000, 4000, 5000 and 6000 s^{-1} were plotted as solid lines on Fig. 6.9 to Fig. 6.12, respectively. It should be noted that the time on horizontal axis is in respect to the start of the shearing interval. In this way, the flocculation state after different resting time, which is manifested by the measured shear stress at t_0 = 1 s, can be compared in a clear manner. It can be observed after each resting interval, the shear stress presents a decreasing trend until it comes approximately to the dynamic yield stress. And this de-flocculation process is in line with the theoretical interpretation in Fig. 6.1. This confirms that the rheometer is able to probe

the reversible thixotropy behaviour and break the recovery during the resting interval. The shear stress significantly drops within the first 5 seconds of the shearing interval and gradually approaches to the steady state at approx. 10 seconds. Under the scenarios with and without magnetic fields, the de- flocculation patterns are similar.

However, comparing the dynamic yield stress after 1 and 90 seconds resting, discrepancies can still be observed which appears to have a larger value after the 90-second resting. The differences in the dynamic yield stress are less than 0.4 kPa and tends to increase at larger flux densities; and the differences are smaller in the cases without magnetic field. These suggest the occurrence of irreversible microstructure change in MR gel after long resting time under magnetic fields. Although CIPs are soft magnetic material which does not show magnetism when the external field is removed, the iron particles may have remanence during the long-time application of large magnetic field [189]. The CIPs with remanence may cause a locally larger magnetic field than the external field and form larger flocs; thus, lead to larger dynamic yield stress values.

The modelling results of the proposed model are also presented as dots on Fig. 6.9 to Fig. 6.12. Firstly, the λ_0 were decided through substituting the measured shear stress at t_0 to Eq. 6.9. The shear stress evolution of the shearing period after t_0 can then be obtained by finding the ideal fitting parameter a and β for Eq. 6.9. The proposed modelling results agree with the experimental data.

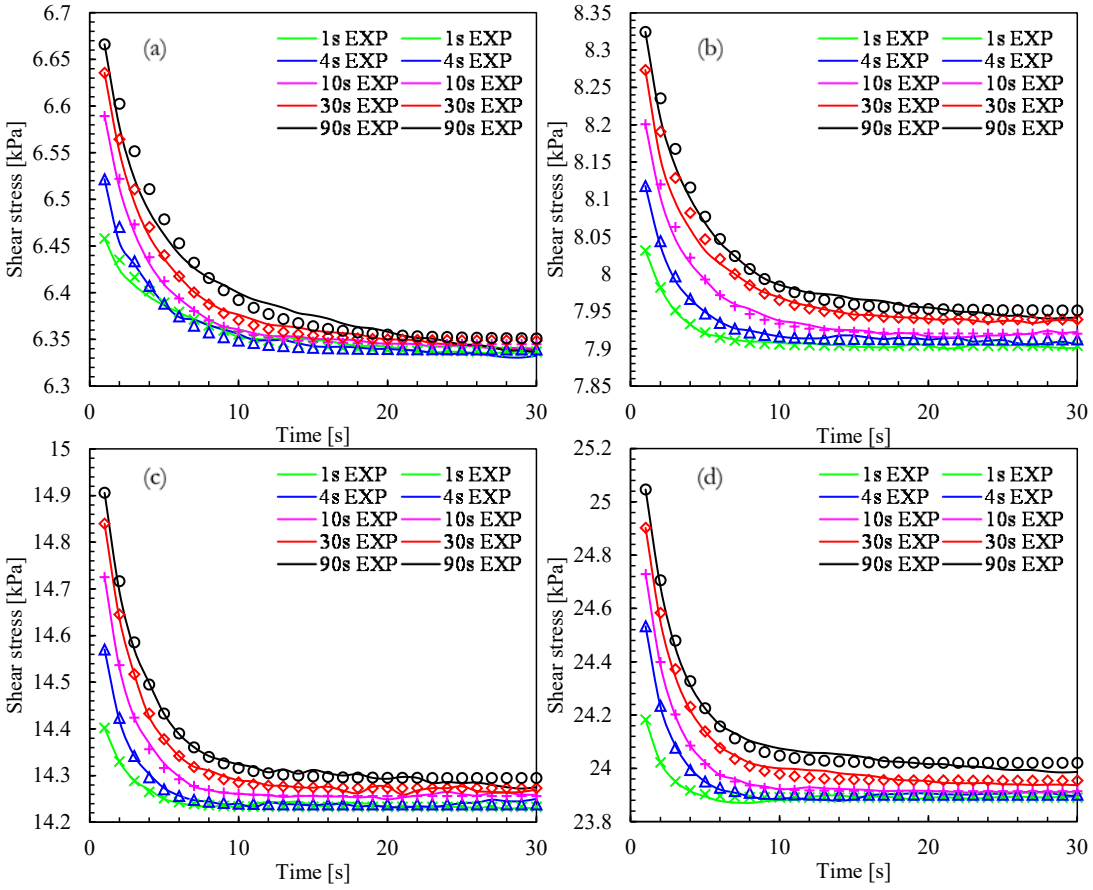

Fig. 6.9 measured and predicted shear stress at shear rate of 3000 s^{-1} under (a) 0 T (b) 0.1 T (c) 0.2 T (d) 0.3 T

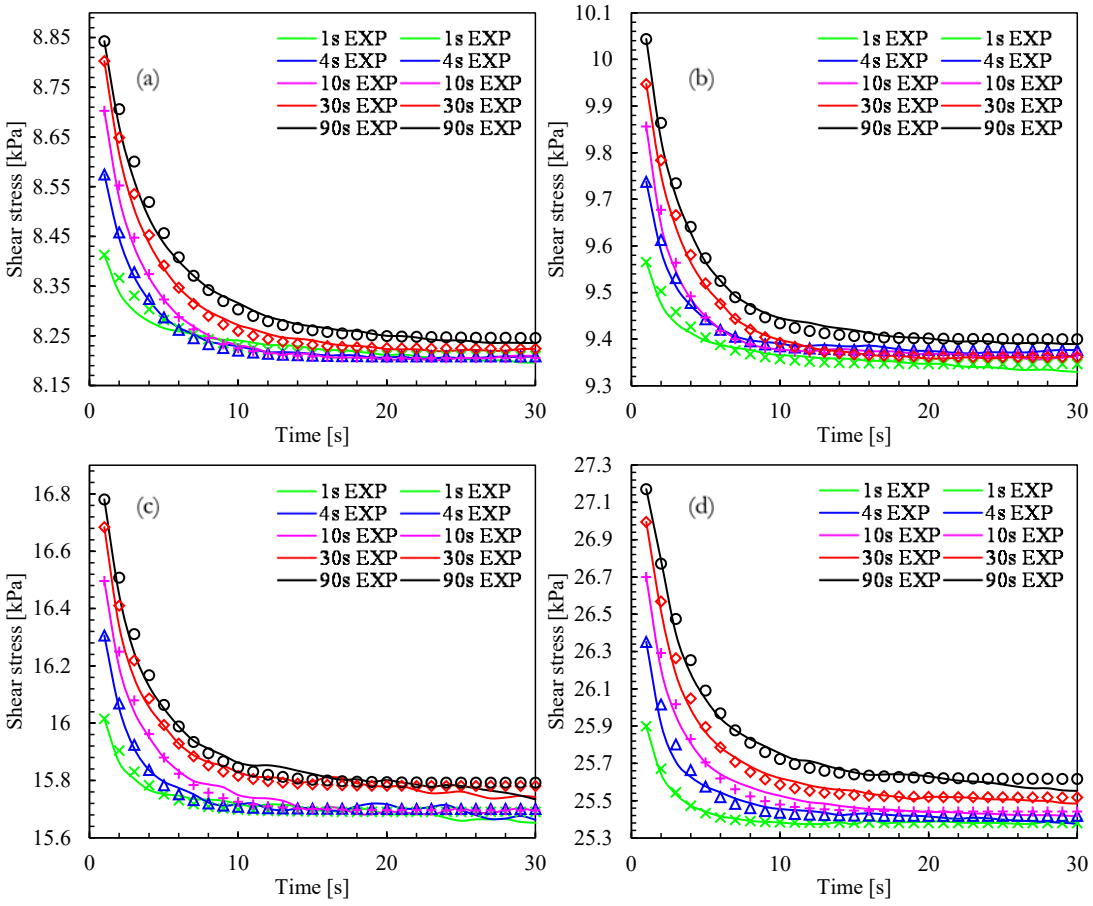

Fig. 6.10 measured and predicted shear stress at shear rate of 4000 s^{-1} under (a) 0 T (b) 0.1 T (c) 0.2 T (d) 0.3 T

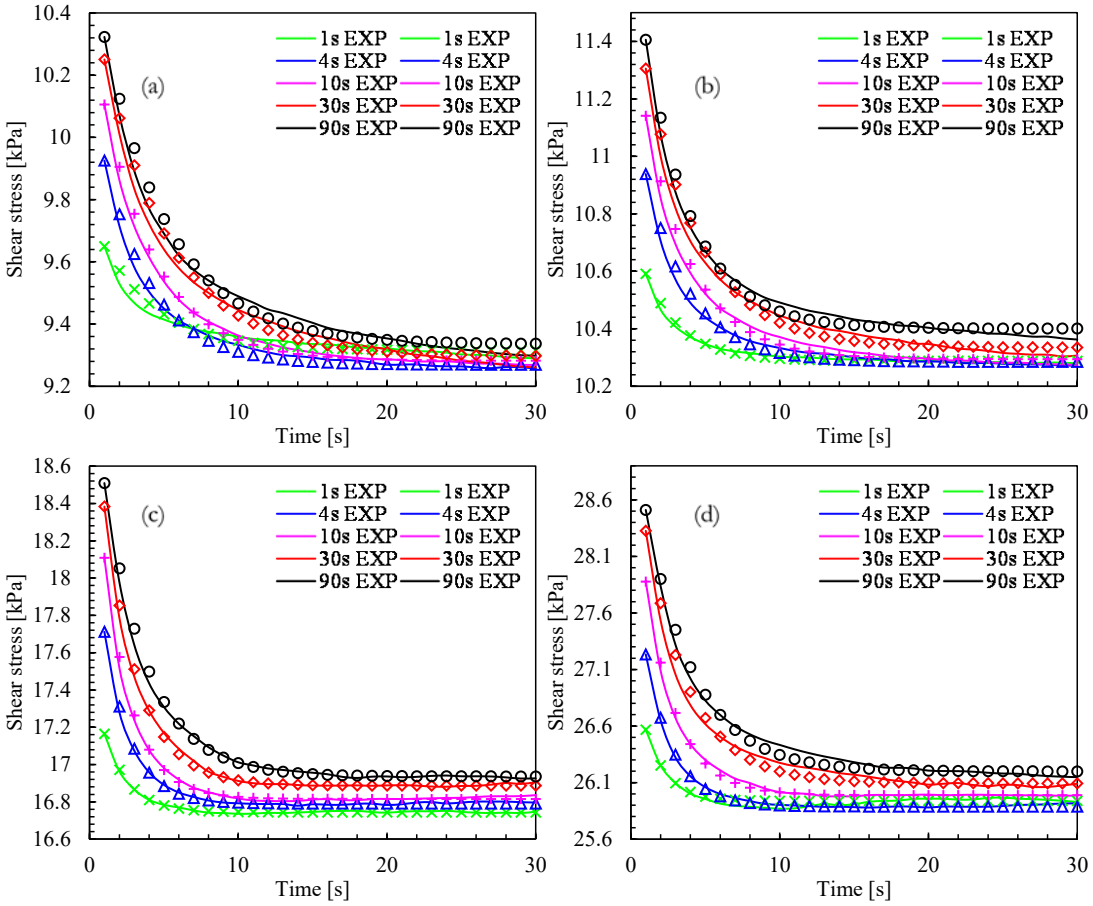

Fig. 6.11 measured and predicted shear stress at shear rate of 5000 s^{-1} under (a) 0 T (b) 0.1 T (c) 0.2 T (d) 0.3 T

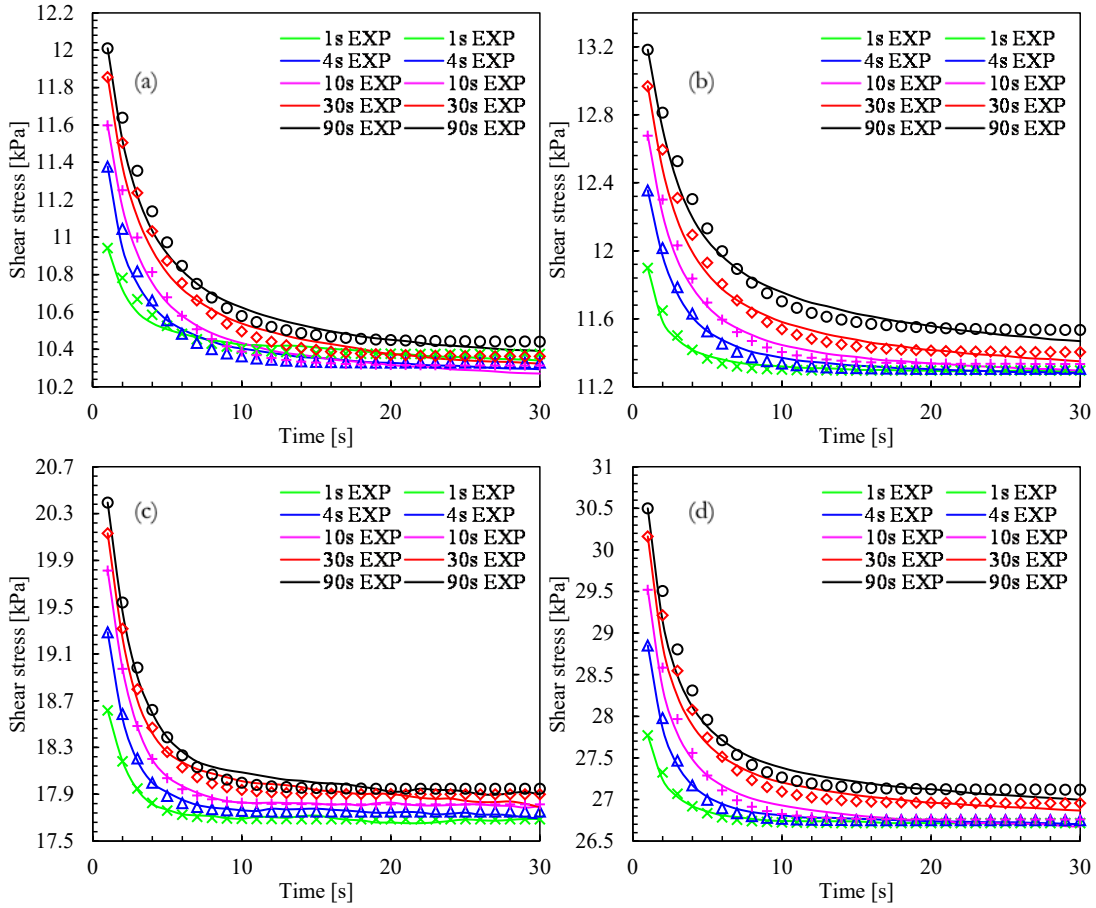

Fig. 6.12 measured and predicted shear stress at shear rate of 6000 s^{-1} under (a) 0 T (b) 0.1 T (c) 0.2 T (d) 0.3 T

6.4.5 Thixotropic yield stress and flocculation state of MR gel

To further understand the influences of magnetic field and resting and shear rate on the thixotropy of MR gel, thixotropic yield stress $\Delta\tau$ and the flocculation state at λ_0 should be discussed. As described in section 6.3, thixotropic yield stress can be represented by the magnitude of stress drop between the first static yield stress and dynamic yield stress, and flocculation states is the ratio between the thixotropic yield stress and dynamic yield stress. Due to the first measurement point is taken at t_0=1 s by rheometer, $\Delta\tau$ and λ_0 at t_0 of MR gel is investigated.

Fig. 6.13(a) to (d) show the thixotropic yield stress of MR gel under the shear rates of 3000, 4000, 5000 and 6000, respectively. It can be observed that resting increases the thixotropic

yield stress for MR gel as expected and is mostly effective in the first 10 seconds. After 30-second rest, the increase in the thixotropic yield stress becomes insignificant. With the increase of shear rate from 3000 to 6000 s^{-1}, $\triangle\tau$ after 90 s resting at zero field dramatically grows from 0.122 to 0.588 kPa. The increase of $\triangle\tau$ at 0.1 T is rather small compared with the zero-field scenarios. Whereas, as the fields increase to 0.3 T, $\triangle\tau$ values are two to three times higher than the zero-field scenarios under all shear rates.

λ_0 values are also plotted in Fig. 6.14. Compared with $\triangle\tau$, shear rate and resting time have similar effects, but magnetic field tends to decrease the flocculation states. this can be explained as magnetic field has a more apparent contribution on MR effect than on thixotropic effect for MR gel. To be specific, the flux density of 0.3 T contributes to approx. doubled thixotropic yield stress compared with that of zero field. As the magnetic field has a more significant in raising the steady shear stress values, λ_0 tends to reduce with the increase of the field. Thus, the effect of magnetic field on thixotropy of MR gel cannot be simply concluded as an increase or decrease trend and should be carefully evaluated by both thixotropic yield stress and flocculation status.

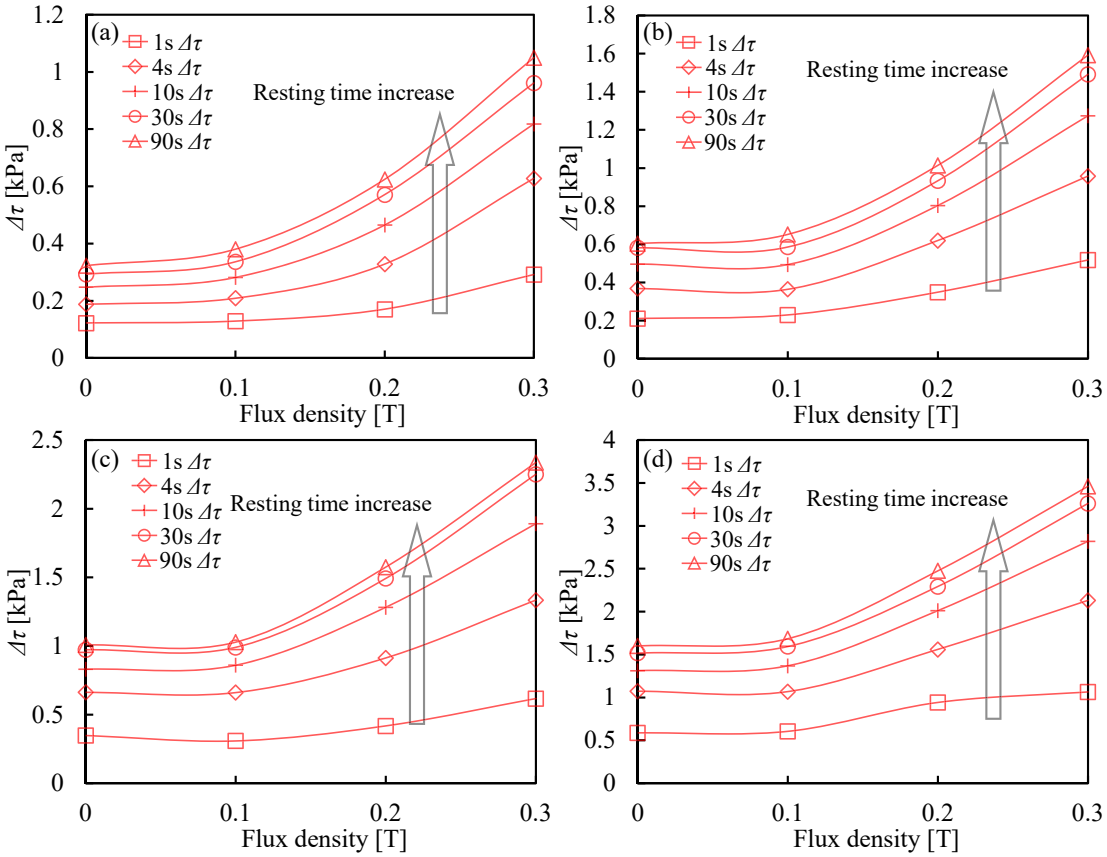

Fig. 6.13 Influence of magnetic field and resting on thixotropic yield stress of MR gel under shear rates of (a) 3000 s^{-1} (b) 4000 s^{-1} (c) 5000 s^{-1} (d) 6000 s^{-1}

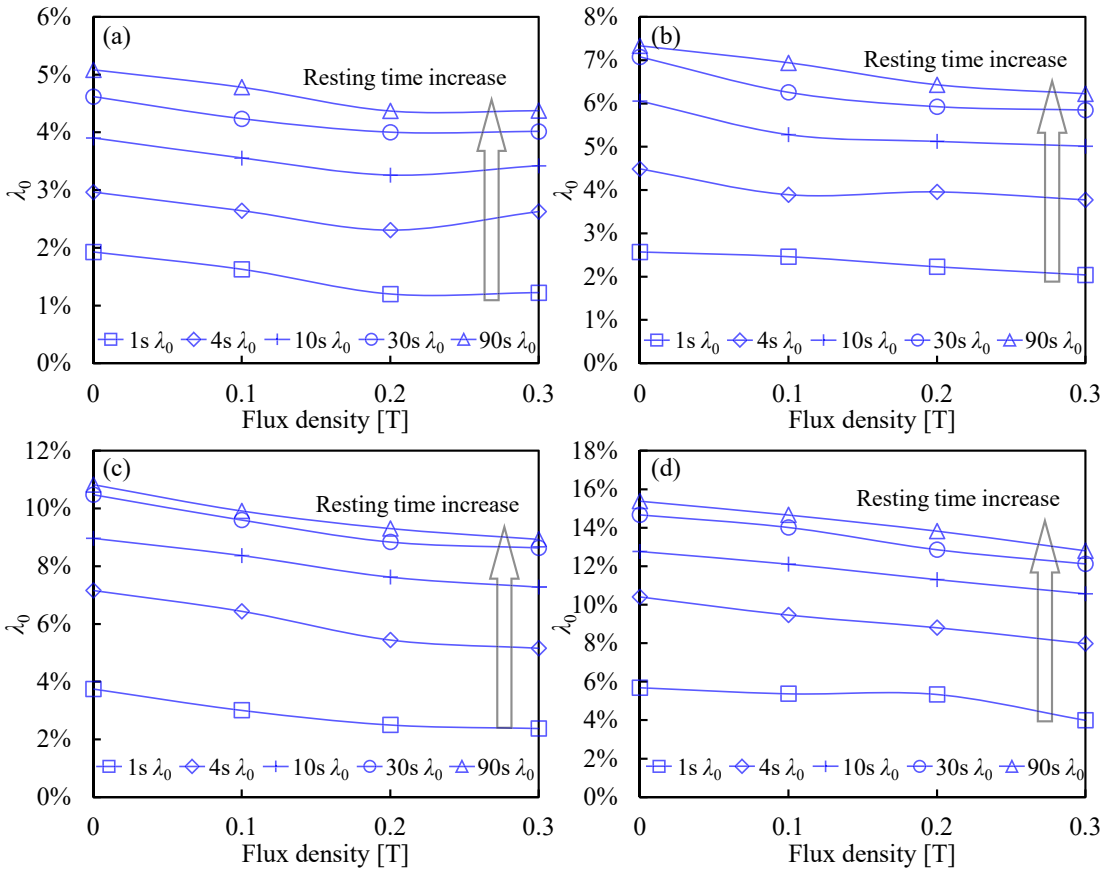

Fig. 6.14 Influence of magnetic field and resting on flocculation state of MR gel under shear rates of (a) 3000 s^{-1} (b) 4000 s^{-1} (c) 5000 s^{-1} (d) 6000 s^{-1}

6.5 Further discussion on MR gel thixotropy

The results in this work indicated the complicated thixotropy in MR gel as a result of the coupling of shear flow and magnetic field. Although MR gel significantly improves the sedimentation performance and yield stress compared with conventional MR fluid, its thixotropy nature may raise challenges in the practical applications. MR materials in the developed devices, i.e., dampers and clutches, are majorly operate in two modes: shear mode and flow mode. And both operating modes can induce the thixotropy.

For device operating in shear mode, a typical application is MR fluid clutch. The shafts disks and the outer cylinder forms the channel to contain MR fluids. By adjusting the

magnetic field that is perpendicular to the shaft disk, the damping property of MR fluid can be tuned, and the different torque transmissibility can be achieved. This operating mode is identical to the twin gap measurement step up in this work. During the clutch running, thixotropy may be involved after the change of speed and altering the magnetic field. If the shaft rotation speed is suddenly increased, the thixotropic yield stress is expected and will gradually decrease to a lower dynamic yield stress. The involvement of the thixotropic yield stress will cause sudden stuck for the clutch during transitions between different speeds. Also, after certain time of shutting off, the increased flocculation state causes a higher thixotropic yield stress. These phenomena are also possible for flow mode device, i.e., MR dampers. In a damper, the piston structures form narrow flow channels with the outer damper cylinder. The piston or the outer cylinder is normally integrated with winding coils that controls the magnetic field in the channel. As the liner motion of the piston takes place, MR fluid flow to the other end of the damper through the channel. In this way, adaptive damping performance can be realized. However, the change of excitation and shutting off lead to different flocculation states thus affect the performance of the damper.

The controlling system may provide solution to compensate or cancel out the thixotropic yield stress. Normally, the rheological models, i.e., Bingham and power law models, only estimate the shear stress response under steady state. The higher values of thixotropic yield stress can be compensated or canceled out by feeding smaller current to the coil then gradually raise the current, as weaker magnetic field exhibits smaller thixotropic yield stress. By introducing the proposed thixotropic model in the control algorithm can provide estimations of the initial flocculation state and the evolution between the thixotropic yield stress steady state stress. Thus, a compensated controlling current can be applied to maintain a smoothed stress response of the adaptive devices.

6.6 Conclusion

In this chapter, 60% weight fraction of CIP MR gel was fabricated. Thixotropy loops and stepwise tests were performed to characterise its thixotropic behaviours. Both tests probed the occurrence of thixotropy behaviour under all four levels of magnetic field (0, 0.1, 0.2, and 0.3 T). The thixotropy loops indicated an increasing trend of the loop area as magnetic field is intensified. More comprehensive findings on the thixotropy of MR gel were revealed through the proposed stepwise tests and are as follows.

- Higher shear rates contributed to more apparent thixotropy behaviours under all levels of magnetic fields considered.
- Resting resulted in the formation of flocculation in the MR gel. The MR gel can recover over half of its reversable microstructures within 10s however, longer resting time under magnetic fields could result in irreversible changes due to the formation of large flocs by the magnetized CIPs (remanence occurred).
- The patterns of shear stress decrease (de-flocculation process) under constant shear rate appear to be similar under all magnetic fields. Thixotropic yield stress rapidly approaches to zero after 10-second shearing.
- Magnetic fields induced approx. doubled thixotropic yield stress for MR gel. However, the flocculation state parameter λ_0 indicated a reducing trend with the intensifying of magnetic field.

A phenomenological model was proposed and validated by the experimental data. The model can well describe the thixotropic behaviours mentioned above under all shear rates, resting time and magnetic fields considered. Finally, the discussions on the effects and potential solutions of thixotropy from the engineering application perspective were presented.

Chapter 7

Conclusions and Future Works

This thesis brings improvement to the existing understanding of gel-like and elastomeric MR materials through experimental characterisation and numerical modelling. In addition to adding this body of knowledge, efficient design, accurate analysis approach and time-dependent magneto-rheology are investigated to facilitate the future development of MR material based controllable devices.

In Chapter 3, a novel shear test rig that features a hybrid magnets system is developed to characterise MR elastomers with advantage of reducing the maximum current to activate the MR effect of MR elastomer. A series of isotropic and anisotropic MR elastomers are characterised and suggests the higher performances, i.e., stiffness, damping and adjustability, of anisotropic samples and samples with higher CIP concentrations. A stiffness stiffening phenomenological is used to model all characterised force-displacement relationships and shows good agreement. This attempt proves that hybrid magnets configuration can enhance the energy conservation, reliability, compatibility and running time for the MR material based adaptive devices.

In Chapter 4, based on the concept of hybrid magnets, an energy-efficient laminated MR elastomer base isolator is design and fabricated. An improved magnetic circuit analysis

approach is proposed to cope with the increased structural complexity brought by laminated structure and hybrid magnets. The accuracy of the model is validated with the results from experimental measurements and finite element analysis. The proposed model provides a simple and accurate solution for a complicated MR device with the great potential to facilitate the design and analysis of relevant engineering applications.

In Chapter 5, the field dependent dynamic properties of MR gel are characterised through oscillatory shear tests and show distinctive difference from the typical behaviours of MR fluids and MR elastomers. At the absence of the magnetic field, it behaves as viscos materials and the application of magnetic field significantly increases the stiffness of MR gel. Moreover, at low flux density (0.27 T), apparent stress overshoot phenomenon is observed. Addressing the characterised unique behaviours of MR gel, a four-parameter phenomenological model is formulated and generalised by support vector machine. The proposed model accurately predicts the behaviours of MR gel and could avoid instability and false control feedback for adaptive devices.

In Chapter 6, thixotropy of MR gel is characterised by a proposed stepwise characterisation technique under various magnetic fields, shear rates and resting periods. The results indicate that thixotropic effect could occur regardless of magnetic field with the resulted and up to 15% decrease in the shear stress under the constant shear rate of 6000 1/s within 5 seconds. Moreover, the over half of decreased shear stress can be recovered after a 10-second resting period. Ignorance of these effect could trigger control failure and unstable performance during the start-up and changing shear rates of the developed application. Thus, this work delivers a thixotropy model to portray the shear stress evolutions caused by thixotropy and a discussion for the influence of thixotropy on MR applications.

The scope and progress of this research have been impacted by the COVID-19 pandemic – being the non-operation of the essential shake table facility and unavailability of technical repairing support since February 2020 to date. The investigation of the performance of

the proposed hybrid magnets MR elastomer base isolator using shake table is thus planed in the future work. This investigation includes uniaxial and bidirectional shear tests which can shed light on the development of adaptive seismic isolation for infrastructures.

Another research task concerns the properties and application of MR gel. As the current understanding of MR gel is not sufficient to deliver effective and efficient engineering application, future works should include the aspects of influence of temperature, sedimentation performance, and off-state viscosity.

Finally, based on the hybrid magnets configuration and improved magnetic circuit model, attempts could be carried out in designing a hybrid magnets MR-gel-based device which could resolve the sedimentation, low MR effect and energy consumption issues of the current MR material applications.

Reference

[1] D.W. Felt, M. Hagenbuchle, J. Liu, J. Richard, Rheology of a magnetorheological fluid, Journal of Intelligent Material Systems and Structures 7(5) (1996) 589-593.

[2] J. Popplewell, R. Rosensweig, Magnetorheological fluid composites, Journal of physics D: applied physics 29(9) (1996) 2297.

[3] X. Guan, X. Dong, J. Ou, Magnetostrictive effect of magnetorheological elastomer, Journal of Magnetism and magnetic materials 320(3-4) (2008) 158-163.

[4] G. Zhou, Shear properties of a magnetorheological elastomer, Smart materials and structures 12(1) (2003) 139.

[5] Y. Xie, M. Yu, H. Qu, J. Fu, Carbon black reinforced magnetorheological gel enabled high-performance magneto-resistor for motor soft start-up, Smart Materials and Structures 28(12) (2019) 125019.

[6] P. Yang, M. Yu, J. Fu, H. Luo, Rheological properties of dimorphic magnetorheological gels mixed dendritic carbonyl iron powder, Journal of Intelligent Material Systems and Structures 29(1) (2018) 12-23.

[7] S.-W. Cho, H.-J. Jung, I.-W. Lee, Smart passive system based on magnetorheological damper, Smart Materials and Structures 14(4) (2005) 707.

[8] S. Guo, S. Yang, C. Pan, Dynamic modeling of magnetorheological damper behaviors, Journal of Intelligent material systems and structures 17(1) (2006) 3-14.

[9] P. Kielan, P. Kowol, Z. Pilch, Conception of the electronic controlled magnetorheological clutch, Przeglad Elektrotechniczny 87(3) (2011) 93-95.

[10] P. Yadmellat, M.R. Kermani, Adaptive modeling of a magnetorheological clutch, IEEE/ASME Transactions on Mechatronics 19(5) (2013) 1716-1723.

[11] Y. Li, J. Li, W. Li, B. Samali, Development and characterization of a magnetorheological elastomer based adaptive seismic isolator, Smart Materials and Structures 22(3) (2013) 035005.

[12] J. Yang, H. Du, W. Li, Y. Li, J. Li, S. Sun, H. Deng, Experimental study and modeling of a novel magnetorheological elastomer isolator, Smart Materials and Structures 22(11) (2013) 117001.

[13] J. Rabinow, The magnetic fluid clutch, Electrical Engineering 67(12) (1948) 1167-1167.

[14] M. Ashtiani, S.H. Hashemabadi, A. Ghaffari, A review on the magnetorheological fluid preparation and stabilization, Journal of Magnetism and Magnetic Materials 374 (2015) 716-730.

[15] Y. Li, J. Li, W. Li, H. Du, A state-of-the-art review on magnetorheological elastomer devices, Smart Materials and Structures 23(12) (2014).

[16] L. Chen, X. Gong, W. Li, Microstructures and viscoelastic properties of anisotropic magnetorheological elastomers, Smart Materials and Structures 16(6) (2007) 2645.

[17] M. Behrooz, X. Wang, F. Gordaninejad, Modeling of a new semi-active/passive magnetorheological elastomer isolator, Smart Materials and Structures 23(4) (2014) 045013.

[18] H.-x. Deng, X.-l. Gong, Application of magnetorheological elastomer to vibration absorber, Communications in nonlinear science and numerical simulation 13(9) (2008) 1938-1947.

[19] S. Li, P. Watterson, Y. Li, Q. Wen, J. Li, Improved magnetic circuit analysis of a laminated magnetorheological elastomer devices featuring both permanent magnets and electromagnets, Smart Materials and Structures 29(8) (2020) 085054.

[20] A.K. Bastola, M. Paudel, L. Li, Magnetic circuit analysis to obtain the magnetic permeability of magnetorheological elastomers, Journal of Intelligent Material Systems and Structures 29(14) (2018) 2946-2953.

[21] M. Cheng, Z. Chen, J. Xing, Design, analysis, and experimental evaluation of a magnetorheological damper with meandering magnetic circuit, IEEE Transactions on Magnetics 54(5) (2018) 1-10.

[22] P.-B. Nguyen, S.-B. Choi, A new approach to magnetic circuit analysis and its application to the optimal design of a bi-directional magnetorheological brake, Smart Materials and Structures 20(12) (2011) 125003.

[23] T. Shiga, A. Okada, T. Kurauchi, Magnetroviscoelastic behavior of composite gels, Journal of Applied Polymer Science 58(4) (1995) 787-792.

[24] M.J. Wilson, A. Fuchs, F. Gordaninejad, Development and characterization of magnetorheological polymer gels, Journal of applied polymer science 84(14) (2002) 2733-2742.

[25] A. Fuchs, B. Hu, F. Gordaninejad, C. Evrensel, Synthesis and characterization of magnetorheological polyimide gels, Journal of applied polymer science 98(6) (2005) 2402-2413.

[26] A. Fuchs, M. Xin, F. Gordaninejad, X. Wang, G.H. Hitchcock, H. Gecol, C. Evrensel, G. Korol, Development and characterization of hydrocarbon polyol polyurethane and silicone magnetorheological polymeric gels, Journal of applied polymer science 92(2) (2004) 1176-1182.

[27] T. Mitsumata, S. Ohori, Magnetic polyurethane elastomers with wide range modulation of elasticity, Polymer Chemistry 2(5) (2011) 1063-1067.

[28] J. Wu, X. Gong, Y. Fan, H. Xia, Physically crosslinked poly (vinyl alcohol) hydrogels with magnetic field controlled modulus, Soft Matter 7(13) (2011) 6205-6212.

[29] Y. Xu, X. Gong, S. Xuan, Soft magnetorheological polymer gels with controllable rheological properties, Smart Materials and Structures 22(7) (2013).

[30] M.-J. Wang, Effect of polymer-filler and filler-filler interactions on dynamic properties of filled vulcanizates, Rubber chemistry and technology 71(3) (1998) 520-589.

[31] J. Mewis, N.J. Wagner, Thixotropy, Advances in Colloid and Interface Science 147 (2009) 214-227.

[32] A.P. Gast, C.F. Zukoski, Electrorheological fluids as colloidal suspensions, Advances in Colloid and Interface science 30 (1989) 153-202.

[33] T.C. Halsey, Electrorheological fluids, Science 258(5083) (1992) 761-766.

[34] W.L. Benard, H. Kahn, A.H. Heuer, M.A. Huff, Thin-film shape-memory alloy actuated micropumps, Journal of Microelectromechanical systems 7(2) (1998) 245-251.

[35] J.D. Busch, A.D. Johnson, Shape-memory alloy micro-actuator, Google Patents, 1991.

[36] M.R. Jolly, J.W. Bender, J.D. Carlson, Properties and applications of commercial magnetorheological fluids, Smart structures and materials 1998: passive damping and isolation, International Society for Optics and Photonics, 1998, pp. 262-275.

[37] O. Ashour, C.A. Rogers, W. Kordonsky, Magnetorheological fluids: materials, characterization, and devices, Journal of intelligent material systems and structures 7(2) (1996) 123-130.

[38] W.M. Winslow, Induced fibration of suspensions, Journal of applied physics 20(12) (1949) 1137-1140.

[39] J.R. Lloyd, M.O. Hayesmichel, C.J. Radcliffe, Internal organizational measurement for control of magnetorheological fluid properties, (2007).

[40] H. Janocha, Adaptronics and smart structures, Springer1999.

[41] F.F. Fang, J.H. Kim, H.J. Choi, Synthesis of core–shell structured PS/Fe3O4 microbeads and their magnetorheology, Polymer 50(10) (2009) 2290-2293.

[42] W. Jiang, Y. Zhang, S. Xuan, C. Guo, X. Gong, Dimorphic magnetorheological fluid with improved rheological properties, Journal of Magnetism and Magnetic Materials 323(24) (2011) 3246-3250.

[43] M.S. Cho, S.T. Lim, I.B. Jang, H.J. Choi, M.S. Jhon, Encapsulation of spherical iron-particle with PMMA and its magnetorheological particles, IEEE Transactions on magnetics 40(4) (2004) 3036-3038.

[44] N. Wereley, A. Chaudhuri, J.-H. Yoo, S. John, S. Kotha, A. Suggs, R. Radhakrishnan, B. Love, T. Sudarshan, Bidisperse magnetorheological fluids using Fe particles at nanometer and micron scale, Journal of Intelligent Material Systems and Structures 17(5) (2006) 393-401.

[45] N. Rosenfeld, N.M. Wereley, R. Radakrishnan, T.S. Sudarshan, Behavior of magnetorheological fluids utilizing nanopowder iron, International Journal of Modern Physics B 16(17n18) (2002) 2392-2398.

[46] C. Burda, X. Chen, R. Narayanan, M.A. El-Sayed, Chemistry and properties of nanocrystals of different shapes, Chemical reviews 105(4) (2005) 1025-1102.

[47] R. Bell, J. Karli, A. Vavreck, D. Zimmerman, G. Ngatu, N. Wereley, Magnetorheology of submicron diameter iron microwires dispersed in silicone oil, Smart Materials and Structures 17(1) (2008) 015028.

[48] G. Ngatu, N. Wereley, J. Karli, R.C. Bell, Dimorphic magnetorheological fluids: exploiting partial substitution of microspheres by nanowires, Smart Materials and Structures 17(4) (2008) 045022.

[49] M.T. López-López, P. Kuzhir, G. Bossis, Magnetorheology of fiber suspensions. I. Experimental, Journal of Rheology 53(1) (2009) 115-126.

[50] S.T. Lim, M.S. Cho, I.B. Jang, H.J. Choi, Magnetorheological characterization of carbonyl iron based suspension stabilized by fumed silica, Journal of magnetism and magnetic materials 282 (2004) 170-173.

[51] J. Viota, J. De Vicente, J. Duran, A. Delgado, Stabilization of magnetorheological suspensions by polyacrylic acid polymers, Journal of colloid and interface science 284(2) (2005) 527-541.

[52] M.J. Hato, H.J. Choi, H.H. Sim, B.O. Park, S.S. Ray, Magnetic carbonyl iron suspension with organoclay additive and its magnetorheological properties, Colloids and Surfaces A: Physicochemical and Engineering Aspects 377(1-3) (2011) 103-109.

[53] T. Shiga, A. Okada, T. Kurauchi, Electroviscoelastic effect of polymer blends consisting of silicone elastomer and semiconducting polymer particles, Macromolecules 26(25) (1993) 6958-6963.

[54] S. Li, Y. Liang, Y. Li, J. Li, Y. Zhou, Investigation of dynamic properties of isotropic and anisotropic magnetorheological elastomers with a hybrid magnet shear test rig, Smart Materials and Structures 29(11) (2020) 114001.

[55] W.H. Li, Y. Zhou, T.F. Tian, Viscoelastic properties of MR elastomers under harmonic loading, Rheologica Acta 49(7) (2010) 733-740.

[56] J.M. Ginder, M.E. Nichols, L.D. Elie, J.L. Tardiff, Magnetorheological elastomers: properties and applications, Smart Structures and Materials 1999: Smart Materials Technologies, International Society for Optics and Photonics, 1999, pp. 131-138.

[57] G. Zhou, J. Li, Dynamic behavior of a magnetorheological elastomer under uniaxial deformation: I. Experiment, Smart Materials and Structures 12(6) (2003) 859.

[58] Y. Li, J. Li, W. Li, H. Du, A state-of-the-art review on magnetorheological elastomer devices, Smart materials and structures 23(12) (2014) 123001.

[59] Y. Li, J. Li, T. Tian, W. Li, A highly adjustable magnetorheological elastomer base isolator for applications of real-time adaptive control, Smart Materials and Structures 22(9) (2013) 095020.

[60] M. Kallio, T. Lindroos, S. Aalto, E. Järvinen, T. Kärnä, T. Meinander, Dynamic compression testing of a tunable spring element consisting of a magnetorheological elastomer, Smart Materials and Structures 16(2) (2007) 506.

[61] S. Kashima, F. Miyasaka, K. Hirata, Novel soft actuator using magnetorheological elastomer, IEEE Transactions on magnetics 48(4) (2012) 1649-1652.

[62] T. Kikuchi, I. Abe, T. Nagata, A. Yamaguchi, T. Takano, Twin-driven actuator with multi-layered disc magnetorheological fluid clutches for haptics, Journal of Intelligent Material Systems and Structures (2020) 1045389X20943958.

[63] A. Milecki, M. Hauke, Application of magnetorheological fluid in industrial shock absorbers, Mechanical Systems and Signal Processing 28 (2012) 528-541.

[64] J. Wang, G. Meng, Magnetorheological fluid devices: principles, characteristics and applications in mechanical engineering, Proceedings of the Institution of Mechanical Engineers, Part L: Journal of Materials: Design and Applications 215(3) (2001) 165-174.

[65] B. Wei, X. Gong, W. Jiang, L. Qin, Y. Fan, Study on the properties of magnetorheological gel based on polyurethane, Journal of Applied Polymer Science 118(5) (2010) 2765-2771.

[66] A. Tiraferri, K.L. Chen, R. Sethi, M. Elimelech, Reduced aggregation and sedimentation of zero-valent iron nanoparticles in the presence of guar gum, Journal of Colloid and Interface Science 324(1-2) (2008) 71-79.

[67] X. Gong, Y. Xu, S. Xuan, C. Guo, L. Zong, W. Jiang, The investigation on the nonlinearity of plasticine-like magnetorheological material under oscillatory shear rheometry, Journal of Rheology 56(6) (2012) 1375-1391.

[68] Y. Xu, X. Gong, S. Xuan, W. Zhang, Y. Fan, A high-performance magnetorheological material: preparation, characterization and magnetic-mechanic coupling properties, Soft Matter 7(11) (2011) 5246-5254.

[69] H. An, S.J. Picken, E. Mendes, Enhanced hardening of soft self-assembled copolymer gels under homogeneous magnetic fields, Soft Matter 6(18) (2010).

[70] M. Yu, B. Ju, J. Fu, S. Liu, S.-B. Choi, Magnetoresistance Characteristics of Magnetorheological Gel under a Magnetic Field, Industrial & Engineering Chemistry Research 53(12) (2014) 4704-4710.

[71] A.K. Bastola, M. Hossain, A review on magneto-mechanical characterizations of magnetorheological elastomers, Composites Part B: Engineering 200 (2020).

[72] G. Schubert, P. Harrison, Equi-biaxial tension tests on magneto-rheological elastomers, Smart Materials and Structures 25(1) (2015) 015015.

[73] G. Stepanov, S. Abramchuk, D. Grishin, L. Nikitin, E.Y. Kramarenko, A. Khokhlov, Effect of a homogeneous magnetic field on the viscoelastic behavior of magnetic elastomers, Polymer 48(2) (2007) 488-495.

[74] M. Kallio, The elastic and damping properties of magnetorheological elastomers, VTT Espoo, Finland2005.

[75] H. Laun, C. Gabriel, C. Kieburg, Twin gap magnetorheometer using ferromagnetic steel plates—performance and validation, Journal of Rheology 54(2) (2010) 327-354.

[76] C. Gabriel, C. Kieburg, H.M. Laun, Clutch and brake related testing of magnetorheological fluids using the BASF twin gap magnetocell, Applied Rheology 20(4) (2010).

[77] F.F. Fang, H.J. Choi, Y. Seo, Sequential coating of magnetic carbonyliron particles with polystyrene and multiwalled carbon nanotubes and its effect on their magnetorheology, ACS applied materials & interfaces 2(1) (2010) 54-60.

[78] B.L. Walter, J.-P. Pelteret, J. Kaschta, D.W. Schubert, P. Steinmann, Preparation of magnetorheological elastomers and their slip-free characterization by means of parallel-plate rotational rheometry, Smart Materials and Structures 26(8) (2017) 085004.

[79] W. Li, M. Nakano, Fabrication and characterization of PDMS based magnetorheological elastomers, Smart materials and structures 22(5) (2013) 055035.

[80] A. Dargahi, S. Rakheja, R. Sedaghati, Development of a field dependent Prandtl-Ishlinskii model for magnetorheological elastomers, Materials & Design 166 (2019).

[81] M. Sedlacik, V. Pavlinek, R. Vyroubal, P. Peer, P. Filip, A dimorphic magnetorheological fluid with improved oxidation and chemical stability under oscillatory shear, Smart Materials and Structures 22(3) (2013).

[82] P. Yang, M. Yu, J. Fu, H. Luo, Rheological properties of dimorphic magnetorheological gels mixed dendritic carbonyl iron powder, Journal of Intelligent Material Systems and Structures 29(1) (2017) 12-23.

[83] X.-X. Bai, P. Chen, On the Hysteresis Mechanism of Magnetorheological Fluids, Frontiers in Materials 6 (2019).

[84] J. De Vicente, D.J. Klingenberg, R. Hidalgo-Alvarez, Magnetorheological fluids: a review, Soft matter 7(8) (2011) 3701-3710.

[85] R. Bonnecaze, J. Brady, Dynamic simulation of an electrorheological fluid, The Journal of chemical physics 96(3) (1992) 2183-2202.

[86] D. Klingenberg, F. van Swol, C. Zukoski, The small shear rate response of electrorheological suspensions. II. Extension beyond the point–dipole limit, The Journal of chemical physics 94(9) (1991) 6170-6178.

[87] R. Christensen, Theory of viscoelasticity: an introduction, Elsevier2012.

[88] L. Chen, S. Jerrams, A rheological model of the dynamic behavior of magnetorheological elastomers, Journal of Applied Physics 110(1) (2011) 013513.

[89] B. Spencer Jr, S. Dyke, M. Sain, J. Carlson, Phenomenological model for magnetorheological dampers, Journal of engineering mechanics 123(3) (1997) 230-238.

[90] Y. Yu, Y. Li, J. Li, Parameter identification and sensitivity analysis of an improved LuGre friction model for magnetorheological elastomer base isolator, Meccanica 50(11) (2015) 2691-2707.

[91] M. Behrooz, X. Wang, F. Gordaninejad, Performance of a new magnetorheological elastomer isolation system, Smart Materials and Structures 23(4) (2014) 045014.

[92] X. Gu, Y. Yu, Y. Li, J. Li, M. Askari, B. Samali, Experimental study of semi-active magnetorheological elastomer base isolation system using optimal neuro fuzzy logic control, Mechanical Systems and Signal Processing 119 (2019) 380-398.

[93] X. Lu, X. Qiao, H. Watanabe, X. Gong, T. Yang, W. Li, K. Sun, M. Li, K. Yang, H. Xie, Mechanical and structural investigation of isotropic and anisotropic thermoplastic magnetorheological elastomer composites based on poly (styrene-b-ethylene-co-butylene-b-styrene)(SEBS), Rheologica acta 51(1) (2012) 37-50.

[94] T. Sun, X. Gong, W. Jiang, J. Li, Z. Xu, W. Li, Study on the damping properties of magnetorheological elastomers based on cis-polybutadiene rubber, Polymer Testing 27(4) (2008) 520-526.

[95] B. Ju, M. Yu, J. Fu, Q. Yang, X. Liu, X. Zheng, A novel porous magnetorheological elastomer: preparation and evaluation, Smart Materials and Structures 21(3) (2012) 035001.

[96] F. Imaduddin, Y. Li, S.A. Mazlan, J. Sutrisno, T. Koga, I. Yahya, S.-B. Choi, A new class of magnetorheological elastomers based on waste tire rubber and the characterization of their properties, Smart Materials and Structures 25(11) (2016) 115002.

[97] X. Gong, X. Zhang, P. Zhang, Fabrication and characterization of isotropic magnetorheological elastomers, Polymer testing 24(5) (2005) 669-676.

[98] P. Zając, J. Kaleta, D. Lewandowski, A. Gasperowicz, Isotropic magnetorheological elastomers with thermoplastic matrices: structure, damping properties and testing, Smart Materials and Structures 19(4) (2010) 045014.

[99] J. Yang, S. Sun, H. Du, W. Li, G. Alici, H. Deng, A novel magnetorheological elastomer isolator with negative changing stiffness for vibration reduction, Smart materials and structures 23(10) (2014) 105023.

[100] S. Sun, H. Deng, J. Yang, W. Li, H. Du, G. Alici, M. Nakano, An adaptive tuned vibration absorber based on multilayered MR elastomers, Smart materials and structures 24(4) (2015) 045045.

[101] Y. Yu, Y. Li, J. Li, X. Gu, A hysteresis model for dynamic behaviour of magnetorheological elastomer base isolator, Smart Materials and Structures 25(5) (2016) 055029.

[102] J. Ginder, S. Clark, W. Schlotter, M. Nichols, Magnetostrictive phenomena in magnetorheological elastomers, International Journal of Modern Physics B 16(17n18) (2002) 2412-2418.

[103] H.-J. Jung, S.-H. Eem, D.-D. Jang, J.-H. Koo, Seismic performance analysis of a smart base-isolation system considering dynamics of MR elastomers, Journal of intelligent material systems and structures 22(13) (2011) 1439-1450.

[104] J.M. Ginder, W.F. Schlotter, M.E. Nichols, Magnetorheological elastomers in tunable vibration absorbers, Smart structures and materials 2001: damping and isolation, International Society for Optics and Photonics, 2001, pp. 103-110.

[105] Z. Xu, X. Gong, G. Liao, X. Chen, An active-damping-compensated magnetorheological elastomer adaptive tuned vibration absorber, Journal of Intelligent Material Systems and Structures 21(10) (2010) 1039-1047.

[106] G. Yun, S.-Y. Tang, S. Sun, D. Yuan, Q. Zhao, L. Deng, S. Yan, H. Du, M.D. Dickey, W. Li, Liquid metal-filled magnetorheological elastomer with positive piezoconductivity, Nature communications 10(1) (2019) 1-9.

[107] S. Qi, H. Guo, J. Chen, J. Fu, C. Hu, M. Yu, Z.L. Wang, Magnetorheological elastomers enabled high-sensitive self-powered tribo-sensor for magnetic field detection, Nanoscale 10(10) (2018) 4745-4752.

[108] F. Thorsteinsson, I. Gudmundsson, C. Lecomte, Prosthetic and orthotic devices having magnetorheological elastomer spring with controllable stiffness, Google Patents, 2015.

[109] T. Yang, D. Xie, Z. Li, H. Zhu, Recent advances in wearable tactile sensors: Materials, sensing mechanisms, and device performance, Materials Science and Engineering: R: Reports 115 (2017) 1-37.

[110] Y. Li, J. Li, Overview of the development of smart base isolation system featuring magnetorheological elastomer, Smart Structures and Systems 24(1) (2019) 37-52.

[111] X. Gu, J. Li, Y. Li, Experimental realisation of the real-time controlled smart magnetorheological elastomer seismic isolation system with shake table, Structural Control and Health Monitoring 27(1) (2020) e2476.

[112] Z.-W. Xing, M. Yu, J. Fu, Y. Wang, L.-J. Zhao, A laminated magnetorheological elastomer bearing prototype for seismic mitigation of bridge superstructures, Journal of Intelligent Material Systems and Structures 26(14) (2015) 1818-1825.

[113] M. Yu, L. Zhao, J. Fu, M. Zhu, Thermal effects on the laminated magnetorheological elastomer isolator, Smart Materials and Structures 25(11) (2016) 115039.

[114] G. Yang, B. Spencer Jr, J. Carlson, M. Sain, Large-scale MR fluid dampers: modeling and dynamic performance considerations, Engineering structures 24(3) (2002) 309-323.

[115] C. Chen, W.-H. Liao, A self-sensing magnetorheological damper with power generation, Smart Materials and Structures 21(2) (2012) 025014.

[116] A. Milecki, Investigation and control of magneto–rheological fluid dampers, International journal of machine tools and manufacture 41(3) (2001) 379-391.

[117] J. Zheng, Z. Li, J. Koo, J. Wang, Magnetic circuit design and multiphysics analysis of a novel MR damper for applications under high velocity, Advances in Mechanical Engineering 6 (2014) 402501.

[118] X. Zhu, X. Jing, L. Cheng, Magnetorheological fluid dampers: a review on structure design and analysis, Journal of intelligent material systems and structures 23(8) (2012) 839-873.

[119] B. Yang, J. Luo, L. Dong, Magnetic circuit FEM analysis and optimum design for MR damper, International Journal of Applied Electromagnetics and Mechanics 33(1-2) (2010) 207-216.

[120] H. Gavin, J. Hoagg, M. Dobossy, Optimal design of MR dampers, Proceedings of US-Japan workshop on smart structures for improved seismic performance in urban regions, 2001, pp. 225-236.

[121] N. Takesue, J. Furusho, Y. Kiyota, Fast response MR-fluid actuator, JSME International Journal Series C Mechanical Systems, Machine Elements and Manufacturing 47(3) (2004) 783-791.

[122] J. An, D.-S. Kwon, Modeling of a magnetorheological actuator including magnetic hysteresis, Journal of Intelligent Material Systems and Structures 14(9) (2003) 541-550.

[123] R. Boelter, H. Janocha, Design rules for MR fluid actuators in different working modes, Smart Structures and Materials 1997: Passive Damping and Isolation, International Society for Optics and Photonics, 1997, pp. 148-159.

[124] J.-H. Yoo, N.M. Wereley, Design of a high-efficiency magnetorheological valve, Journal of Intelligent Material Systems and Structures 13(10) (2002) 679-685.

[125] A. Grunwald, A.-G. Olabi, Design of magneto-rheological (MR) valve, Sensors and Actuators A: Physical 148(1) (2008) 211-223.

[126] N. Guo, H. Du, W. Li, Finite element analysis and simulation evaluation of a magnetorheological valve, The international journal of advanced manufacturing technology 21(6) (2003) 438-445.

[127] Q.-H. Nguyen, Y.-M. Han, S.-B. Choi, N.M. Wereley, Geometry optimization of MR valves constrained in a specific volume using the finite element method, Smart Materials and Structures 16(6) (2007) 2242.

[128] Q. Wang, X. Dong, L. Li, J. Ou, Mechanical modeling for magnetorheological elastomer isolators based on constitutive equations and electromagnetic analysis, Smart Materials and Structures 27(6) (2018) 065017.

[129] H. Böse, R. Rabindranath, J. Ehrlich, Soft magnetorheological elastomers as new actuators for valves, Journal of Intelligent Material Systems and Structures 23(9) (2012) 989-994.

[130] C. Yang, J. Fu, M. Yu, X. Zheng, B. Ju, A new magnetorheological elastomer isolator in shear–compression mixed mode, Journal of Intelligent Material Systems and Structures 26(10) (2015) 1290-1300.

[131] H.C. Roters, Electromagnetic devices, Wiley & Sons (1941).

[132] W. Wright, M. McCaig, Permanent Magnets, Oxford University Press for the Design Council, the British Standards Institution (1977).

[133] S.U. Khayam, M. Usman, M.A. Umer, A. Rafique, Development and characterization of a novel hybrid magnetorheological elastomer incorporating micro and nano size iron fillers, Materials & Design (2020) 108748.

[134] A. Bastola, V. Hoang, L. Li, A novel hybrid magnetorheological elastomer developed by 3D printing, Materials & Design 114 (2017) 391-397.

[135] L. Zhang, Z. Huang, H. Shao, Y. Li, H. Zheng, Effects of γ-Fe2O3 on γ-Fe2O3/Fe3O4 composite magnetic fluid by low-temperature low-vacuum oxidation method, Materials & Design 105 (2016) 234-239.

[136] T. Hu, S. Xuan, L. Ding, X. Gong, Stretchable and magneto-sensitive strain sensor based on silver nanowire-polyurethane sponge enhanced magnetorheological elastomer, Materials & Design 156 (2018) 528-537.

[137] T. Mitsumata, N. Abe, Magnetic-field sensitive gels with wide modulation of dynamic modulus, Chemistry letters 38(9) (2009) 922-923.

[138] H.-N. An, S.J. Picken, E. Mendes, Direct observation of particle rearrangement during cyclic stress hardening of magnetorheological gels, Soft Matter 8(48) (2012) 11995-12001.

[139] B. Hu, A. Fuchs, S. Huseyin, F. Gordaninejad, C. Evrensel, Supramolecular magnetorheological polymer gels, Journal of applied polymer science 100(3) (2006) 2464-2479.

[140] T. Mitsumata, K. Sakai, J.-i. Takimoto, Giant reduction in dynamic modulus of κ-carrageenan magnetic gels, The Journal of Physical Chemistry B 110(41) (2006) 20217-20223.

[141] B. Liu, C. Du, G. Yu, Y. Fu, Shear thickening effect of a multifunctional magnetorheological gel: the influence of cross-linked bonds and solid particles, Smart Materials and Structures 29(1) (2019) 015004.

[142] H.-N. An, B. Sun, S.J. Picken, E. Mendes, Long time response of soft magnetorheological gels, The Journal of Physical Chemistry B 116(15) (2012) 4702-4711.

[143] H. An, S.J. Picken, E. Mendes, Nonlinear rheological study of magneto responsive soft gels, Polymer 53(19) (2012) 4164-4170.

[144] F.D. Goncalves, J.-H. Koo, M. Ahmadian, A review of the state of the art in magnetorheological fluid technologies--Part I: MR fluid and MR fluid models, The Shock and Vibration Digest 38(3) (2006) 203-220.

[145] F. Gandhi, W.A. Bullough, On the phenomenological modeling of electrorheological and magnetorheological fluid preyield behavior, Journal of Intelligent Material Systems and Structures 16(3) (2005) 237-248.

[146] L. Davis, Model of magnetorheological elastomers, Journal of Applied Physics 85(6) (1999) 3348-3351.

[147] X. Zhang, W. Li, X. Gong, An effective permeability model to predict field-dependent modulus of magnetorheological elastomers, Communications in Nonlinear Science and Numerical Simulation 13(9) (2008) 1910-1916.

[148] Z. Guo, Y. Chen, Q. Wan, H. Li, X. Shi, S. Tang, X. Peng, A hyperelastic constitutive model for chain-structured particle reinforced neo-Hookean composites, Materials & Design 95 (2016) 580-590.

[149] Y. Yu, J. Li, Y. Li, S. Li, H. Li, W. Wang, Comparative Investigation of Phenomenological Modeling for Hysteresis Responses of Magnetorheological Elastomer Devices, Int J Mol Sci 20(13) (2019).

[150] G. Yang, B.F. Spencer Jr, H.-J. Jung, J.D. Carlson, Dynamic modeling of large-scale magnetorheological damper systems for civil engineering applications, Journal of Engineering Mechanics 130(9) (2004) 1107-1114.

[151] X. Xie, L. Xu, Z. Li, Modeling of Magnetorheological Self-Centering Brace, Journal of Engineering Mechanics 146(1) (2020) 04019112.

[152] H. Wang, Y. Li, G. Zhang, J. Wang, Effect of temperature on rheological properties of lithium-based magnetorheological grease, Smart Materials and Structures 28(3) (2019) 035002.

[153] H. Sahin, X. Wang, F. Gordaninejad, A new model for yield stress of magnetorheological greases/gels under combined effects of magnetic field and temperature, Active and Passive Smart Structures and Integrated Systems 2009, International Society for Optics and Photonics, 2009, p. 72881E.

[154] G. Zhang, Y. Li, H. Wang, J. Wang, Rheological Properties of Polyurethane-Based Magnetorheological Gels, Frontiers in Materials 6 (2019) 56.

[155] R.H. Ewoldt, G.H. McKinley, On secondary loops in LAOS via self-intersection of Lissajous–Bowditch curves, Rheologica Acta 49(2) (2010) 213-219.

[156] K. Hyun, J.G. Nam, M. Wilhelm, K.H. Ahn, S.J. Lee, Nonlinear response of complex fluids under LAOS (large amplitude oscillatory shear) flow, Korea-Australia Rheology Journal 15(2) (2003) 97-105.

[157] R.H. Ewoldt, A. Hosoi, G.H. McKinley, New measures for characterizing nonlinear viscoelasticity in large amplitude oscillatory shear, Journal of Rheology 52(6) (2008) 1427-1458.

[158] L. Zhou, L.P. Cook, G.H. McKinley, Probing shear-banding transitions of the VCM model for entangled wormlike micellar solutions using large amplitude oscillatory shear (LAOS) deformations, Journal of non-newtonian fluid mechanics 165(21-22) (2010) 1462-1472.

[159] H.G. Sim, K.H. Ahn, S.J. Lee, Large amplitude oscillatory shear behavior of complex fluids investigated by a network model: a guideline for classification, Journal of Non-Newtonian Fluid Mechanics 112(2-3) (2003) 237-250.

[160] F. Renou, J. Stellbrink, G. Petekidis, Yielding processes in a colloidal glass of soft star-like micelles under large amplitude oscillatory shear (LAOS), Journal of Rheology 54(6) (2010) 1219-1242.

[161] T. Divoux, C. Barentin, S. Manneville, Stress overshoot in a simple yield stress fluid: An extensive study combining rheology and velocimetry, Soft Matter 7(19) (2011) 9335-9349.

[162] L. Wang, H. Kamath, Modelling hysteretic behaviour in magnetorheological fluids and dampers using phase-transition theory, Smart materials and structures 15(6) (2006) 1725.

[163] J. Duchon, Splines minimizing rotation-invariant semi-norms in Sobolev spaces, Constructive theory of functions of several variables, Springer1977, pp. 85-100.

[164] J.W. Chong, Y. Kim, K.H. Chon, Nonlinear multiclass support vector machine–based health monitoring system for buildings employing magnetorheological dampers, Journal of Intelligent Material Systems and Structures 25(12) (2014) 1456-1468.

[165] J. Xiong, S.-Q. Shi, T.-Y. Zhang, A machine-learning approach to predicting and understanding the properties of amorphous metallic alloys, Materials & Design 187 (2020) 108378.

[166] Y. Zhang, G.S. Hong, D. Ye, K. Zhu, J.Y. Fuh, Extraction and evaluation of melt pool, plume and spatter information for powder-bed fusion AM process monitoring, Materials & Design 156 (2018) 458-469.

[167] G. Konstantopoulos, E.P. Koumoulos, C.A. Charitidis, Classification of mechanism of reinforcement in the fiber-matrix interface: Application of Machine Learning on nanoindentation data, Materials & Design (2020) 108705.

[168] T. Mitsumata, N. Abe, Giant and reversible magnetorheology of carrageenan/iron oxide magnetic gels, Smart materials and structures 20(12) (2011) 124003.

[169] S. Li, T. Tian, H. Wang, Y. Li, J. Li, Y. Zhou, J. Wu, Development of a four-parameter phenomenological model for the nonlinear viscoelastic behaviour of magnetorheological gels, Materials & Design 194 (2020) 108935.

[170] H.A. Barnes, Thixotropy—a review, Journal of Non-Newtonian fluid mechanics 70(1-2) (1997) 1-33.

[171] N. Roussel, Steady and transient flow behaviour of fresh cement pastes, Cement and concrete research 35(9) (2005) 1656-1664.

[172] P. Billberg, Development of SCC static yield stress at rest and its effect on thelateral form pressure, SCC 2005, combining the second North American conference on the design and use of self-consolidating concrete and the fourth international RILEM symposium on self-compacting concrete, 2005, pp. 583-589.

[173] Y. Wang, W. Xie, D. Wu, Rheological properties of magnetorheological suspensions stabilized with nanocelluloses, Carbohydrate Polymers 231 (2020) 115776.

[174] Z. Li, D. Li, Y. Chen, H. Cui, Study of the thixotropic behaviors of ferrofluids, Soft Matter 14(19) (2018) 3858-3869.

[175] D. Wang, Z. Tian, Q. Meng, Y. Hou, Development of a novel two-layer multiplate magnetorheological clutch for high-power applications, Smart materials and structures 22(8) (2013) 085018.

[176] M. Yu, S.B. Choi, X. Dong, C. Liao, Fuzzy neural network control for vehicle stability utilizing magnetorheological suspension system, Journal of Intelligent Material Systems and Structures 20(4) (2009) 457-466.

[177] P. Coussot, Rheometry of pastes, suspensions, and granular materials: applications in industry and environment, John Wiley & Sons2005.

[178] A. Berker, W. Van Arsdale, Phenomenological models of viscoplastic, thixotropic, and granular materials, Rheologica acta 31(2) (1992) 119-138.

[179] R. De Rooij, A. Potanin, D. Van den Ende, J. Mellema, Steady shear viscosity of weakly aggregating polystyrene latex dispersions, The Journal of chemical physics 99(11) (1993) 9213-9223.

[180] A. Potanin, R. De Rooij, D. Van den Ende, J. Mellema, Microrheological modeling of weakly aggregated dispersions, The Journal of chemical physics 102(14) (1995) 5845-5853.

[181] P. Coussot, J. Raynaud, F. Bertrand, P. Moucheront, J. Guilbaud, H. Huynh, S. Jarny, D. Lesueur, Coexistence of liquid and solid phases in flowing soft-glassy materials, Physical review letters 88(21) (2002) 218301.

[182] C.F. Goodeve, A general theory of thixotropy and viscosity, Transactions of the Faraday Society 35 (1939) 342-358.

[183] P. Coussot, Q.D. Nguyen, H. Huynh, D. Bonn, Avalanche behavior in yield stress fluids, Physical review letters 88(17) (2002) 175501.

[184] N. Roussel, R. Le Roy, P. Coussot, Test of a thixotropy model by comparison with local and macroscopic flow properties, J. Non-Newton. Fluid Mech 117 (2004) 85-95.

[185] S. Jarny, N. Roussel, R. Le Roy, P. Coussot, Steady state and transient behaviour of fresh cement pastes: MRI velocity measurements and simulation, 2005.

[186] N. Roussel, A thixotropy model for fresh fluid concretes: theory, validation and applications, Cement and concrete research 36(10) (2006) 1797-1806.

[187] J.E. Wallevik, Rheology of particle suspensions: fresh concrete, mortar and cement paste with various types of lignosulfonates, Fakultet for ingeniørvitenskap og teknologi2003.

[188] H. Green, R. Weltmann, Analysis of thixotropy of pigment-vehicle suspensions-basic principles of the hysteresis loop, Industrial & Engineering Chemistry Analytical Edition 15(3) (1943) 201-206.

[189] Y.I. Dikansky, A. Ispiryan, S. Kunikin, Remanence magnetization of iron oxide particles with different size distribution, Journal of Physics: Conference Series, IOP Publishing, 2019, p. 012052.

Appendix A

Calculation for the elements in the improved MCM of the hybrid magnets MR elastomer isolator

$$l_{\text{air}} = height\ of\ airgap = 5\ \text{mm}$$

$$l_{\text{MRE}} = thickness\ of\ MRE = 1\ \text{mm}$$

$$l_{\text{Steel sheet}} = thickness\ of\ steel\ sheet = 1\ \text{mm}$$

$$l_{\text{Steel block}} = height\ of\ steel\ block = 37\ \text{mm}$$

$$l_{\text{Yoke}} = height\ of\ yoke = 110\ \text{mm}$$

$$l_{\text{PM}} = thickness\ of\ PM = 5\ \text{mm}$$

$$l_{\text{Steel plate}} = half\ of\ the\ plate\ thickness \times 2 + Average\ of inner\ and\ outer\ radius\ of\ yoke = 110\ \text{mm}$$

$$A_{\text{air}} = \pi(outer\ radius\ of\ yoke)^2 - \pi(inner\ radius\ of\ yoke)^2 = 12566.37\ \text{mm}^2$$

$$A_{\text{MRE}} = \pi(radius\ of\ MRE)^2 = 7853.98\ \text{mm}^2$$

$$A_{\text{Steel sheet}} = \pi(radius\ of\ steel\ sheet)^2 = 7853.98\ \text{mm}^2$$

$$A_{\text{Steel block}} = \pi(radius\ of\ steel\ block)^2 = 7853.98\ \text{mm}^2$$

$$A_{\text{Yoke}} = \pi(outer\ radius\ of\ yoke)^2 - \pi(inner\ radius\ of\ yoke)^2 = 12566.37\ \text{mm}^2$$

$$A_{\text{PM}} = \pi(radius\ of\ PM)^2 = 7853.98\ \text{mm}^2$$

$$A_{\text{Steel plate}} = (plate\ thickness) \times \pi(diameter\ of\ steel\ block + inner\ diameter\ of\ yoke)/2 = 4398.23\ \text{mm}^2$$

Appendix B

Reluctance of fringing path

	l (m)	A (m^2)	R (Aturns/Wb)
R_{air1}	6.57E-03	3.14E-04	1.66E+07
R_{air2}	1.29E-02	3.14E-04	3.25E+07
R_{air3}	1.91E-02	3.14E-04	4.84E+07
R_{air4}	2.54E-02	3.14E-04	6.43E+07
R_{air5}	3.17E-02	3.14E-04	8.02E+07
R_{air6}	3.80E-02	3.14E-04	9.62E+07
R_{air7}	4.43E-02	3.14E-04	1.12E+08
R_{air8}	5.06E-02	3.14E-04	1.28E+08
R_{air9}	5.68E-02	3.14E-04	1.44E+08

Appendix C

Results from FEA, MCM and MCMF (MCM considering fringing effect)

$i = 0$ A					
	FEA (T)	MCMF (T)	MCM (T)	MCMF error	MCM error
PM	0.63	0.53	0.49	15.7%	22.7%
S1	1.04	0.86	0.49	17.4%	53.0%
M1	0.58	0.51	0.49	10.8%	14.8%
S2	0.70	0.60	0.49	14.8%	30.4%
M2	0.56	0.50	0.49	9.3%	11.7%
S3	0.60	0.54	0.49	11.3%	19.0%
M3	0.54	0.50	0.49	8.1%	9.5%
S4	0.57	0.51	0.49	9.7%	13.6%
M4	0.53	0.49	0.49	7.2%	7.8%
S5	0.55	0.50	0.49	8.4%	10.3%
M5	0.52	0.49	0.49	6.4%	6.5%
S6	0.53	0.49	0.49	7.2%	7.9%
M6	0.52	0.49	0.49	5.9%	5.5%
S7	0.52	0.49	0.49	6.5%	6.4%
M7	0.51	0.49	0.49	5.4%	4.7%
S8	0.52	0.49	0.49	5.7%	5.2%
M8	0.51	0.49	0.49	5.1%	4.2%
S9	0.51	0.49	0.49	5.5%	4.6%
M9	0.51	0.48	0.49	4.9%	3.9%

i = 0.286 A					
	FEA (T)	MCMF (T)	MCM (T)	MCMF error	MCM error
PM	0.54	0.43	0.45	19.6%	16.2%
S1	1.02	0.89	0.45	13.0%	56.0%
M1	0.47	0.41	0.45	14.0%	5.2%
S2	0.66	0.55	0.45	16.3%	31.6%
M2	0.45	0.40	0.45	12.2%	0.5%
S3	0.53	0.46	0.45	12.9%	14.5%
M3	0.44	0.39	0.45	10.9%	2.9%
S4	0.48	0.42	0.45	12.1%	6.1%
M4	0.43	0.38	0.45	9.7%	5.6%
S5	0.45	0.40	0.45	10.8%	0.1%
M5	0.42	0.38	0.45	8.8%	7.8%
S6	0.43	0.39	0.45	9.9%	3.8%
M6	0.41	0.38	0.45	8.0%	9.6%
S7	0.42	0.38	0.45	8.7%	7.0%
M7	0.40	0.38	0.45	7.3%	11.1%
S8	0.41	0.38	0.45	7.8%	9.5%
M8	0.40	0.37	0.45	6.8%	12.3%
S9	0.40	0.38	0.45	7.1%	11.3%
M9	0.40	0.37	0.45	6.6%	13.1%

i = 0.571 A					
	FEA (T)	MCMF (T)	MCM (T)	MCMF error	MCM error
PM	0.43	0.33	0.35	23.1%	18.4%
S1	0.99	0.94	0.35	4.9%	64.6%
M1	0.36	0.30	0.35	16.8%	4.1%
S2	0.62	0.53	0.35	15.5%	43.8%
M2	0.34	0.29	0.35	14.3%	3.3%
S3	0.45	0.40	0.35	11.7%	22.8%
M3	0.32	0.28	0.35	12.6%	8.6%
S4	0.39	0.34	0.35	12.1%	10.6%
M4	0.31	0.28	0.35	11.0%	13.1%
S5	0.35	0.31	0.35	11.1%	1.0%
M5	0.30	0.27	0.35	9.6%	16.8%
S6	0.33	0.30	0.35	10.3%	6.1%
M6	0.29	0.27	0.35	8.4%	20.1%
S7	0.31	0.28	0.35	8.9%	12.2%
M7	0.28	0.26	0.35	7.4%	22.9%
S8	0.30	0.28	0.35	7.6%	17.3%
M8	0.28	0.26	0.35	6.5%	25.2%
S9	0.29	0.27	0.35	6.3%	21.6%
M9	0.28	0.26	0.35	5.9%	27.2%

i = 0.857 A					
	FEA (T)	MCMF (T)	MCM (T)	MCMF error	MCM error
PM	0.32	0.23	0.23	28.5%	27.9%
S1	1.03	1.01	0.23	1.9%	77.6%
M1	0.24	0.20	0.23	18.5%	5.5%
S2	0.67	0.53	0.23	21.0%	65.6%
M2	0.21	0.18	0.23	14.2%	7.4%
S3	0.41	0.37	0.23	9.0%	43.3%
M3	0.20	0.17	0.23	11.1%	17.6%
S4	0.31	0.29	0.23	7.0%	26.9%
M4	0.18	0.17	0.23	8.2%	26.7%
S5	0.27	0.25	0.23	6.5%	13.4%
M5	0.17	0.16	0.23	5.4%	35.2%
S6	0.23	0.22	0.23	4.7%	0.4%
M6	0.16	0.16	0.23	2.9%	42.8%
S7	0.21	0.20	0.23	3.8%	10.3%
M7	0.15	0.15	0.23	0.5%	50.1%
S8	0.19	0.19	0.23	0.0%	23.3%
M8	0.15	0.15	0.23	1.5%	56.6%
S9	0.17	0.18	0.23	3.7%	35.6%
M9	0.14	0.15	0.23	3.5%	62.9%

i = 1.143 A					
	FEA (T)	MCMF (T)	MCM (T)	MCMF error	MCM error
PM	0.20	0.13	0.09	37.0%	55.1%
S1	1.02	1.09	0.09	7.2%	91.1%
M1	0.12	0.09	0.09	24.4%	27.3%
S2	0.71	0.56	0.09	21.1%	87.2%
M2	0.09	0.08	0.09	12.3%	2.5%
S3	0.40	0.37	0.09	6.2%	77.4%
M3	0.07	0.07	0.09	0.9%	35.1%
S4	0.28	0.28	0.09	0.5%	67.8%
M4	0.05	0.06	0.09	13.7%	77.2%
S5	0.22	0.23	0.09	3.1%	58.8%
M5	0.04	0.05	0.09	34.1%	135.9%
S6	0.18	0.19	0.09	4.5%	49.9%
M6	0.03	0.05	0.09	65.1%	224.9%
S7	0.15	0.16	0.09	6.6%	40.3%
M7	0.02	0.04	0.09	119.2%	380.4%
S8	0.12	0.14	0.09	13.0%	27.6%
M8	0.01	0.04	0.09	227.2%	695.9%
S9	0.10	0.12	0.09	28.2%	7.4%
M9	0.00	0.03	0.09	572.5%	1712.5%

i = 1.357 A					
	FEA (T)	MCMF (T)	MCM (T)	MCMF error	MCM error
PM	0.11	0.05	0.00	55.7%	Not applicable
S1	1.04	1.16	0.00	11.4%	
M1	0.04	0.01	0.00	65.4%	
S2	0.75	0.59	0.00	21.2%	
M2	0.02	0.00	0.00	81.3%	
S3	0.42	0.40	0.00	5.4%	
M3	0.04	0.01	0.00	58.5%	
S4	0.30	0.30	0.00	1.4%	
M4	0.05	0.02	0.00	53.8%	
S5	0.24	0.24	0.00	2.3%	
M5	0.06	0.03	0.00	51.9%	
S6	0.20	0.21	0.00	1.1%	
M6	0.08	0.04	0.00	50.9%	
S7	0.18	0.18	0.00	2.4%	
M7	0.09	0.04	0.00	50.3%	
S8	0.17	0.16	0.00	3.3%	
M8	0.09	0.05	0.00	49.9%	
S9	0.15	0.15	0.00	1.5%	
M9	0.10	0.05	0.00	49.6%	

Appendix D

Measured hysteresis for MR gel and modelling results of the proposed model under excitation frequency=0.1 Hz

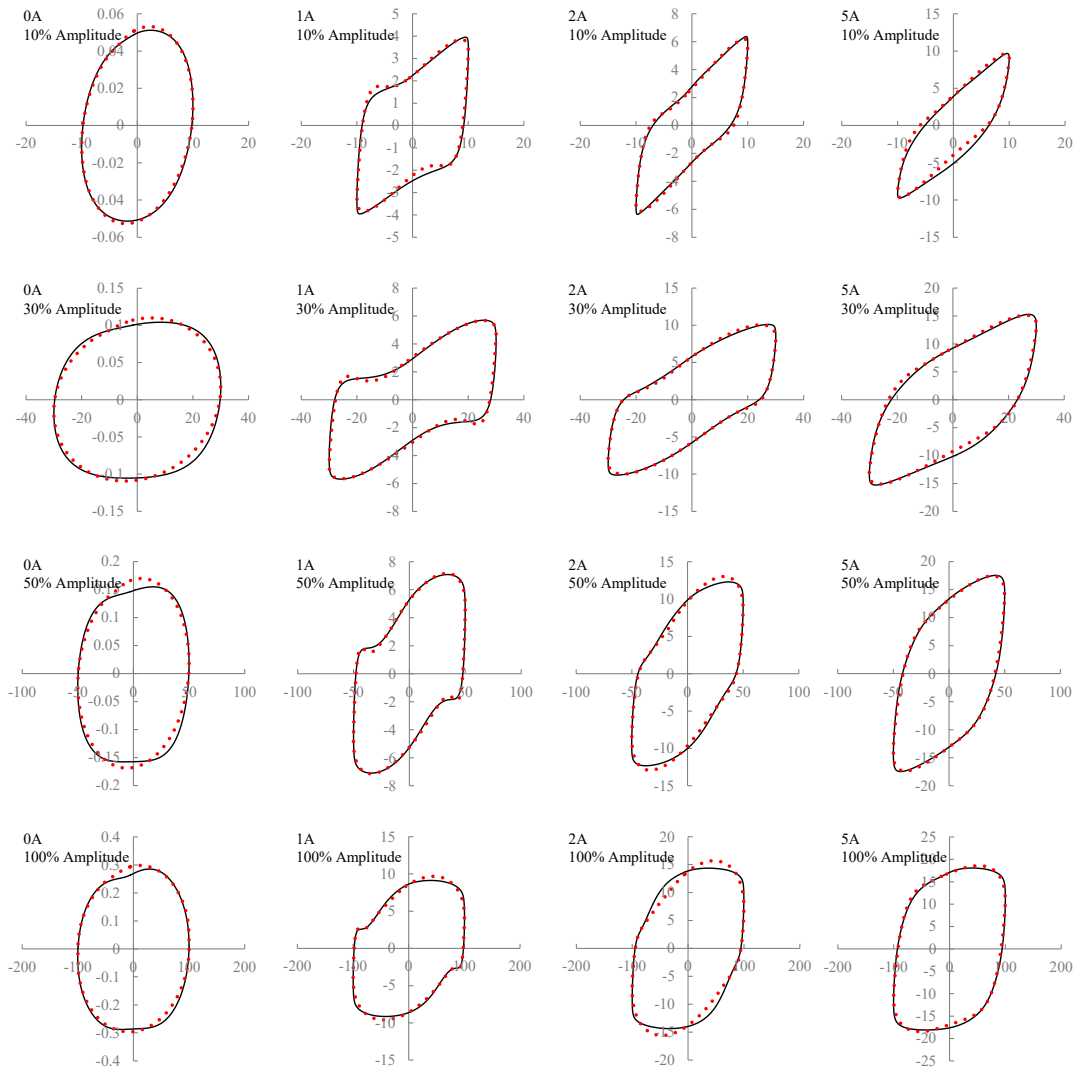

Note:

Horizontal axis: strain amplitude (%); vertical axis: shear stress (kPa); black solid line: experimental data; red dotted line: predicted results from the proposed model.

Measured hysteresis for MR gel and modelling results of the proposed model under excitation frequency=0.5 Hz

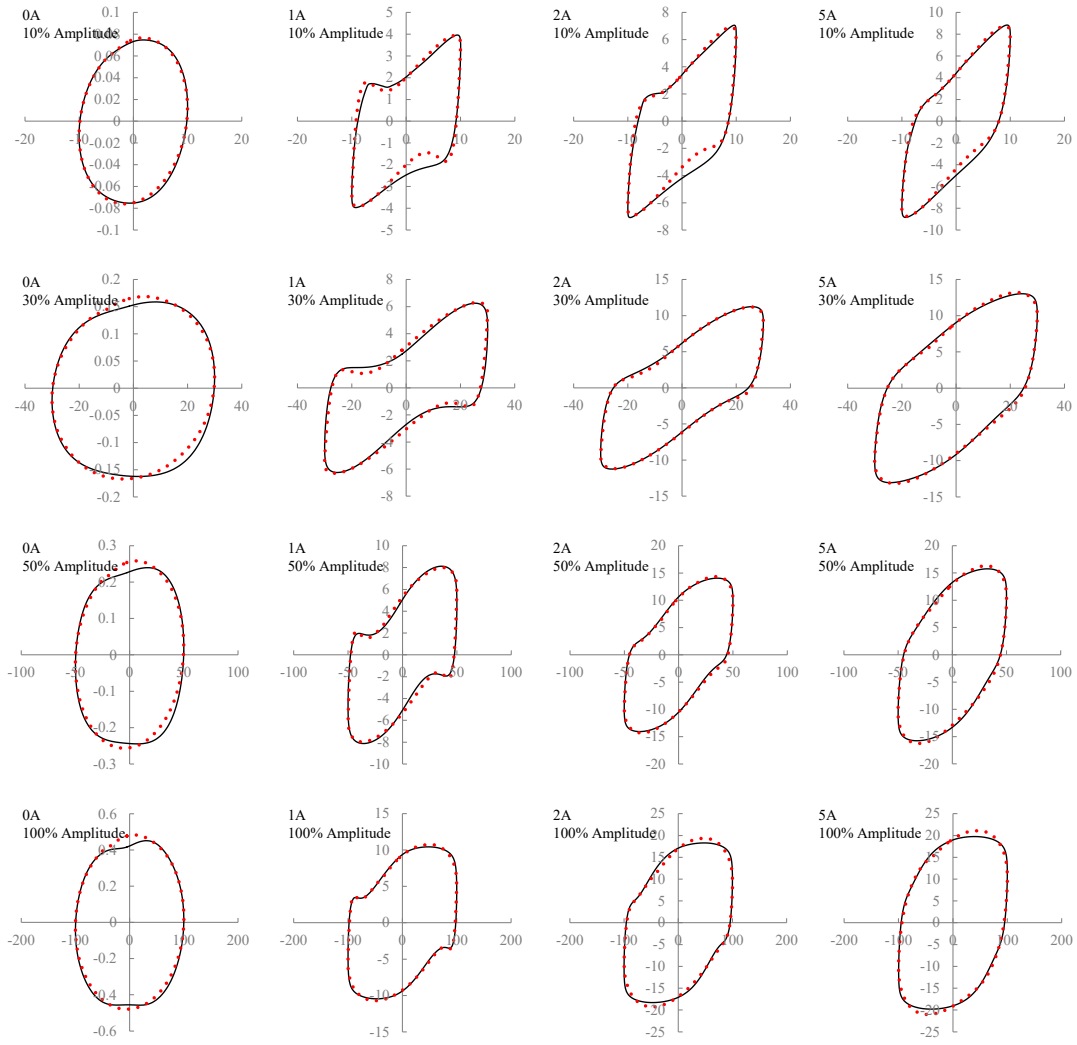

Note:

Horizontal axis: strain amplitude (%); vertical axis: shear stress (kPa); black solid line: experimental data; red dotted line: predicted results from the proposed model.

Measured hysteresis for MR gel and modelling results of the proposed model under excitation frequency=1 Hz

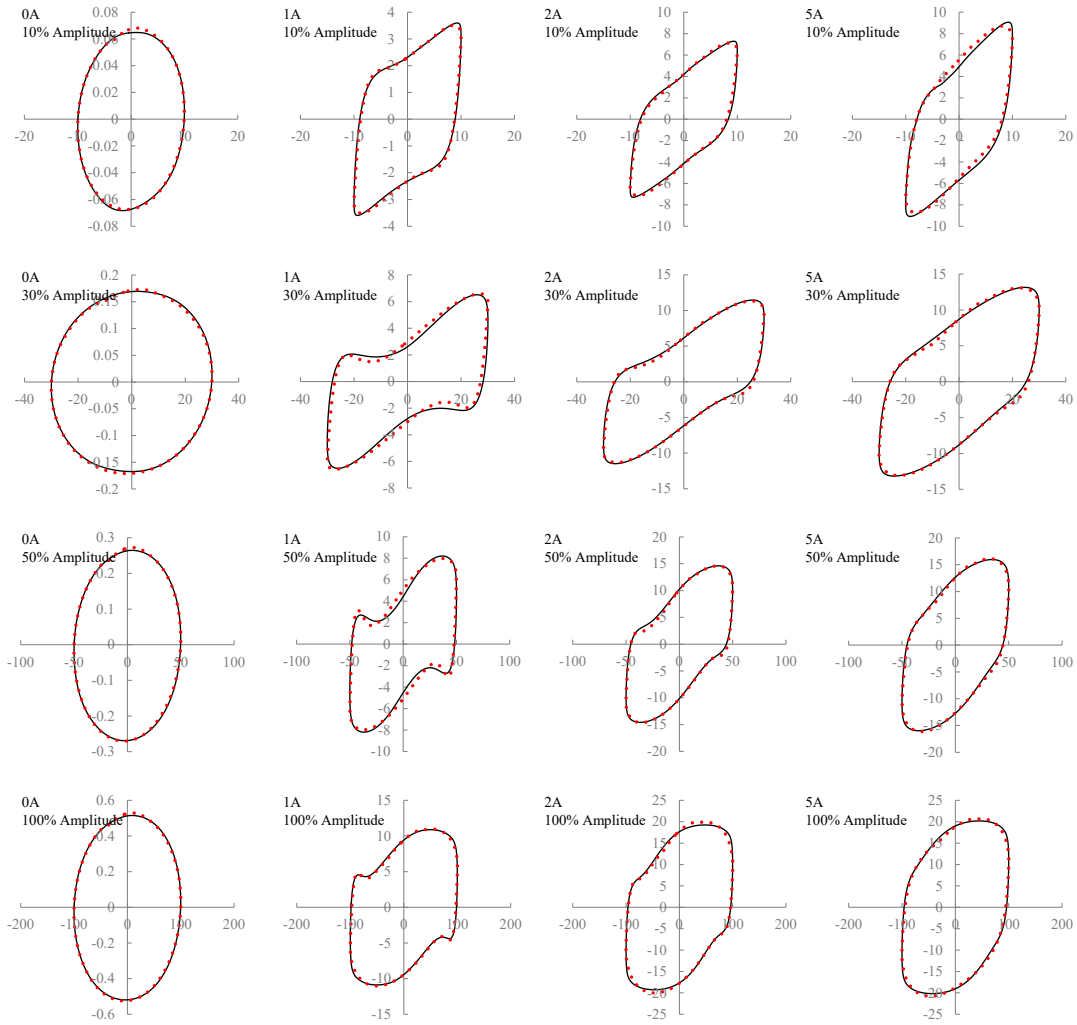

Note:

Horizontal axis: strain amplitude (%); vertical axis: shear stress (kPa); black solid line: experimental data; red dotted line: predicted results from the proposed model.

Measured hysteresis for MR gel and modelling results of the proposed model under excitation frequency=2 Hz

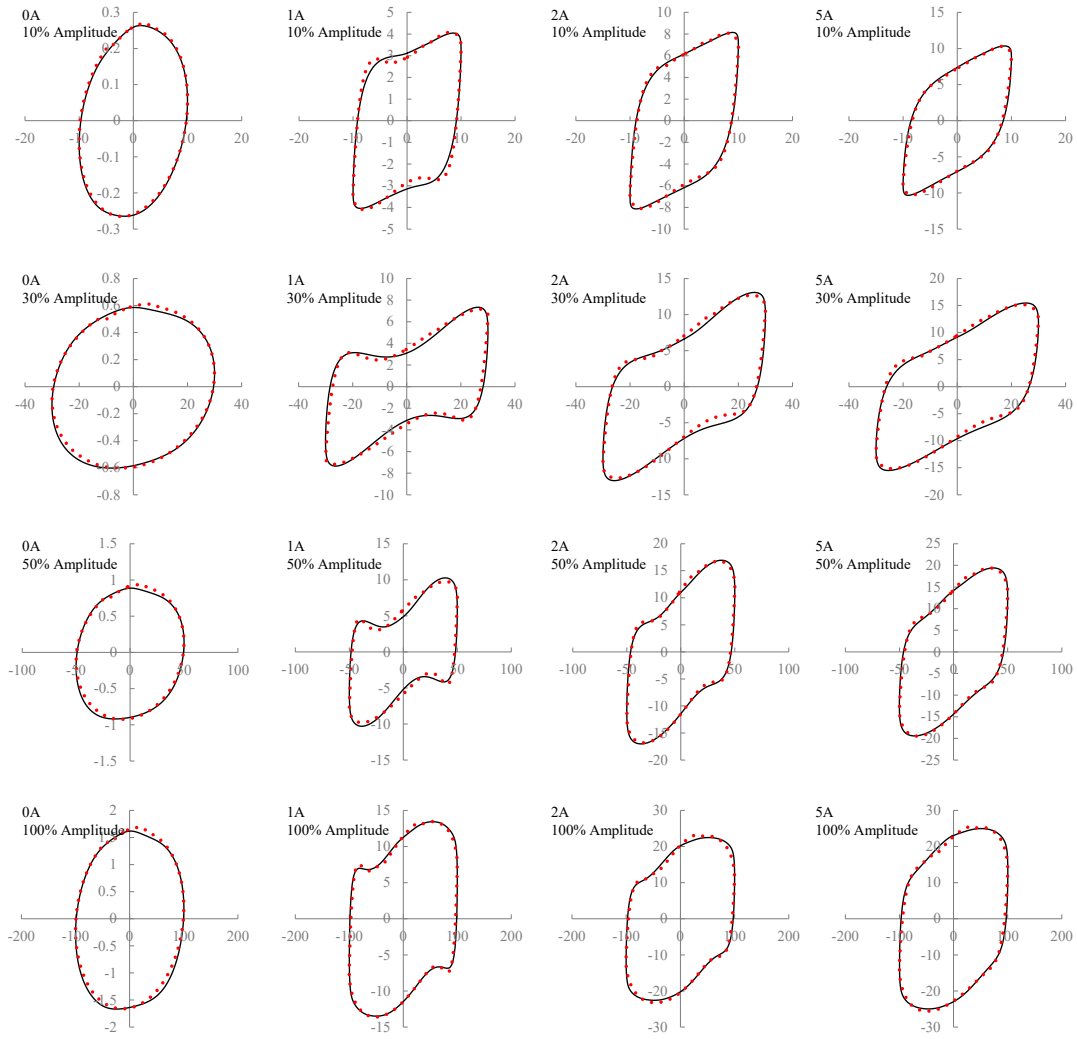

Note:

Horizontal axis: strain amplitude (%); vertical axis: shear stress (kPa); black solid line: experimental data; red dotted line: predicted results from the proposed model.